Development of Thermoelectric Devices: Design, Fabrication and Characterisation

By

Mark Cooper Robbins
BSc (University of Leeds), MSc (University of Leeds/University of Sheffield)

Master's Thesis
Presented for the award of Master of Philosophy
Cardiff University

September 2015

Supervisors Dr Gao Min
Dr Richard Marsh

School of Engineering,
Cardiff University

DECLARATION

This work has not been submitted in substance for any other degree or award at this or any other university or place of learning, nor is being submitted concurrently in candidature for any degree or other award.

Signed …… (candidate) Date ……

STATEMENT 1

This thesis is being submitted in partial fulfillment of the requirements for the degree of ……(insert MCh, MD, MPhil, PhD etc, as appropriate)

Signed …… (candidate) Date ……

STATEMENT 2

This thesis is the result of my own independent work/investigation, except where otherwise stated.

Other sources are acknowledged by explicit references. The views expressed are my own.

Signed …… (candidate) Date ……

STATEMENT 3

I hereby give consent for my thesis, if accepted, to be available online in the University's Open Access repository and for inter-library loan, and for the title and summary to be made available to outside organisations.

Signed …… (candidate) Date ……

STATEMENT 4: PREVIOUSLY APPROVED BAR ON ACCESS

I hereby give consent for my thesis, if accepted, to be available online in the University's Open Access repository and for inter-library loans **after expiry of a bar on access previously approved by the Academic Standards & Quality Committee.**

Signed …… (candidate) Date ……

Summary

Improved efficiencies during waste heat recovery using currently available thermoelectric devices by increased hot-side temperatures push device materials to their operating limits. Magnesium silicide is one such material that is of interest for improved devices which can provide increased efficiencies by withstanding far higher temperatures.

Within this report, progress has been made in achieving ohmic contacts for high-performance tin-antimony doped magnesium silicide and higher manganese silicide. To achieve this, a lab scale prototyping and characterisation facility was designed and tested. Furthermore, a COMSOL model was developed for module prototyping verification and has been validated using empirical data. In addition, to achieve the fabrication of a prototype module a joining process is developed for pre-contacted co-sintered antimony doped magnesium silicide and undoped higher manganese silicide. Moreover, assembly and characterisation of a prototype 7-couple module is performed followed by its characterisation data being used to validate a COMSOL model.

Results showed contact sheet resistances of 8.58 ± 0.61 $\mu\Omega.cm^2$ and 32.7 ± 0.95 $\mu\Omega.cm^2$ being achieved for silver brazed antimony doped magnesium silicide and undoped higher manganese silicide, respectively. Furthermore, the prototype module created within this study has a power density of 130.29 mW/cm^2 under a 300^oC temperature differential. Moreover, barrier coating studies were additionally carried out for high figure of merit tin-antimony doped magnesium silicide and undoped higher manganese silicide investigating electrolytic plating, electroless plating, and sputter coating deposition techniques. Results demonstrated a sputter-coated nickel layer at a thickness of 1.2 μm with a 300 nm titanium adhesion layer results in a contact sheet resistance of 467.00 ± 8.35E $\mu\Omega.cm^2$ and 17.00 ± 0.13 $\mu\Omega.cm^2$ for silver brazed tin-antimony doped magnesium silicide and undoped higher manganese silicide, respectively. Furthermore, from the empirically verified COMSOL model a final COMSOL simulation is carried out with ideal values for the high-performance silicide material and a power density of 143mW/cm^2 is calculated.

These results show that improvement of the barrier layer can lead to a significantly more efficient device by incorporating higher performance, higher operating temperature materials, however with increasing dopant levels effective joining processes becomes increasingly difficult.

Acknowledgements

For general and technical support for the duration of the study, acknowledgement is made to Dr Gao Min of Cardiff University and Mr Kevin Simpson of European Thermodynamics. For technical help and discussion, thanks are given to Dr Richard Tuley and Dr Christopher Stuttle of European Thermodynamics Ltd. Support from groups at Queen Mary, University of London, IntrinsiQ Materials, London, Toyota-Tsusho, Yasunaga Corp, TEER Coatings and Loughborough University is recognised for helpful discussions and assistance with equipment that made this study possible. Finally, thanks are made to Innovate UK and the Knowledge Transfer Partnership for funding of projects that feature in this study.

Dedication

"What is written without effort is in general read without pleasure."

Samuel Johnson (1709-1784)

This thesis is dedicated to the ones I love. My long term partner, Melanie Potts, for her unconditional love and support throughout the duration of this research. My father, Denis Robbins, for his invaluable advice and encouragement throughout my scientific career. Finally, to all of my friends, family and extended family for their inspiration, support and companionship. Without you, the effort I have been able to put into this work would not be possible.

Contents

1. Introduction

1.1. Background

Due to the laws of thermodynamics, waste heat is generated in all processes and leads to reductions in energetic efficiencies. A great number of reactions take place where the thermal energy waste is negligible, but when processes are highly calorific and exhibit low efficiencies a large amount of heat is often wasted. As a result, this leads to significant financial and environmental ramifications as valuable resources are converted into significant amounts of heat to be dissipated into the environment. In these situations, increases in efficiency are critical and can result in relatively large amounts of energy and money being saved. The efficiency increases can either be undertaken within a process which is application specific, but can also take place by reclaiming some of the energy from the significant amounts of exhausted heat.

Thermoelectric devices offer a solution for energy reclamation from applications with large amounts of waste heat. Using a thermal gradient, thermoelectric devices convert waste heat into usable electrical power via the Seebeck effect.

1.1.1. Seebeck Effect

Thermoelectric devices designed for energy generation operate due to the principal of the Seebeck effect. The Seebeck effect is best described using the single unit of a thermoelectric device, the thermocouple, shown in Figure 1.

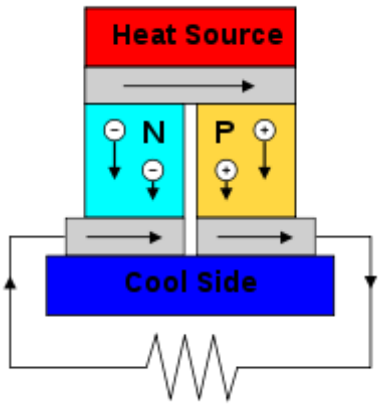

Figure 1. Basic schematic of a thermocouple [1].

A thermocouple comprises two dissimilar metals, or an n-type and p-type semiconductor pair, joined electrically in series. When a known temperature gradient is applied between the junction of the two materials and their ends, a potential difference can be measured between the two metals. From this, the Seebeck coefficient can be calculated. The Seebeck coefficient is represented in Volts per Kelvin (V/K) and is signified by the Greek character alpha (α) [2].

1.1.2 Figure of Merit

The Seebeck coefficient is an important material parameter for characterising the performance of a thermoelectric material. A greater Seebeck coefficient for a given material at a set temperature differential leads to a greater electrical potential in comparison to a different material with a lower Seebeck coefficient. The electrical conductivity (σ) is also an important material parameter to be considered when developing thermoelectric materials. By maximising the electrical conductivity (or minimising the resistivity), the ability for charge carriers to flow in the material is increased thus reducing I^2R losses.

Material developers often refer to the 'power factor' of a thermoelectric material. The power factor is calculated by combining the Seebeck coefficient and the electrical conductivity as $\alpha^2\sigma$; this term summarises the electrical properties of the material but negates its thermal characteristics. Thus, this term is often used in specific applications where device thermal properties are of lesser importance.

The final parameter that is particularly important to material developers is the thermal conductivity of the material, represented by the Greek letter Kappa (κ). It is important to minimise this value so as to maximise the temperature differential across the material when under operation, thus enabling a greater potential difference to be achieved by the Seebeck effect. Thermoelectric material developers aim to maximise the electrical conductivity and Seebeck coefficient while minimising the thermal conductivity i.e. creating a phonon glass electron crystal (PEGC). The main difficulty is that electrical conductivity and thermal conductivity are innately linked. By increasing the electrical conductivity, it will increase the thermal conductivity due to the electronic component of thermal transfer in materials. The thermal conductivity is the product of the electron and lattice parameter as shown in Equation 1.

$$\kappa_{tot} = \kappa_{lattice} + \kappa_{electron} \quad (1)$$

Efforts have been made to maximise the electrical conductivity and Seebeck coefficient and minimise the thermal conductivity by utilising the properties of particular crystal structures

and nano-structuring of materials to interrupt the phononic transfer through the material. Crystal structures such as the chalcogenide series and a cage-like structure are explored which have inclusions that harmonically reduce or reflect phonons in the material. The chalcogenide series has compounds such as cadmium iodide (CdI_2) which upon alloying with elements such as copper and silver causes intercalation of the molecules between the CdI_2 layers[3]. The modification of the crystal structure causes a reduction in the thermal conductivity while causing no effect on electrical conductivity due to phonon scattering. A similar approach is taken using cubic cell crystal structures. Dopants are introduced into the cell which are loosely bonded by Van der Waals forces. The inclusions inside the cell can rattle and disperse the phonons, hence the common term '*rattler*' for this structure[4]. Other nano-processing techniques are implemented by producing the material from a nano-powder and pressing the powder at high pressure and temperature to form a highly dense disc of material. Nanopowders are typically produced using the method of ball milling; this is an efficient technique that is easily scaled up for production. Pressing of the nano-powder is usually carried out using a hot pressing method or Spark Plasma Sintering (SPS) [5]. Hot pressing involves pressing the powder in a die which is simultaneously heated by an electrical heat source, achieving moderate heating rates. SPS is similar to hot pressing in that the powders are pressed in a die under elevated temperatures, but the heat is applied by passing a high current through the die (and material) to achieve higher heating rates from Joule heating [6].

The thermoelectric figure of merit (Z) combines three important factors for thermoelectric materials: Seebeck coefficient, electrical conductivity and thermal conductivity. The figure of merit is calculated by dividing the power factor by the thermal conductivity; as shown in Equation 2.

$$Z = \frac{\alpha^2 \sigma}{\kappa} \tag{2}$$

This is in line with the fact that the material performance will be boosted by increasing the Seebeck coefficient and the electrical conductivity or reducing the thermal conductivity. Therefore, a higher 'Z' value for a material indicates a higher performing material. The value for the thermoelectric figure of merit changes over the temperature of operation of a material. It is commonly represented graphically by multiplying it by the temperature in Kelvin, termed 'ZT' and represents the dimensionless figure of merit, shown in Equation 3.

$$ZT = \frac{T\alpha^2 \sigma}{\kappa} \tag{3}$$

The graphical representation of the ZT will typically increase at lower temperatures, peak and then drop as the melting temperature of the material is reached/neared. The ZT is most commonly used when comparing thermoelectric materials. Figure 2 shows the ZT curves for a selection of thermoelectric materials.

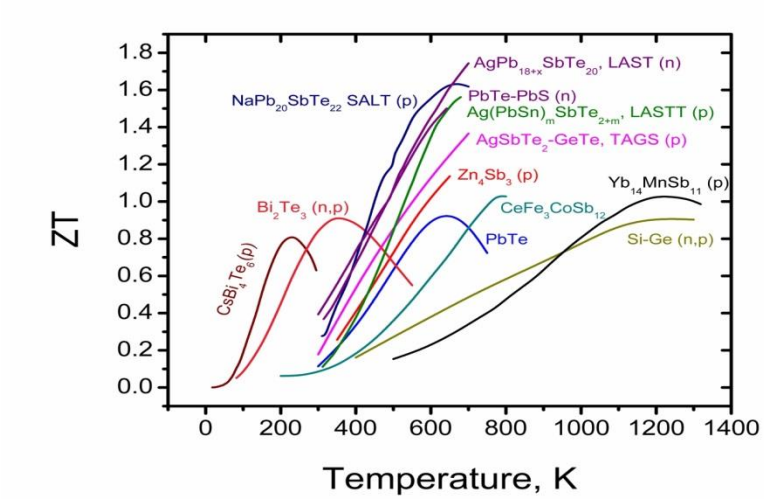

Figure 2. Dimensionless figure of merit (ZT) for a variety of thermoelectric materials [7].

1.2 Thermoelectric Generator Design

The basic module design is used commonly for commercial devices, in which the thermoelectric materials are assembled and joined between two metallized ceramics, forming an electrically insulated module at both hot and cold thermal contacts. It offers a more straightforward assembly process as the number of components for assembly is minimised in comparison to other designs that will be described in the next section.

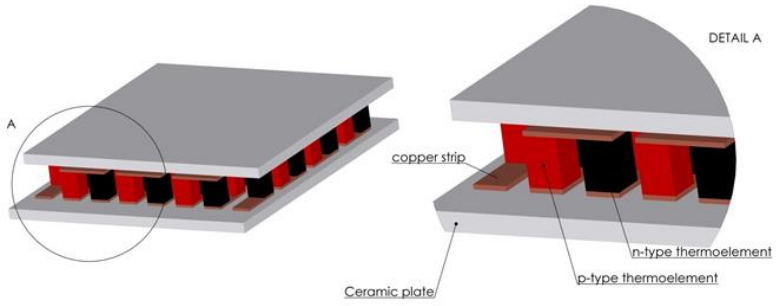

Figure 3. A schematic outlining the particular components in the standard module design with ceramic plates on the top and bottom of the module.

Figure 3 shows a schematic of the standard design for a thermoelectric module used for commercial modules and prototyped modules. The ceramic plates and copper contacts represent a single component as the copper is directly bonded to the aluminium oxide ceramic. This is often nickel plated to increase the mechanical strength of the joint and to reduce interdiffusion of copper during operation at elevated temperatures.

Thermoelectric modules are manufactured by joining the n-type and p-type semiconductor materials electrically in series and thermally in parallel, while insulating the components between two ceramic substrates. The ceramic substrates are typically metallised using the direct bonded copper (DBC) approach and form the circuit for joining the materials in electrical series.

The semiconductor materials are cut from a disc to produce many square based prism shaped pellets and soldered to the copper electrical contacts that are arranged on the metallised ceramics. This process is commonly split into two stages: The hot side pellets are soldered to the hot side metallized ceramic with a high-temperature solder. The next step completes the circuit by soldering the cold side to the second metallized ceramic substrate using a lower temperature melting point solder. The method is used to ensure that the hot side pellets are not removed from the metallised ceramic when the cold side pellets are joined, thus simplifying jig design. For large scale module manufacture, the soldering process is carried out in a belt furnace with an inert atmosphere. The process enables the manufacturer to batch solder modules without damaging the semiconductor material.

To protect the semiconductor materials during operation, a barrier coating is applied to the contacts of the pellets before soldering. The barrier coating is applied to reduce inter-diffusion of elements across the solder junction and as a secondary function it increases the bond strength between the solder and semiconductor material. Nickel is the main material that is deposited by electrodeposition onto the contacts before cutting of the discs. In some cases molybdenum, tin and bismuth are also included to improve the mechanical properties of the layer. Under continual operation, elements such as copper can migrate into the semiconductor causing a change in electrical and mechanical properties, thus reducing the lifetime and performance of the device.

Improvements to modules can be achieved by modifying particular aspects of the design. One mode of failure arises from the brittleness of the aluminium oxide ceramic substrates. The variety of materials under thermal stress in a module means there is an inherant issue with mismatches in coefficient of thermal expansion. The stresses are most commonly relieved in the ceramics of modules as cracks. This can cause open or closed circuit failures in the

module. By using alternative ceramics which possess better mechanical properties, such as aluminium nitride (AlN) [8] and silicon nitride (SiN) [9], the potential for this failure mode can be reduced. Furthermore, non-oxide ceramics, such as nitrides, have been found to exhibit a higher thermal conductivity than some of the more common oxide ceramics[8, 9]. This is favourable as the maximum efficiency (ϕ_{Max}) of a module is dependent on the temperature differential across the semiconductor pellets, shown in Equation 4.

$$\varphi_{max} = \frac{T_H - T_C}{T_H} \cdot \frac{\sqrt{1+Z_C\bar{T}}-1}{\sqrt{1+Z_C\bar{T}}+\frac{T_C}{T_H}} \qquad (4)$$

Where T_H and T_C are the temperatures of the hot and cold side of the pellets respectively. Z_C is the combined figure of merit of the couple and $\bar{T}$ is the average temperature across the pellets [10]. If heat transfer to the semiconductor material is maximised, maximum efficiency of the device is increased. Other modifications include: using stronger ceramics such as AlN to enable a thinner substrate to be used, oxidation/sublimation coatings for pellets and filling the air gaps in the module with a low thermal conductivity material such as Aerogel. These alterations can all contribute to increased performance or lifetime of a thermoelectric module for power generation.

1.2.1 Joining Test Thermocouple/Uni-junction

The uni-junction design offers a method for high throughput testing of contact resistance and semiconductor material resistivity using minimal amounts of sample material. The assembly consists of two sample pellets that are joined end to end with a solder or braze paste and a metallic contact in the middle. When polished, the two junctions can be characterised using four point probe measurements along a linear axis. Figure 4 shows a basic schematic of the uni-junction design.

Figure 4. Schematic of the uni-junction design. The key on the right-hand side outlines the specific parts with the colour on the schematic.

This design can also be used to produce a p-n junction or thermocouple, to test the compatibility of two corresponding thermoelectric materials under the same joining process. Success with this type of assembly will determine if the process is suitable for prototyping in a module form.

1.2.2 High-Temperature Module Design

To reduce stresses in the module, arising from differences in thermal expansion coefficients at high temperature differentials; extra degrees of freedom have to be introduced into the module design. One design that has been explored involves the removal of the hot side ceramic from the assembly. This increases assembly complexity but in turn reduces the residual stresses in the module under operation by allowing the legs to 'fan out'. Figure 5 shows a schematic of the design. Metal tabs are used as the electrical contacts to complete the series circuit.

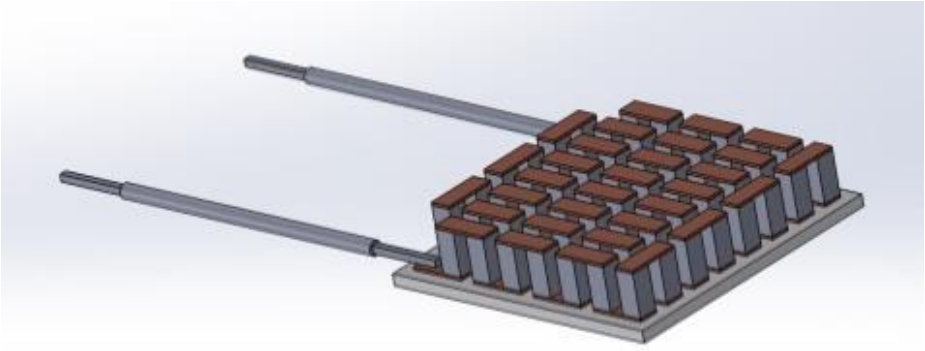

Figure 5. A schematic of the proposed design for a high-temperature module. The module is assembled with metal tabs as the electrical interconnects for the hot side of the module, replacing a metallised ceramic.

1.3 Motivation

The current commercially available thermoelectric generators use bismuth telluride as the thermoelectric semiconductor. Due to the performance characteristics of bismuth telluride with respect to temperature and joining technology, they are designed to operate up to a maximum hot side temperature of 250^{o}C to 300^{o}C [11]. Currently, there are no commercially available higher temperature options for energy harvesting using thermoelectric devices. The Organic Rankine Cycle (ORC) is an example of a system which offers a higher efficiency (~30%) and higher temperature solution (~400^{o}C max) for energy harvesting than thermoelectric devices [12]. But with many working parts and typically a greater system size,

this process is not feasible for applications where autonomy, system weight and size are critical e.g. the automotive industry. Thermoelectric devices could fit the scope for higher temperature applications, owing to their comparably smaller size, low maintenance due to no moving parts and silent operation, should a commercially available high temperature device become available.

Industries such as the automotive sector, marine, smelting, incineration and many others where high-temperature waste heat is lost could benefit from this technology [13]. Automotive companies like Jaguar Land Rover, BMW and Fiat, have shown interest in thermoelectric technology for increasing efficiency of their cars. Harvesting the waste heat lost from exhaust gases, to produce electrical power which can be fed back into the cars system will subsequently allow them to reduce the size/load of the alternator in the engine, thus reducing the load on the engine and increasing engine fuel economy. The aim is to maximise the average power output of the system when under a standardised drive cycle. An example of this is the New European Drive Cycle (NEDC). The peak system power output that developers aim for is a minimum of 300 W; this is an estimate based on a 5% system efficiency, taking into account the weight penalty of the device itself. In exhaust systems for a mid-range diesel engine, the exhaust gas can reach temperatures in the region of 500^{o}C to 700^{o}C after the catalytic converter. A system based on Bismuth Telluride devices would utilise only a small proportion of the exhaust gas energy. To achieve a higher power output, it is necessary to develop higher temperature modules that can harness the full potential of the exhaust gas.

Another important factor in developing thermoelectric devices lies in cost, abundance and toxicity of raw materials. Bismuth Telluride has the chemical formula Bi_2Te_3 and so its major component is tellurium and is typically doped with antimony, both of which are low in abundance and toxic [14]. With increasing prices for precious metals, the need for thermoelectric modules based on more abundant elements like silicon and sulphur is ever increasing.

When developing new modules comprising novel materials, one of the greatest challenges lies in the electrical and thermal joining of the new material to electrical contacts. The technology for low-temperature devices is well served by widely available materials. Extensive development of lead or tin based solders in the electronics industry means there are numerous options to choose from, many of which produce excellent thermal and electrical properties. These characteristics are important for thermoelectric modules, as the solder junction is required to have a low electrical resistance and high thermal conductivity.

Another fundamental property of the solder junction is the mechanical strength. The solder joint acts as a structural component of the module. Despite the availability of low-

temperature solder alloys, it can be difficult to achieve a mechanically robust joint due to the properties of the semiconductor material. An example of this was in the early development of bismuth telluride modules. Bismuth telluride exhibits poor adhesion and solder wetting when bonding directly to the material. To add strength to the connection, a nickel barrier is deposited onto the contact faces of the material before cutting. The nickel layer promotes better adhesion and wetting when soldering, leading to a mechanically stronger joint [15, 16].

Matters arising with solder/braze alloy selection, oxidation/sublimation protection and substrate selection become more important at elevated operating temperatures. Above 300^{o}C, very few solders are available as the elements and alloys that are most available become volatile at such temperatures. Lead has a melting temperature of 328^{o}C, which can be extended up to 370^{o}C in certain alloy compositions but exhibits a wide melting range. Any Zinc based solders will become volatile above 400^{o}C and beyond this point, filler materials are referred to as brazing alloys. Between 400^{o}C and 600^{o}C, the majority of brazing alloys are Aluminium based, such as Aluminium-Silicon. These materials are specifically designed to join Aluminium to Aluminium and do not offer a good electrical joint. Above 600^{o}C, silver based brazing materials become available. Silver is particularly conductive and relatively mechanically robust, but its cost is an issue for mass manufacture. The reactivity in the process of brazing is typically very volatile. It increases the importance of barrier coatings to achieve high-performance thermal, mechanical and ohmic contacts.

Silicides offer an environmentally friendly and low-cost option for thermoelectric module production. Figure of merits in the region of unity are observed within the given temperature range and compatibility with module components show that it is a very promising thermoelectric material. Production time for ingots is of a similar time scale to other competing materials. As with most materials, sublimation and oxidation effects must be overcome at high temperatures for the material to be viable for commercial use in energy harvesting. The materials involved are extremely abundant hence the low cost in these materials. Due to this, silicides were chosen to develop a mid-temperature thermoelectric module. Two silicide material types are used in this study, manufactured by different techniques. The relevant literature for the two materials is reviewed in section 3.5.

The challenges outlined in this section are addressed in this study by means of exploring a variety of barrier coating methods and joining alloys for a novel silicon-based thermoelectric semiconductor material.

1.4 Aims and Objectives

The aims of this study are:

- To establish a lab scale thermoelectric module prototyping facility.
- To develop a joining process for silicide thermoelectric modules that is scalable for mass manufacture with respect to cost effectiveness and material abundance.
- To manufacture and characterise a prototype silicide thermoelectric generator module.
- To develop a computational model for simulation of thermoelectric modules using COMSOL Multiphysics software.

To achieve these goals, the following actions will be taken:

- Equipment will be sourced for the various stages necessary for material preparation, joining trials and thermoelectric module prototyping.
- Characterisation equipment will be designed and built for performance verification of thermoelectric samples.
- Various metal layer deposition methods will be assessed for their effectiveness as a barrier coating.
- Lab scale joining trials will be carried out with a range of joining alloys. Characterisation equipment will be used to measure the performance of the sample junctions.
- Once a suitable joining process is defined, a small prototype module will be assembled and characterised.
- Validation of the COMSOL model will be carried out using characterisation data from a prototype module.

2 Design and Development of a Thermoelectric Lab

To assemble modules, the important considerations are to accurately position the elements while protecting the material during the joining process. To do this, specific equipment is tested for suitability that enables the process to be carried out under vacuum or inert atmosphere. Furthermore, various jig designs have been tested based on commercial designs and novel approaches for improving the protection and positioning of the components during the assembly process. Finally, the equipment for processing the thermoelectric material is considered and the important factors for assembly are explained.

For operating temperatures up to 500^{o}C, certain design considerations are necessary to reduce thermal stresses on a module when in operation. The coefficient of thermal expansion becomes important as a temperature differential of 500^{o}C can cause large deformations across a module, inducing stresses that increase the probability of failure when in operation.

This chapter describes the different assembly designs used throughout the research process through to final module design.

2.1 Thermoelectric Material Sectioning

An important stage of material processing is in the sectioning of thermoelectric materials from pucks into pellets. Thermoelectric materials are inherently brittle owing to their glass like internal structure causing them to be difficult to process from pucks into pellets. Specific equipment is used to grind and cut the materials effectively. For lab scale material processing, an automated grinding and sectioning machine (Struers Accutom-50, see Figure 6) is used to grind and section the pucks using a diamond cup and blade. The fluid used for cooling and lubrication during cutting is a water based solution. Corrozip-LF is an additive developed by Struers and is recommended for use on this equipment. Initially, cutting is carried out using this fluid, but due to the reactivity of the magnesium-based alloys, a water free option is tested. An oil based fluid is tested for improved protection of the thermoelectric material in later tests to reduce resistance in the thermoelectric junctions. The oil based fluid is supplied by Struers and is a recommended product for use on the Accutom-50 cutting machine.

Figure 6. Struers Accutom-50, used for grinding and cutting of thermoelectric material.

It is important to firstly grind the faces of the thermoelectric pucks to achieve parallel surfaces; this ensures that when pellets are cut from the puck that they are all of the same height. A grinding cup is used to achieve parallel faces by controlled removal of material from both faces of the puck. A second function of this process is to remove the fouled top layer of the material to expose fresh material for plating and joining. The grinding process can produce parallel surfaces with a tolerance of approximately 5 μm to 40 μm; this is an acceptable tolerance for module manufacture as the solder/braze bond line is typically of an order thicker.

The next stage of processing is sectioning of the ground puck using a diamond blade. Graphite sacrificial material is used to mount the puck and the material is sectioned. The sample is then removed and turned 90^{o} for the second stage of sectioning to produce square based pellets. Figure 7 shows samples after grinding and dicing. Once the materials are processed, cleaning stages are carried out using acetone, isopropanol and deionized water.

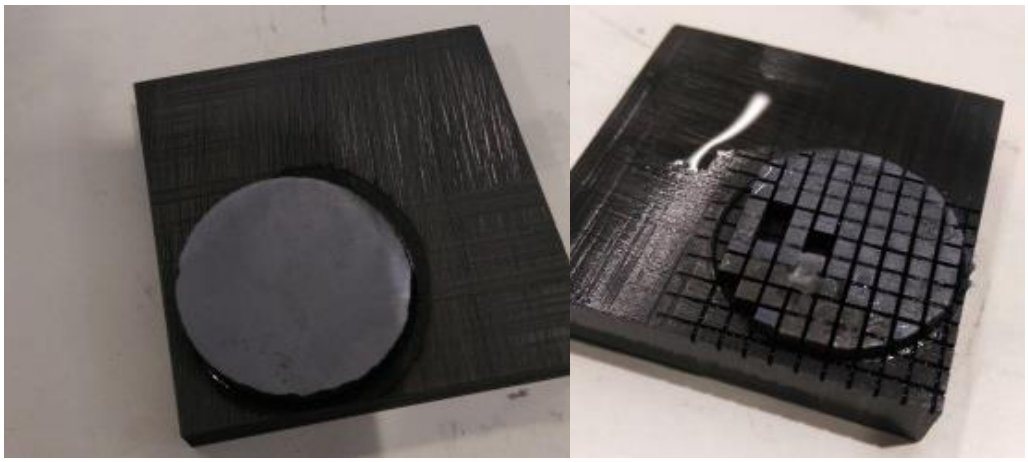

Figure 7. Sample puck after grinding (left) and dicing (right). Pellets are occasionally ejected but can be retrieved from the tray below the sample stage.

For larger scale sectioning, a multi-wire diamond saw can be used. This process uses a multiple diamond coated wires that are aligned in parallel to section large surface areas of thermoelectric material. A diamond abrasive slurry is used as a coolant and to aid in cutting and to reduce the chance of fracturing of the materials.

This process represents a significant part of the module manufacturing procedure. Technologies such as net shaping of pellets offers a potential method for cutting the lengthy material sectioning stages out of the manufacturing process. A process such as hot isostatic processing (HIP), where single pellets of the powder are pressed with equal pressure in all axes, could lead to significant cost savings by reduction of cutting losses and time saving in the overall manufacturing duration. A drawback of this process is to overcome the issues with density and sintering of the final pellets.

2.2 Vacuum Brazing Equipment

The vacuum brazing process is based on a tube furnace and vacuum tube system. A vacuum brazing process is explored for mid to high-temperature thermoelectric materials. The system must be taken to high temperatures, above the defined working temperature of the module, as the electrical joints must be stable above this temperature in operation. As the process is carried out at high temperatures, the electrical joints and the thermoelectric material must be protected from oxidation, which would otherwise be detrimental to the performance of the device in increased resistance and reduced effective pellet size.

A Carbolite CTF tube furnace was used for brazing, which has a heated area of 900 mm. The vacuum system is comprised of an Inconel work tube that is sealed at one end. It has a vacuum flange at the opening to connect the vacuum pump and is used to insert the assemblies. An Edwards RV5 rotary vane vacuum pump is used to evacuate the system and a Pirani gauge is used to monitor the vacuum level.

The system is designed to reduce cooling time by having a removable vacuum chamber; this reduces the duration of time that the assembly is at elevated temperatures through ambient cooling of the system as opposed to natural cooling of the whole system, which can be extremely time consuming. Typically, lab scale vacuum brazing systems use a glass work tube that is fixed in the heating chamber of the furnace. An Inconel chamber is used as it is particularly strong and resistant to thermal shock that would otherwise damage a glass vacuum tube upon removal from the furnace.

Figure 8 shows a schematic of the vacuum brazing system. The vacuum tube is mounted on supports outside of the furnace and the flange is removed, the sample to be brazed is inserted into the tube and the flange is re-positioned on the tube. The vacuum pump is then activated and the pressure is monitored via the Pirani gauge system. The furnace is preheated to the brazing temperature plus an additional temperature value to account for thermal losses and gradients across the Inconel tube. The Inconel tube is inserted into the furnace and an internal thermocouple is used to monitor the temperature inside the tube, this is located in the region of the sample inside the tube. Once the temperature gauge reaches the desired temperature, the sample is left to dwell to allow for sufficient heat to penetrate the sample. Once brazing is completed, the Inconel tube is removed from the furnace onto a heat resistant mount. The system is left to cool and the sample is removed by purging the vacuum system and removing the flange system once a safe temperature is displayed on the internal thermocouple reader.

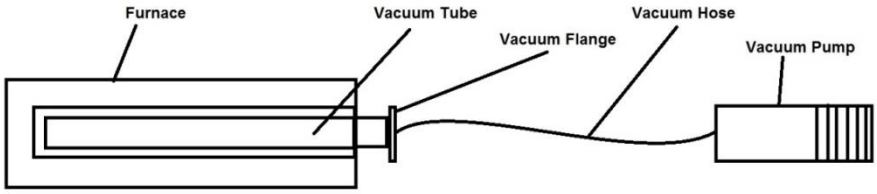

Figure 8. A schematic of the vacuum brazing system incorporating an Inconel vacuum tube and vacuum pump.

The vacuum tube is connected to the pump by a flexible Nalgene hose that is stable under low pressure; the flexibility enables the vacuum tube to be removed with minimal interference from the vacuum pump assembly. The system is capable of reaching a vacuum pressure of 2×10^{-2} Torr which means the brazing can be carried out with approximately 10000 times less oxygen in the system than at normal atmospheric pressure.

Figure 9 and Figure 10 show images of the vacuum brazing system during cooling and an internal view of the vacuum chamber. Due to the hazardous nature of this process, strict health and safety procedures are exercised. Only one user may use the system at any time and another person must always be supervising the process in case of emergency. High-temperature heat proof gauntlets are used to prevent burns and protective eyewear is used in the unlikely case of explosion/implosion of the system. A risk assessment is carried out for the process and is reviewed periodically. The process and equipment is designed so that contact is not made with heated parts of the system, but the relevant precautions are taken to reduce chances of injury.

Figure 9. An image showing the vacuum system once a brazing trial has been completed during the cooling phase.

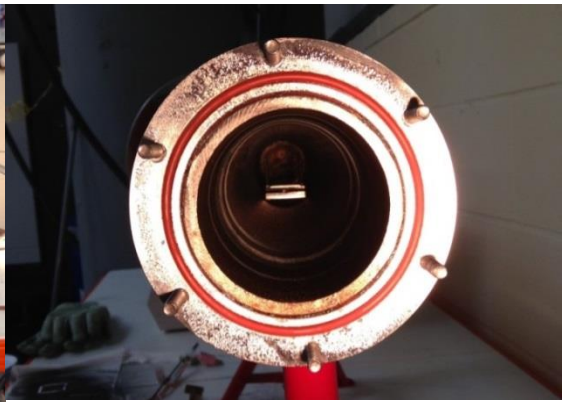

Figure 10.Vacuum flange location and internal view of the Inconel vacuum tube.

2.3 Jig Design

A jig used to hold the thermoelectric assembly in position during soldering or brazing to prevent components from becoming displaced when the solder or braze alloy is in a liquid state. Furthermore, this allows the assembly to be clamped; which assists in minimising the joining bond line. Various jig designs have been explored with varying materials depending on the joining process.

For low-temperature devices, where soldering is necessary, a simple jig design can be used for prototyping. The process for low temperature devices uses a procedure in which one end of the thermoelectric elements are soldered to the metallized substrate with a specific alloy followed by a second soldering stage in which an alloy is used with a lower melting temperature is used to attach the metallised substrate and form a complete thermoelectric module. This process requires a simpler jig design as it is only necessary to position one side of the module and utilises the weight of the jig to provide a compressive force to minimise the solder bond line.

Figure 11 shows an example of the jigs that can be used to position pellets during soldering. This process is typically carried out using a hot plate to provide heat to the side of the assembly that is to be soldered. The recesses in the jig hold the pellets in position and a weight can be applied to provide compression during the soldering process. This is typically carried out in an inert/reduced oxygen atmosphere to minimise damage through the oxidation of the thermoelectric material. The jigs can be made from metal or plastic dependent on processing temperature. For low temperature, the jigs can be 3D printed or injection moulded.

For higher temperatures, metal jigs can be used by which the ‘checkerboard’ is laser cut out of a metallic sheet and is then mounted on a metallic backing plate.

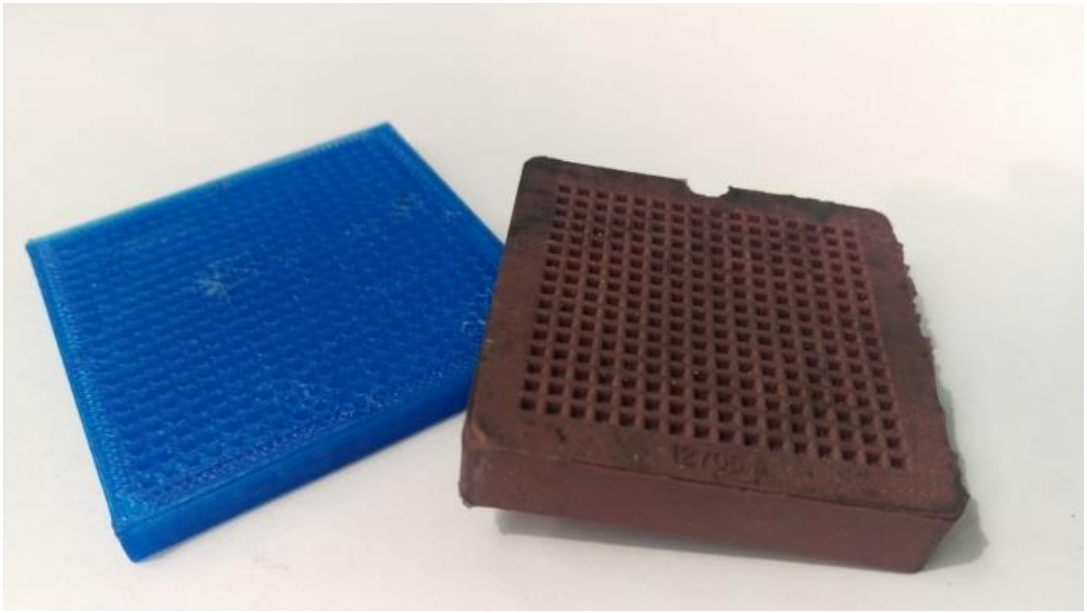

Figure 11. Examples of jigs for Bismuth Telluride module prototyping.

A second approach that can be used for both high and low temperature joining processes is the ‘comb’ type jig. The methodology behind this approach is to solder both sides of the pellets to the metallised ceramics with the same temperature joining alloy in one step. To perform this process, the pellets must be held in position during the joining process and then the jig must be dismantled to reveal the final module. There is difficulty in positioning the internal pellets of the module; as due to the geometry of the module, the jig will essentially be soldered into the module. To overcome this problem, a more complex jig is designed containing two ‘comb’ parts that interlock to provide the ‘checkerboard’ matrix of spaces for the pellets to be positioned. Once the joining process is completed, the combs can be removed independently, so as not to damage the thermoelectric legs. Figure 12 shows an example of the components for this type of jig.

Figure 12. Components of a 'comb' style jig. The fingers are positioned at a 90^{o} pitch to provide the 'checkerboard' arrangement to position the pellets on the metallised ceramic.

An issue with the 'comb' style jig is the threat of the joining alloy attaching the module assembly to the comb teeth. This can be overcome by using thinner teeth, but there is a limit to the size with respect to rigidity and the ability to manufacture the components. To address this issue, thin stainless steel wire is used to provide the 'checkerboard' matrix for pellet positioning. The wire can be removed from the module assembly once joining is complete and provides a thinner alternative to the 'comb' style jig. Figure 13 shows an example of the 'wire' jig. The stainless steel wire has a cross-sectional diameter of 1mm, which is the standard pellet spacing used for module prototyping. The wire is woven into a mesh using small holes in the outer ring of the jig, providing the matrix of spaces for pellet positioning.

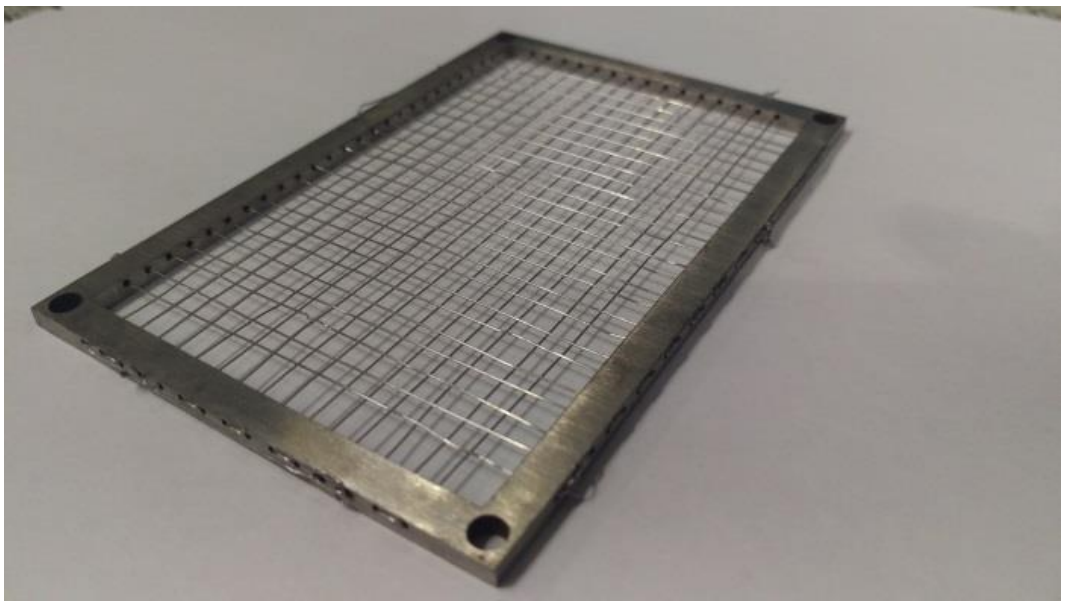

Figure 13. Wire Jig for pellet positioning during joining procedure.

Metal, plastic or rubber materials can be used for the low-temperature modules dependent on the actual temperature necessary for the joining material to flow. Aluminium is most commonly the chosen metal for low-temperature devices due to price and machinability in comparison to stainless steel. For high-temperature processing, stainless steel is always used, as typical brazing temperatures are above the melting temperature of plastics and aluminium.

2.4 Inert Gas Brazing System

The ability to braze under an inert atmosphere is in some cases beneficial as the joining alloy system may be designed for inert atmospheres and is representative of systems that can be used in the future to upscale the manufacturing of the prototypes, for example in an inert atmosphere belt furnace. Furthermore, with respect to brazing processes, silver brazing alloys commonly contain zinc that is particularly volatile under excess heat. In a vacuum system, zinc can evaporate above 420^{o}C coating all components within the chamber and the chamber interior itself to become coated with a zinc layer.

For prototyping purposes, argon gas is used as the inert atmosphere to prevent oxidation of the thermoelectric elements at elevated temperatures. When considering upscaling, argon gas is a possible candidate for an inert atmosphere but is considerably more expensive than nitrogen gas or a reducing atmosphere. An issue with nitrogen gas is that it is typically less pure than argon gas, in that it contains slightly more oxygen and moisture, which would lead

to degradation of the thermoelectric elements under high temperatures. Furthermore, nitrogenization of the semiconductor materials can occur if it is particularly reactive.

A tube furnace is used to apply heat to the system under the inert atmosphere brazing process and two additional methods can be used to encapsulate the system during the process. The first process is to use a vacuum tube that is evacuated and then filled with argon gas; this process is repeated a minimum of three times to minimise oxygen levels in the system. This method is less favoured as the chamber is particularly large and so a large volume of gas is used for each brazing trial. Secondly, as mentioned previously, due to the presence of zinc in the braze materials, the interior of the system can be coated with a layer of zinc. This can affect the pressure measurement system (Pirani valve) and can foul other experiments that may be sensitive to zinc.

To overcome the issues with using a vacuum tube, a system is developed which is cheaper and more efficient. This system is designed for operation under low volume flow of argon across the assembly within a small chamber. Figure 14 shows a schematic of the system.

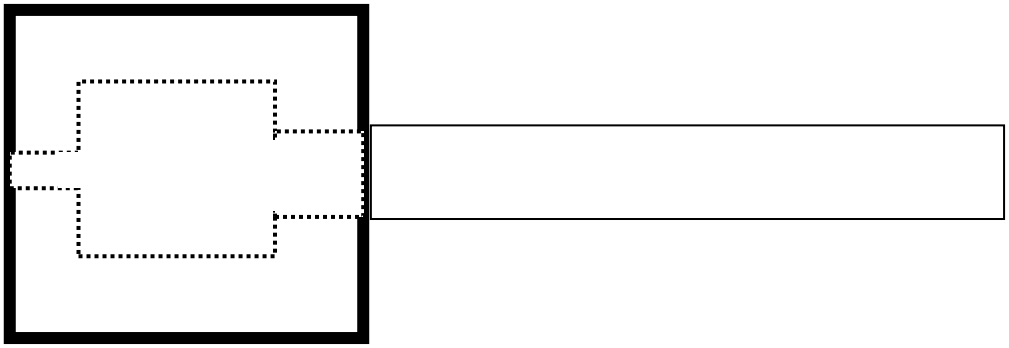

Figure 14. Argon brazing system assembly. The dotted region shows the internal chamber that allows the cross flow of argon across the sample during brazing.

The sample assembly is positioned in the chamber and argon gas is supplied through a metal pipe (from the right). The gas can pass across the sample and exit the chamber through a narrower outlet than the entry inlet. This provides a positive pressure in the system and so reduces the risk of oxygen entering the system during the brazing process.

This assembly is inserted into the tube furnace for heating. The prototype chamber is made from graphite and so assists in scavenging of oxygen to protect the sample thermoelectric device contained within. The assembly can be seen in Figure 15.

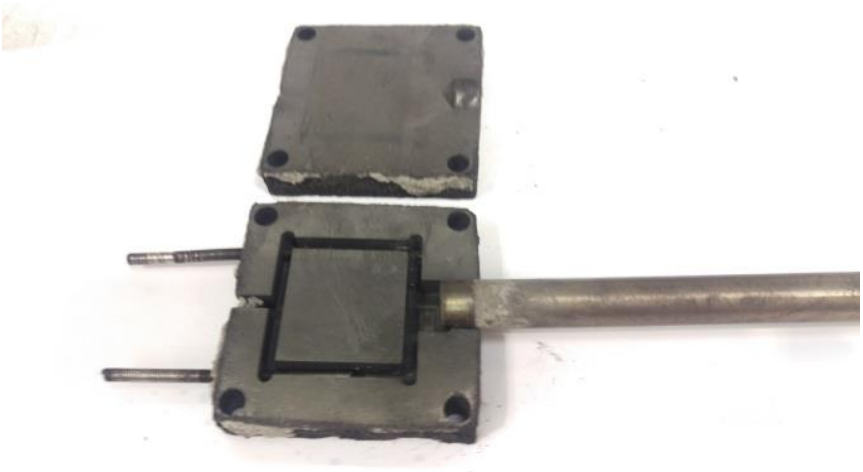

Figure 15. Graphite Argon flow jig for contact resistance sample production.

After extended tests using the graphite jig, it was found that degradation of the chamber occurs over time. The graphite oxidises at high temperatures and becomes fragile, thus during testing, the probability of oxygen ingress is more likely. As a result, the jig is re-manufactured out of stainless steel. Furthermore, a chamber for 7-couple prototyping is added to maximise functionality of the jig. The jig is depicted in Figure 16.

Figure 16. Stainless steel Argon flow jig. Contact resistance samples and 7-couple modules can be brazed in this assembly.

2.5 Thermoelectric Characterisation

Characterisation equipment is a fundamental part of a thermoelectric lab. It is necessary to have equipment which can be used to verify the quality of samples and compare results from different experiments. Characterisation equipment for thermoelectric materials is available to be purchased from companies such as Ulvac and Netszch but is very expensive. Bespoke characterisation equipment is used in this study which is designed and built by European Thermodynamics Ltd and partners.

The Seebeck coefficient can be measured by applying a small known temperature gradient to a sample and analysing the voltage output generated. This measurement can be used to analyse the effect of experiments on the composition of a sample. For example, heat treatment of a sample in air can cause oxidation at the surface; this reduces the effective volume of the material which alters the electrical output. It is likely that a reduction in Seebeck coefficient would be measured between the sample and an untreated specimen.

Sample resistivity measurements are an important tool in defining the quality of a thermoelectric material and junction. For a junction interface, the sheet resistance is calculated. This is a two-dimensional representation of the resistance in a cross section of the junction interface/bond line. A known current is applied across a sample, directed through the junction. Surface voltage measurements are taken along the centre line of the sample. One of the measurement points is taken at the edge of the sample in line with one of the current injection probes, a voltage is measured for incremental distances between the voltage probes (along the centre line) and the data is plotted on a distance-voltage (D-V) plot. The resistance of the contact is calculated using Ohms law. The sample has a known cross section and the thickness of the junction is defined by the D-V plot. Multiplying the measured interface resistance by the cross-sectional area gives the sheet resistance. This is a useful variable for comparing samples using a value that represents how good the joint is for a given area.

From the four point probe data, the bulk semiconductor resistivity can also be calculated. A comparison similar to the Seebeck measurement can be made by assessing the change in resistivity of a sample before and after an experiment. Should an increase in resistivity of the semiconductor be measured after an experiment, degradation in the form of oxidation or sublimation may have occurred. From this reading, samples can be selected for compositional analysis in the bulk material.

Finally, to characterise a full thermoelectric generator module; a system is used which applies and maintains a set temperature difference on the device. The power output is measured over a range of resistive loads. From this data, the maximum power output can be measured which

occurs when the resistive load matches the resistance of the module at that operational temperature.

The following sub sections explain the setup and functioning of each piece of equipment used for characterisation of samples produced in this study.

2.5.1 Seebeck Hot Probe Equipment

For measurement of room temperature Seebeck coefficient, a test rig is developed which imposes a small temperature gradient on a sample and the resulting voltage is obtained. From this, the Seebeck coefficient is calculated in μV/K.

Figure 17 shows a simplified schematic of the equipment. A copper block is used as a cold sink and the sample is inserted between the cold block and copper probe. A weighted force is applied to the acrylic rod to improve clamping of a sample between the copper block and copper probe. This provides better thermal and electrical contact quality. Insulated resistance wire is wound around the copper probe. Electrical power is applied across the resistance wire to provide a small temperature increase above ambient. The system is mounted within an acrylic box to reduce transient temperature gradients from the surroundings during measurement. The differential thermocouple comprises of two copper wires connected by a length of constantan wire. One end of the constantan wire is connected to the copper probe and the remaining end is attached to the copper block. The differential thermocouple is attached using thermally conductive epoxy. This provides a connection that is electrically insulated but maximises thermal conductivity. The copper wires are connected to a Keithley multimeter and when a temperature gradient is applied, a voltage can be measured between the two ends of the constantan wire. This arises from the thermoelectric properties of the constantan wire. The voltage measurement is representative of the temperature difference between the copper probe and copper block. Copper wires are attached to the copper probe and copper cold sink, between the two wires, the Seebeck voltage of a sample can be measured. The physical equipment is shown in Figure 18.

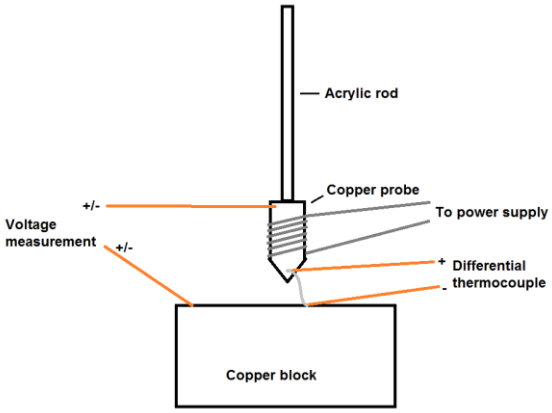

Figure 17. Schematic of custom made room temperature Seebeck measurement kit.

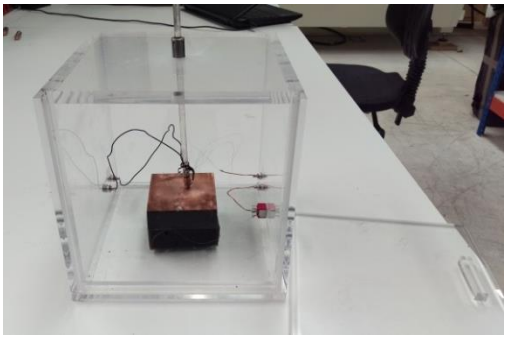

Figure 18. Custom made room temperature Seebeck measurement kit.

When taking a measurement, to improve accuracy the voltage input to the resistance wire is increased incrementally over four readings. The highest temperature differential is typically 20-25^{o}C. The temperature differential is calculated from the Seebeck coefficient of constantan. The calculation also corrects for the Seebeck coefficient of the copper wires. An average Seebeck coefficient is taken across the four readings using graphical representation. An example measurement is shown in Table 1 and Figure 19.

Sample	Power Supply Voltage (V)	Thermocouple Voltage (mV)	Seebeck Voltage (mV)	Seebeck Voltage (uV)	Delta T (K)	Gradient from Graph (uV/K)	Calibrated Gradient (uV/K)
	0.00	0.000	0.000	0	0.000	-233.11	-186.84
N	0.50	0.075	-0.585	-585	2.495		
N	1.00	0.230	-1.780	-1780	7.650		
N	1.50	0.452	-3.499	-3499	15.034		
N	2.00	0.746	-5.788	-5788	24.812		

Table 1. Seebeck coefficient measurement for an n-type bismuth telluride sample.

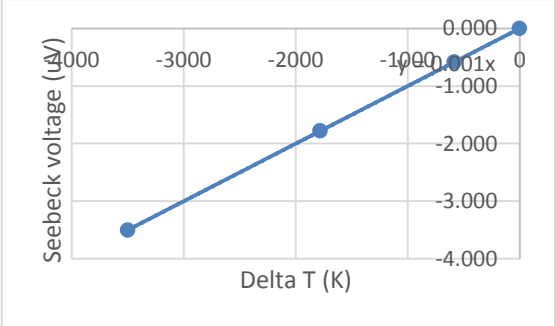

Figure 19. An example of Seebeck measurement results and corresponding graph, for an n-type commercial bismuth telluride sample.

The gradient of the graph produced is calculated in μV/K. The value is then multiplied by a correction factor to give the final calibrated Seebeck coefficient.

2.5.2 4-Point Probe Resistance Measurement Equipment

For characterisation of joining trials, an important factor is the resistance properties across the bonded interface. To characterise this, the sheet resistance is measured using four-point probe resistance measurements along the central axis of a sample. Precision displacement measurements are taken using a three axis probe positioning system (see Figure 20). The sample is clamped in a test mount that applies a known current at each end of the sample. A voltage probe is positioned on the central axis of the sample, as close to the edge at which one of the current input probes is clamped. The fourth probe is incorporated into the precision displacement arm that is loaded with a fine tungsten tip. A Keithley source meter is used to output a short pulse across the sample with a width of approximately 80ms, during which a voltage measurement is taken between the voltage probes. The tungsten probe is lifted and moved along the central axis of the sample. Measurements are taken at recorded displacements from the static voltage probe and the resistance is calculated using Ohms law. The results are plotted in a resistance-displacement graph. The brazed interface can be identified by a change in gradient of the graph (see Figure 21).

The sheet resistance is calculated by multiplying the total resistance change across the junction interface by the cross-sectional area of the sample. This value is most suitable as it is comparable to any geometry of sample with different bond line thicknesses. For a thermoelectric device, for maximum efficiency this value should be minimised. A realistic minimum sheet resistance is expected to be of the order of 10^{-5} $\Omega.cm^2$. From this data, the resistivity of the semiconductor can also be calculated as measurements along the sample are taken up to the junction. Comparing the resistivity of a sample before and after an experiment will indicate if the semiconductor material has been damaged by diffusion, sublimation or oxidation as the electrical properties will be affected by this.

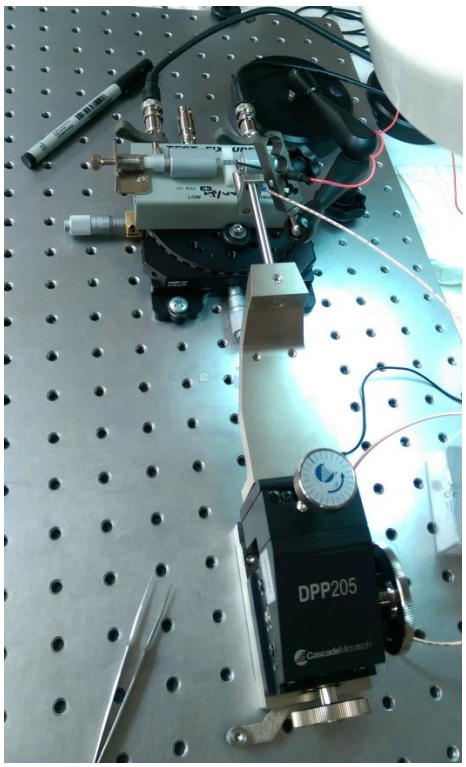

Figure 20. 4 point probe test bed for contact resistance characterisation.

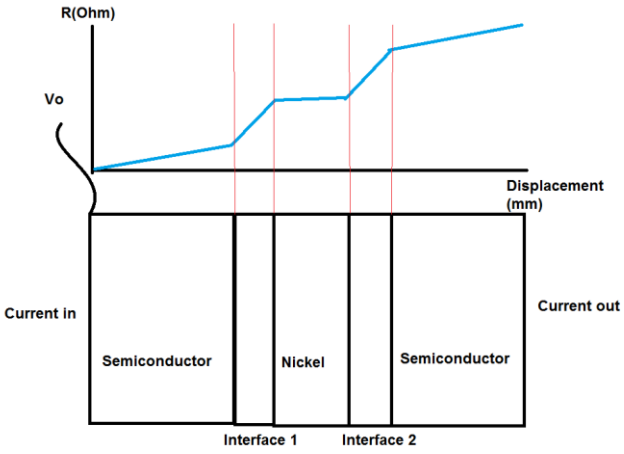

Figure 21. Schematic showing an example of a graphical representation of resistance along a sample and the reference of location on a sample.

2.5.2.1 Uncertainty Analysis of Contact Resistance Measurement

The main metric used for analysis of junction quality in this study was the contact resistance, measured using the 4-point probe equipment described in this section. To understand the accuracy and limitations of this measurement, uncertainty analysis was carried out using some example measurements [17]. Readings for a sample with a contact resistance in the 1 mΩ.cm^2 range and for a sample with a contact resistance in the 10 μΩ.cm^2 range will be analysed and compared. This serves as an example of how the error limits are calculated for all of the measurements of contact resistance in this study as it is not feasible to display the error analysis for each measurement.

The first example is of a sample with a moderately high contact resistance of 3.75 mΩ.cm^2. Table 2 shows the uncertainty budget for this measurement.

Source of Uncertainty	Value ±	Scaled Value ±	Probability Distribution	Divisor	Standard Uncertainty	Standard Uncertainty Squared
Voltage Measurement Keithley 2400 (V (@200 mV))	1.20E-05	8.70E-06	Rectangular	√3	5.02E-06	2.52E-11
Current Source Keithley 2400 (A (@10 mA))	2.00E-06	2.00E-04	Rectangular	√3	1.15E-04	1.33E-08
Cross Section Geometry Measurement (cm (@2.5mm))	2.00E-03	8.00E-03	Rectangular	√3	4.62E-03	4.27E-05
Standard Uncertainty of mean of 10 repeated readings (Ω (@1 mΩ))	6.00E-05	4.48E-04	Normal	1	2.59E-04	6.68E-08
Combined Standard Uncertainty (Ω.cm^2)			Normal			**2.45E-05**
Expanded Uncertainty (Ω.cm^2)			Normal (*k*=2)			**4.90E-05**

Table 2. Uncertainty budget for a contact resistance measurement in the range of 1 mΩ.cm^2.

The voltage measurement across the junction is measured at 1.38 V with a 10 mA current injected. This measurement is repeated 10 times for each point and the standard uncertainty of the mean value is extracted from this data, giving a resistance drop of 138 mΩ with and uncertainty value of ±0.06 mΩ. The geometric measurements are taken using digital callipers which have an uncertainty of ±0.01 mm when measuring in the 2.5 mm region [18]. The uncertainty values are all scaled by dividing the uncertainty value by the measured value. To express the scaled values to the same confidence level, assumptions were made about the distribution of measurements. For voltage, current and geometric measurements, where the uncertainty is supplied by the equipment manufacturers [19], the distribution is assumed to be uniform or '*rectangular*', i.e. the value of measurement is equally likely to fall anywhere within the stated error limits. The values for uncertainty were divided by √3 for these cases to calculate the standard uncertainty and because the cross sectional area involves two measurements, the square of the standard uncertainty is doubled. To calculate the combined standard uncertainty summation in quadrature is used. This value represents the confidence level of 68%, described as the coverage factor k = 1. This value is doubled to get the expanded uncertainty (k = 2) providing a level of confidence of approximately 95%.

Table 3 shows the uncertainty budget for a sample with a much lower contact resistance measurement of 30.10 μΩ.cm^2.

Source of Uncertainty	Value ±	Absolute Value ±	Probability Distribution	Divisor	Standard Uncertainty	Standard Uncertainty Squared
Voltage Measurement Keithley 2400 (V (@200 mV))	1.20E-05	1.71E-04	Rectangular	√3	9.90E-05	9.80E-09
Current Source Keithley 2400 (A (@10 mA))	2.00E-06	2.00E-04	Rectangular	√3	1.15E-04	1.33E-08
Cross Section Geometry Measurement (cm (@2.5mm))	2.00E-03	8.00E-03	Rectangular	√3	4.62E-03	4.27E-05
Standard Uncertainty of mean of 10 repeated readings (Ω (@1 mΩ))	5.00E-06	6.25E-04	Normal	1	3.61E-04	1.30E-07
Combined Standard Uncertainty ($\Omega.cm^2$)			Normal			**1.97E-07**
Expanded Uncertainty ($\Omega.cm^2$)			Normal (*k*=2)			**3.94E-07**

Table 3. Uncertainty budget for a contact resistance measurement in the range of 10 μΩ.cm2.

At lower contact resistances the standard uncertainties were increased as the limits of accuracy for the measurement equipment is approached. Voltage measurements were taken at the lowest end of the resolution scale for the Keithley 2400 and so the expanded uncertainty is still accurate. For measurements much lower than 10 $\mu\Omega.cm^2$ it is expected that more accurate equipment would be necessary.

To reduce the error in contact resistance measurements, more accurate geometric analysis equipment would be necessary as the error is dominated by the cross sectional area measurement. Furthermore, a source of error in the positioning of the measurement probes for four wire analysis may have a dominant effect when the contact resistance is less than 10 $\mu\Omega.cm^2$. Currently the effective value of contact resistivity is much higher than the bulk resistivity of the material. As the contact resistance reduces, the two values converge, meaning that the probe positioning accuracy becomes much more important. Accurate computerised positioning equipment could be used to reduce the user error in positioning or the probe could be dragged along the surface. The latter approach would require a form of high frequency sampling which may reduce measurement time but could produce additional sources of error i.e. the probe bouncing or causing debris to collect at the leading edge of the probe. As the uncertainty for probe positioning was unknown in this measurement, and because of the small effect it has on the measurement uncertainty, it was not included in the calculation. For future improvements to the contact resistance measurement equipment the effect of probe positioning will be characterised and the equipment will be modified to reduce the uncertainty.

2.5.3 Module Characterisation Equipment

To measure matched load output performance of a module at a given temperature differential, a module test rig is used. This equipment and the accompanying control programme was developed by Glasgow University. The test rig comprises of a hot copper block and water cooled heat exchanger that is coupled together using a compression spring system. A module is placed between the hot copper block and water cooled exchanger and a clamping force is applied by the compression spring. The clamping force is measured using an in-line pressure transducer located under the spring. The heated copper block contains a silicon carbide heating element that is powered by an Agilent power supply. The coolant is supplied from a chiller system that maintains a coolant temperature and continually circulates the fluid. Thermocouples are integrated into the hot and cold blocks and in the coolant line. Coolant flow is recorded using an integrated flow meter in the coolant loop. The module output wires are connected to an Agilent load cell. The module clamping system can be seen in Figure 22. The setup is controlled by an Agilent Vee control programme that interfaces with the equipment through an Agilent data recorder. The programme prompts for a temperature differential and load step value in Amps for the resistance sweep applied by the load cell. In operation, the system monitors the temperature differential and regulates the power supplied to the heater block to achieve a steady temperature differential. A feedback loop from the integrated thermocouples is used to achieve this. The differential on the module is applied in open circuit mode. Once the temperature differential is reached, and the system is at steady state, the load cell applies a calculated electrical resistance to the module and the voltage and current is recorded. The resistance is increased incrementally, and voltage-current characteristics are recorded. When the resistance is increased, a higher current output is recorded. The increase in current causes the overall thermal properties of the module to change due to the Peltier effect. As a result, continual monitoring of the heater power has to be carried out by the programme to maintain a constant temperature differential.

The data collected is transferred into an excel document for analysis. From this data, an I-V curve can be plotted and module power can be calculated. The maximum power output point can be obtained from the graph that is located at the peak of the power curve.

Figure 22. Module characterisation test rig. This equipment is developed by a group at the University of Glasgow.

2.6 Thermoelectric Lab Overview and Summary

A thermoelectric lab has been implemented in European Thermodynamics Ltd which enables research into thermoelectric joining and prototype module manufacture to be carried out. The lab comprises material processing equipment such as semiconductor sectioning apparatus which is used for producing pellets for joining trials and prototype module manufacturing. Brazing and soldering trial equipment was developed which includes a tube furnace and enclosures which are specifically designed for carrying out trials under different atmospheres. Lastly, bespoke characterisation equipment for joining trials and prototype modules was designed and built for verification and comparison of samples.

Figure 23. Overview picture of the lab developed and installed at European Thermodynamics Ltd.

Figure 23 is an image of the lab at European Thermodynamics. On the left of the image is the cutting and sample storage area. Material processing is carried out here for grinding and cutting of the semiconductor samples. To the right of the image is the furnace used for brazing trials and prototype module manufacture. The characterisation equipment is positioned outside of the lab in more stable environmental conditions.

The thermoelectric lab contains all of the necessary equipment to carry out joining trials and prototype module manufacture effectively. This lab is used for the development of a silicide thermoelectric module which is reported in the subsequent chapters of this thesis.

3 Literature Survey

The focus of this study is to develop a joining process for a mid-temperature thermoelectric material and subsequently build a prototype module. To identify a suitable thermoelectric material, a survey of the literature for the state of the art thermoelectric materials was carried out. N-type magnesium silicide and p-type higher manganese silicide were chosen as the most suitable candidates for this study.

Papers for bismuth telluride, skutterudites, half heuslers, lead telluride and silicide materials are discussed and the key characteristics of the materials are compared and summarised thereafter. Lastly, a review of the literature based on module prototyping for silicide materials was carried out to identify the current state of the art for this study.

3.1 Bismuth Telluride

Bismuth Telluride is the state of the art commercial thermoelectric material for low-temperature energy harvesting [20]. It forms a tetragonal/rhombohedral crystal structure with five atoms in one unit cell and due to this crystal nature it cleaves easily in the trigonal axis due to Tellurium-Tellurium Van Der Waals bonds [21]. A method for increasing the structural properties is to produce polycrystalline alloys of the material that in turn enhances the thermoelectric properties of the material. Increasing grain structure within thermoelectric materials has been shown to reduce the phonon conduction of heat through the material, thus lowering the thermal conductivity [22]. It is desirable for this parameter to be minimised in thermoelectric materials as the core working function is dependent on a thermal gradient being maintained across the material. Efforts to nanostructure these materials using ball milling and SPS techniques have been employed to reduce thermal conductivity and optimise thermoelectric performance due to increased phonon scattering from grain boundaries. A consideration when nano-structuring these materials is the implication of reducing electronic conductivity as this approach leads to modification of the effective carrier concentration and thus the energy of Fermi levels which are key to the semiconducting properties. Furthermore, attempts to modify the structure of BiTe by using a substrate of carbon nanotubes and mechanical exfoliation techniques for quasi 2D atomic trilayers and bilayers have been reported [23].

Typically, a dimensionless figure of merit (ZT) of 1 is achieved at 473 K with standard Bismuth Telluride, which can be doped to exhibit p-type or n-type semiconducting properties [24]. The maximum working temperature of Bismuth Telluride is in the region 550 K,

beyond this the material is severely and irreversibly damaged due to oxidation and sublimation. The melting temperature is approximately 850 K, which makes it unsuitable for applications such as energy generation from waste heat in industrial processes. Furthermore, the cost and limited abundance of the raw materials would mean that heavy production would exhaust the world's supply rapidly [25].

Although BiTe is unsuitable for high-temperature energy harvesting, it is important to include it in this account as it is a well-characterised material. Developments made with this material may be directly transferrable to other materials that are more suited to high-temperature energy generation with similar structures.

Poudel *et al* report a synthesis route for nanopowders of bismuth telluride by means of nano-precipitation. The material is then densified using Spark Plasma Sintering (SPS) creating a semiconducting material with an average grain size of ~90 nm. This material was reported to have a peak ZT of 1.1 at 340 K and showed a 30% increase in power factor compared to the previous state of the art [26]. Conversely, a more scalable technique has been developed by which ball milling is used to produce a nano-powder of p-type doped bismuth antimony telluride that is densified by SPS. Reports show that a peak ZT of 1.4 is achieved at 373 K and 1.2 and 0.8 at room temperature and 523K respectively [27].

A recent study into improving the mechanical properties of bismuth telluride using nano-inclusions is reported by Williams *et al* [28]. The inclusion of nano-boron carbide particles is shown to increase the Vickers hardness of a p-type $Bi_{0.5}Sb_{1.5}Te_3$ sample by 27% over a sample produced without boron carbide, with no effect on ZT.

Although bismuth telluride is a low-temperature thermoelectric material, the recent research shows us that by modifying processing techniques, the thermoelectric performance of the material can be improved. Addressing problems with mechanical properties using the approaches above, may be transferable to mid-temperature materials that are more suited for industrial waste heat applications.

3.2 Skutterudites

Skutterudites follow the general formula RM_4X_{12}, where *X* represents P, As, or Sb; *M* represents Fe, Ru, or Os; and *R* represents La, Ce, Pr, Nd, or Eu. These compounds are body-centred cubic with 34 atoms in the conventional unit cell but sometimes the primitive unit cell is taken to have only 17 atoms. This structure is described as consisting of square planar rings of four pnicogen atoms (*X*) with the rings oriented along either the [100], [010], or

[001] crystallographic directions. The metal (*M*) atoms form a simple cubic sub lattice and the *R* atoms are positioned in the two remaining cells. This structure is desirable for thermoelectric materials as the square planar rings in the oversized cell can oscillate anharmonically, which dissipates the low-frequency phononic contribution to thermal conductivity. This is termed the 'rattler' structure or 'Einstein Oscillator' and has shown to produce a phonon glass but it is unclear whether an electron crystal can be achieved. One approach is to fill partially with a heavy Lanthanide group atom like ytterbium, cerium or thallium. This method has been reported to produce materials that have relatively good electrical properties and significantly lower thermal conductivity compared to an undoped equivalent [4, 29, 30].

An example of two complementary skutterudite materials is presented in separate papers by H.Ning *et al* and G.S.Nolas *et al*. The two skutterudite materials CeFeCoSb and YbCoSb are both produced by the same general method. The raw materials are mixed in their stoichiometric amounts and are slowly heated under vacuum followed by quenching in water. The material now has a homogeneous spread of the constituents but the correct crystal phases are not achieved. Ball milling and annealing produces the dense polycrystalline phase that is required. Measurements of the Lattice thermal conductivity for both materials show similar values in the region of 2.5 to 5 W/mK over a range of 0 to 300 K. This represents a significant reduction of thermal conductivity in comparison to the un-doped samples.

Both materials exhibit similar Seebeck coefficients, resistivity's and ZT's in the desired working range of 300 K to >700 K. From the data displayed in Figure 27Figure 24 to Figure 27 we can see that the two materials complement each other as p and n junction materials for module production. Their thermoelectric properties follow similar trends up to 600-700 K, which is a useful temperature for industrial energy harvesting. It is important to consider effects on the material from exceeding these temperatures. Taking the material to higher temperatures may cause oxidation or sublimation of phases within the material which in turn would decrease the thermoelectric properties [4, 29].

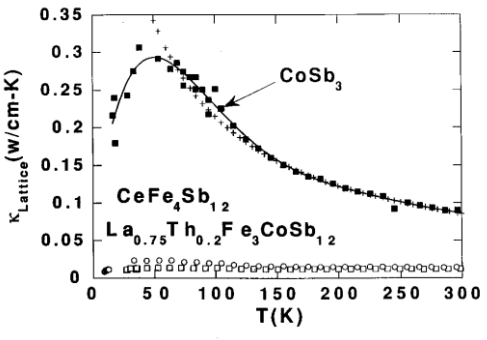

Figure 24. Lattice thermal conductivity for CeFeSb represented by open circles[4].

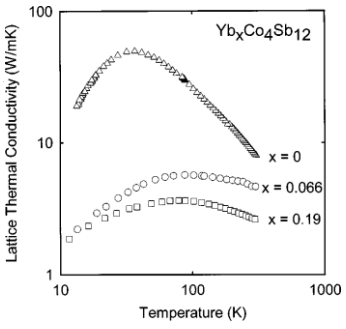

Figure 25. Lattice thermal conductivity for Yb(19%)CoSb represented by open squares[29].

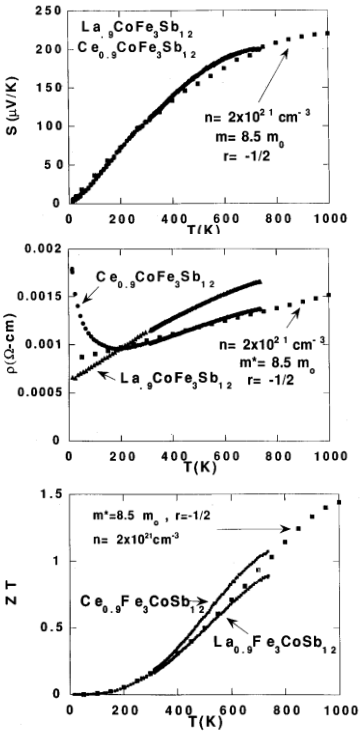

Figure 26. Seebeck coefficient, resistivity and ZT plots for CeFeSb[4].

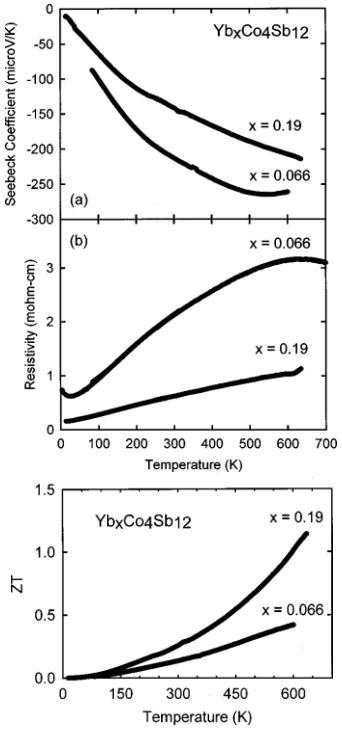

Figure 27. Seebeck coefficient, resistivity and ZT of YbCoSb[29].

A study into the oxidation effect of $CoSb_3$ in air from 500°C to 650°C (770K – 920K) has shown that sublimation of Sb_2O_3 occurs at 650°C causing rapid weight loss of the sample. At temperatures leading up to 650°C, the oxidation characteristics obey a parabolic law. Inevitably, after high-temperature treatment the materials thermoelectric properties are significantly reduced. Interestingly, after treatment for 48h at 500°C there is only a very minimal drop in thermoelectric properties, especially in ZT when compared to a pre-treated sample [28].

Another pair of skutterudite materials for thermoelectric generation are Ni-doped CeFeSb (p-type) and Co(SbTe) (n-type). NiCeFeSb serves as a strong p-type semiconducting material as iron has one less electron than cobalt. Therefore the unit cell will effectively have four fewer electrons than more common skutterudite materials. Nickel doping modifies the electron structure and introduces scattering sites for phonons. Coupled with its greater solubility in the structure compared to cobalt this material has great potential for high-temperature energy generation. Heavily tellurium doped cobalt antimonide beyond the 0.25% theoretical solubility limit produces an n-type semiconductor with 'rattler' sites filled with the heavy tellurium atoms. Like NiCeFeSb, CoSbTe has a modified electron structure due to doping

and inclusions in the unit cell that cause a decrease in thermal conductivity, this is essential for effective thermoelectric conversion.

The two skutterudite materials exhibit similar thermoelectric properties over the temperature range 300-800 K, both produced using the same method of stoichiometric mixing, annealing, powdering and then spark plasma sintering. The CeFeNiSb material is compared to CeFeCoSb when measuring thermal conductivity; slightly lowered thermal conductivity is observed with its greatest effect being seen at higher temperatures within the range of 0.8 to 1.4 W/mK [31, 32].

Figure 28Figure 31 show that similar Seebeck potentials are observed in the region of ±180 to 200 μV/K for each material and ZT approaches 0.8 at higher temperatures. For these materials to be seriously considered for high-temperature thermoelectric generation, the ZT curve would have to be significantly flattened as a steep range of ZT is observed for both materials over the temperature range. This indicates that efficiency would be very low over large temperature variations.

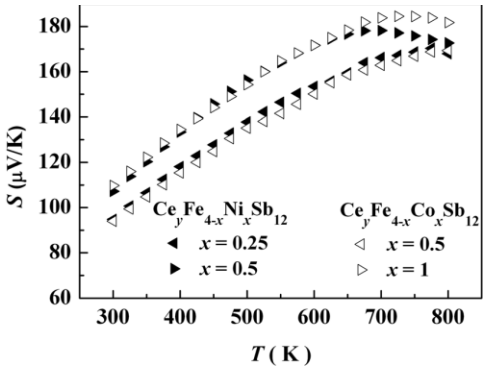

Figure 28. Seebeck coefficient for CeFeNiSb and CeFeCoSb[31].

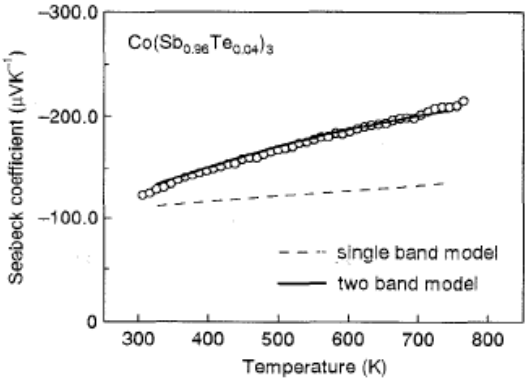

Figure 29. Seebeck coefficient for CoSbTe[32].

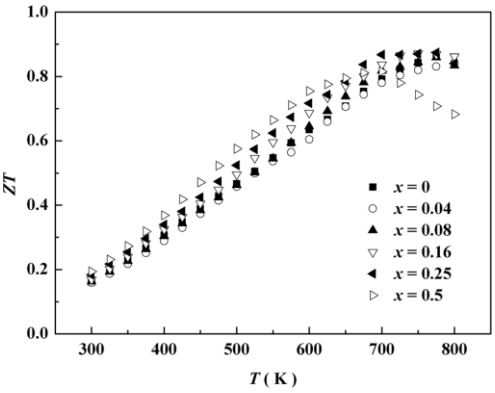

Figure 30. ZT curve for CeFeNiSb with varying amounts of Nickel[31].

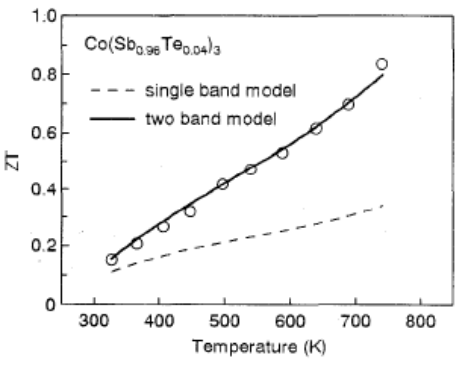

Figure 31. ZT curve for CoSbTe[29].

Skutterudite materials show great promise for high-temperature thermoelectric generation applications. Currently, more research needs to be carried out on the materials with the aim to flatten the ZT curve. This could be achieved by changing doping levels along the material to functionally grade it, achieving higher ZT at all temperature points. Secondly, coating or atmospheric properties for these materials need to be considered as gassing of certain constituents may occur at higher temperatures due to oxidation and sublimation.

3.3 Half Heusler

The Half Heusler structure comprises a cubic orientation with four of the eight vacancy spots filled with a transition metal atom. Typical compounds are MCoSb and MNiSn where M can be titanium, zirconium or hafnium singularly or in combination. Half Heusler materials have shown promise for thermoelectric generation but have recently shown to have lower performance than other state of the art materials. This is partly to do with the advances in other materials that can be filled with phonon dispersing atoms that can anharmonically vibrate in their cells, lowering the thermal conduction. This method cannot be employed in the Half Heusler material so efforts have to be focussed on reducing the thermal conductivity by a different approach. Grain boundaries in materials are known to scatter phonons, which in turn reduces the thermal conductivity of the material. In focusing efforts toward nano-structuring of the material, the ZT of Half Heuslers can be increased as phonon scattering is amplified due to a greater density of grain boundaries present in the material [33, 34].

HfZr(NiSn)Sb is an n-type Half Heusler thermoelectric material which typically has a ZT of 0.8 between 600-700^{o}C (873-973K). Producing this material using a nano-particulate method has been reported to give a 25% increase in ZT to unity. This method involves arc melting the constituents in a stoichiometric mixture to produce an ingot; this is then ball milled to produce a nano-particulate powder. Final densification is carried out using direct current hot-pressing that produces bulk samples with nano-sized grains in the region of 100nm [31].

Figure 32 shows the experimental properties of the nanostructured HfZr(NiSn)Sb. It can clearly be seen in each case that nano-structuring and densification enhance the properties of the material in most cases. As expected, the thermal conductivity of the material is decreased due to nano-structuring, a compromise to this enhancement is the decrease in electrical conductivity due to the reduction in effective carrier concentration. This arises due to the fact that a greater proportion of the material is comprised of grain boundary phase material and so there is less contribution to the conduction band. What is achieved in this case is the fine

tuning of these properties between the thermal and electrical conductivity which leads to a greater ZT.

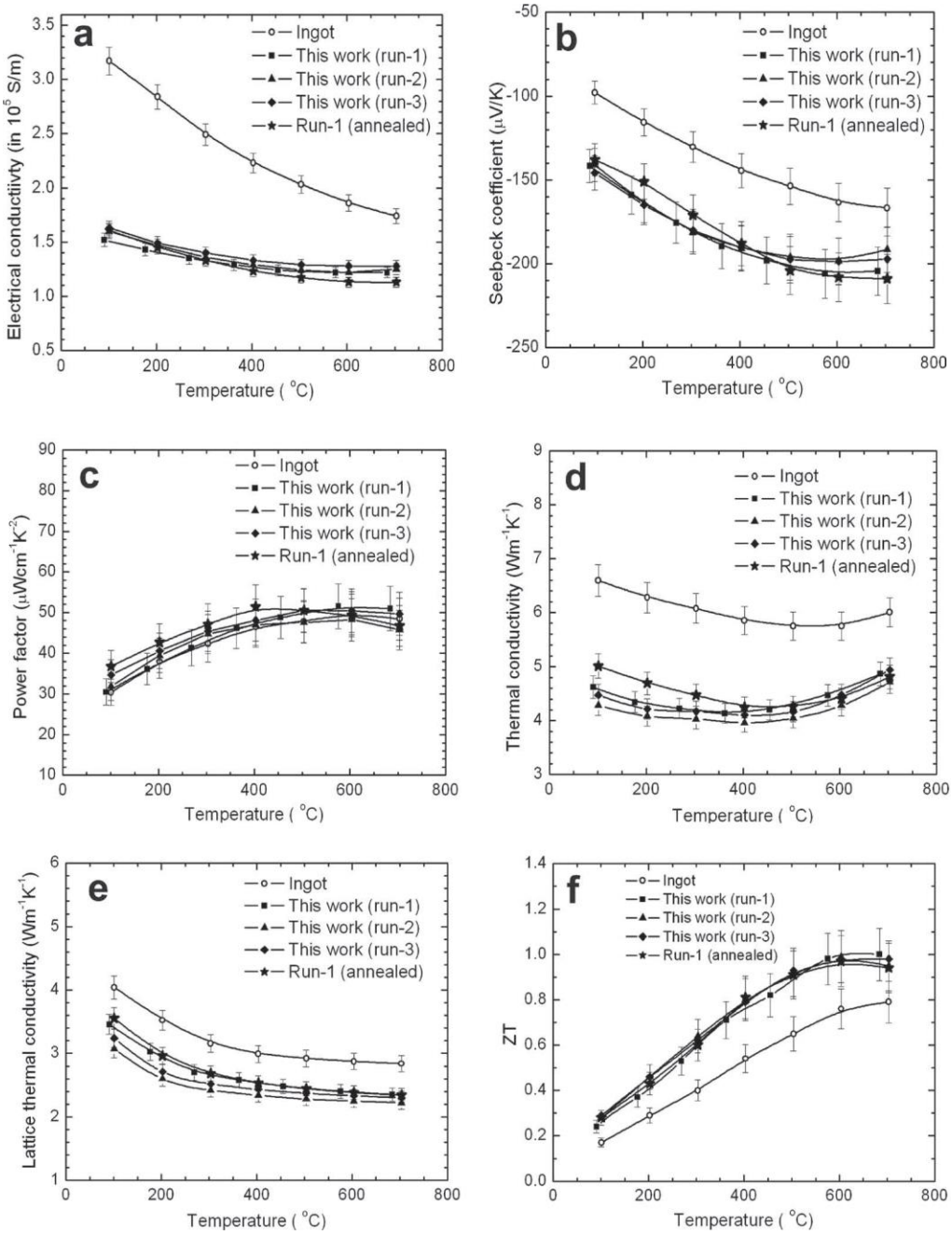

Figure 32.a) Temperature-dependent electrical conductivity, b) Seebeck coefficient, c) power factor, d) total thermal conductivity, e) lattice thermal conductivity, and f) ZT values of three nanostructured Hf 0.75 Zr 0.25 NiSn 0.99 Sb 0.01 samples, and the sample annealed at 800 ° C for 12 hours in air; the line is for viewing guidance only, for comparison with the ingot sample (open circles) which matches the previous state of the art n-type half-Heusler composition[31].

The same group then turned their focus on enhancing the properties of a p-type Half Heusler compound using the same method. ZrHf(CoSb)Sn is a p-type thermoelectric compound with a typical ZT in the region of 0.5 at 700C (973K), after employing the method to produce nanoparticulate ingots of this material the ZT was measured to be in the region of 0.8 at

700°C, this constitutes a 60% increase in performance [32]. Figure 33 shows the change in properties due to the enhanced production process.

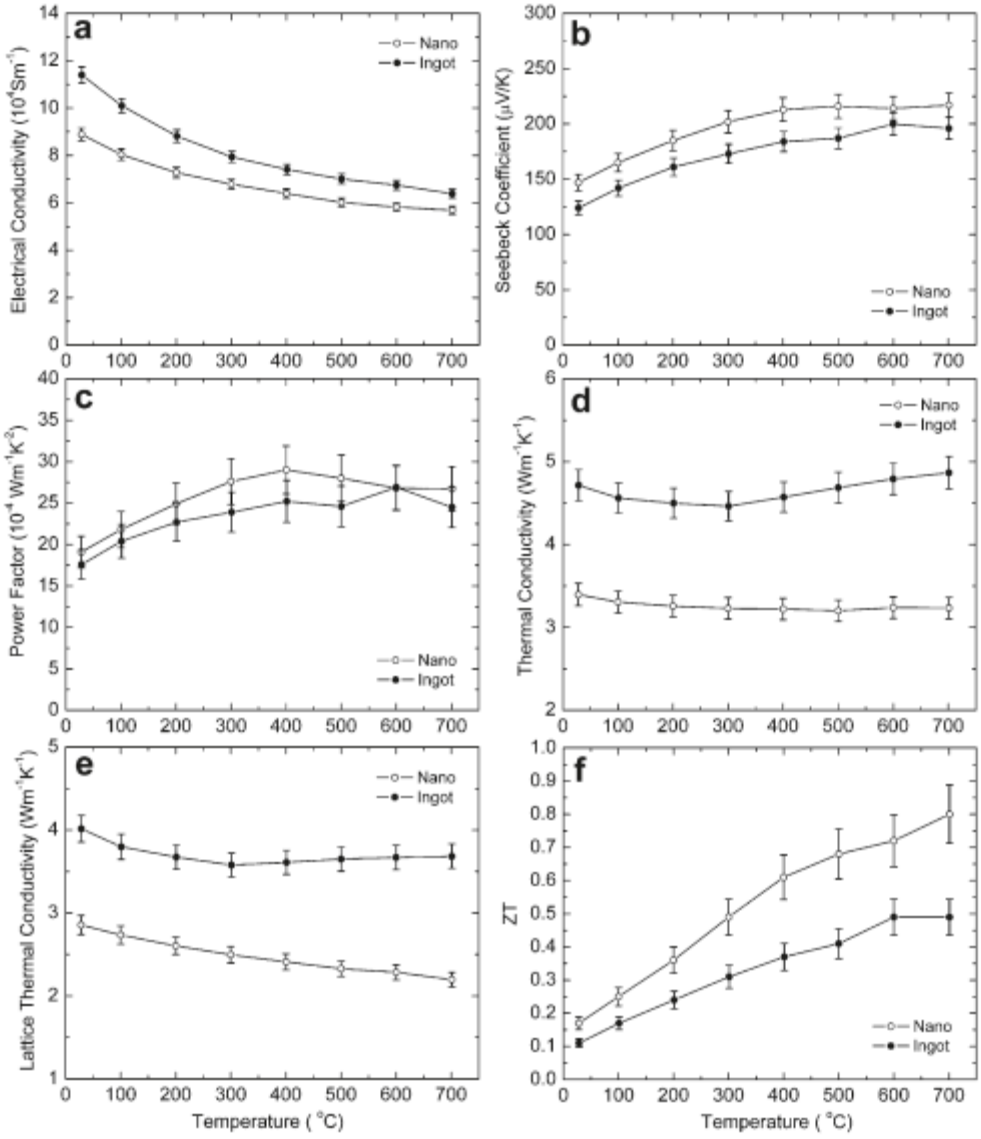

Figure 33. Temperature-dependent (a) electrical conductivity, (b) Seebeck coefficient, (c) power factor, (d) total thermal conductivity, (e) lattice part of thermal conductivity, and (f) ZT of ball-milled and hot-pressed sample in comparison with that of the ingot[32].

The two HH compounds have ZTs in similar regions and show an effective method of optimising performance of these materials. Further studies need to be carried out to achieve particulate sizes below 100nm while reducing thermal conductivity but making sure the expense of carrier mobility is not too great.

3.4 Lead Telluride

Lead Telluride is a thermoelectric material that has the same single phase cubic structure as NaCl, with a typical working temperature range of 50-500^{o}C (323-773 K). The material boasts good thermoelectric properties in this temperature range, with a peak ZT of 0.8 for single phase lead telluride and figure of merits in the region of double this for modified lead telluride structures.

The greatest advancements in performance for lead telluride have been made by alloying of the material with other components such as lead iodide and germanium telluride. More recently, nano-structuring of thermoelectric lead telluride material has become a more popular mode of study facilitated by the advancements in nanotechnology.

Lead telluride has been used as a thermoelectric generation material since the 60s in space missions for use in radioisotope thermoelectric generators or RTGs. Silicon germanium later replaced lead telluride as a TE generating material for RTGs [2]. As of yet there have been very few accounts of this material being used for terrestrial energy generation due to the toxicity of lead. An argument in favour of the use of lead telluride for terrestrial use is in analogy with table salt (NaCl), separately Sodium and Chlorine are two dangerous materials but when combined become relatively inert. Much of the same is said about lead telluride as it is a stable material in its working temperature range, albeit ingestion is not recommended.

A method for producing n-type lead telluride using indium doping has been developed by Y.Gelbstein *et al*. Dopant concentrations of 0.1, 0.5, 1 and 3 at% were tested and produced by the following procedure: Casting of elemental material under vacuum of 10^{-5} Torr at 950C for 10 mins followed by water quenching, attrition milling to powder form, cold compacting and final sintering at 625^{o}C for 3 hours followed by 15 minutes at 725^{o}C. Alongside this experiment, lead iodide filled samples of lead telluride are tested and compared to previous studies in the context of carrier concentration. The study shows that lead iodide filled samples of lead telluride can be produced to a good standard of performance by direct scale up of previously used techniques. Doping with 0.1 at% indium gives the best thermoelectric properties in the temperature range 300-700 K, showing consistent ZT between 1.4 to 1.6 as shown in Figure 34 [31].

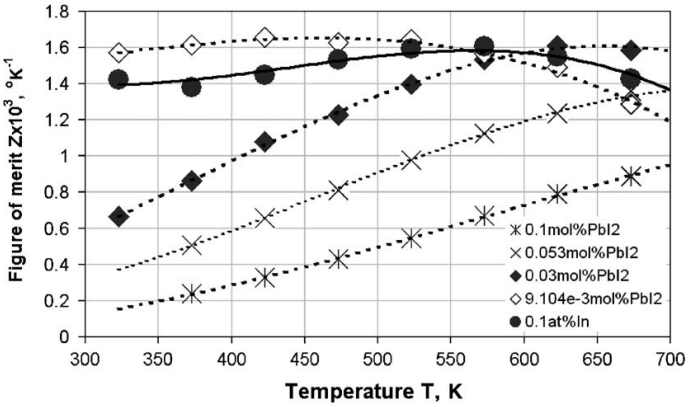

Figure 34. The temperature dependence of the figure merit for 0.1 at% In-doped PbTe sample (solid curve) and of PbI2- doped PbTe samples (dotted curves)[31].

Germanium lead telluride alloyed with bismuth telluride has been shown to exhibit high ZT values at temperatures up to 500°C. This material is made by cold pressing, annealing, milling and sintering by SPS. It has a grain structure with maximum grain size of 200μm, equivalent to a 60-mesh powder. In comparison to current studies, this grain size is large but this is combined with molecular inclusions of bismuth telluride, which causes extra sites for phonon scattering. Hence, the following ZT curve is achieved from different compositions shown in Figure 35 [32].

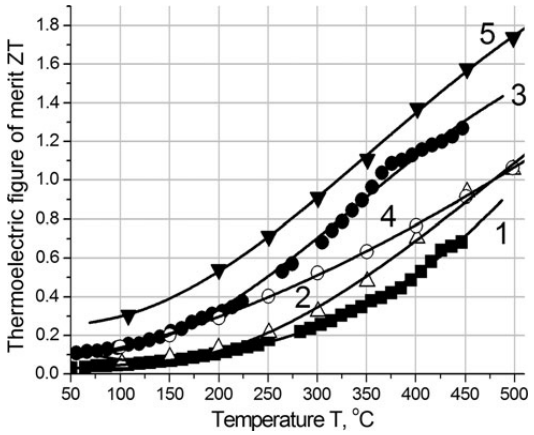

(1) GeTe,
(2) $Pb_{0.05}Ge_{0.95}Te$,
(3) $(GeTe)_{0.95}(Bi_2Te_3)_{0.05}$,
(4) $Pb_{0.13}Ge_{0.87}Te$
(5) $Pb_{0.13}Ge_{0.87}Te$ + 3 mol% Bi_2Te_3.

Figure 35. Temperature dependence of different compositional alloys with thermoelectric figure of merit[32].

It can be seen that the binary compositions give best thermoelectric properties. A problem with these materials is that the curve for the material is very steep and so the material will only exhibit a useful thermoelectric performance in a small operating band. It would be recommended that future studies in this material should be concentrated on flattening the ZT curve. This is likely to be achieved by functionally grading the material. This involves

modifying the dopant levels in the material along the axis parallel to the thermal gradient so that the thermoelectric properties are maximised at all temperature points along the axis [35].

B. Yu *et al* found that by doping lead telluride with thallium, large increases in ZT can be observed. Although a completely experimental exercise, due to the extremely high toxicity of thallium, it is an important study for developing a process of production for this material, as in later research studies efforts to replace thallium with a more suitable dopant can be made.

Stoichiometric amounts of thallium, lead and tellurium are prepared by ball milling to produce an alloy powder. These powders are then hot pressed using direct current to produce dense discs of the material. Figure 36 shows the measured properties of the final material compared to a reference material. The material is only tested up to 400°C as softening of the sample occurs beyond this temperature. A peak ZT value of 1.3 is measured at 400°C, but it is plotted on a steep curve ranging from 0.5 at 200°C, giving it an average ZT of 0.8 over this range. Improvements to these values could be achieved by decreasing the grain size into the nanoscale, which may also change the high-temperature physical characteristics [36].

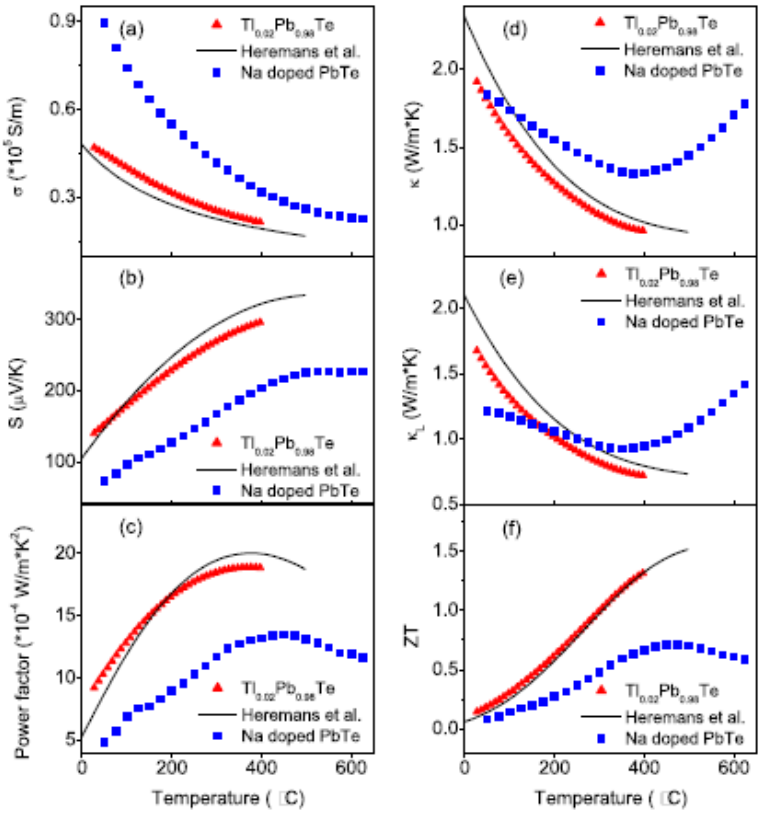

Figure 36. a) Electrical conductivity, b) Seebeck coefficient S, c) power factor, d) thermal conductivity, e) lattice thermal conductivity L, and f) dimensionless figure-of-merit ZT dependence of temperature of the hot-pressed dense bulk samples Tl0.02Pb0.98Te and a reference sample of Na-doped p-type PbTe[36].

Lead telluride holds great potential for thermoelectric power generation. The high ZT reaching 1.5 in the temperature range of 300K-700K makes it one of the highest performing materials of its kind. Disadvantages of this material are that its constituents are known to be harmful in their elemental form and tellurium is a rare earth element so long-term use may not be possible due to supply or price. Publications have been released [10, 37-39] showing how modules can be fabricated using this material although protection of the material is not mentioned. The stability of lead telluride at high temperatures is not as good as alternative materials due to sublimation and softening of the material. Separate studies would have to be conducted to explore functional coatings to combat sublimation and oxidation of this material.

3.5 Silicides

Higher manganese silicide (HMS, p-type) is commonly coupled with magnesium silicide (n-type) to form thermocouples. They are typically designed for a working range of 573-873K (higher for HMS) and exhibit similar thermoelectric properties throughout this range due to their mutual tetragonal crystal structure. The crystal structure is moderately complicated due to the many different compositions that occur with silicides. Often, a Nowotny chimney ladder phase is exhibited in silicides that consist of the metallic material forming a central tetragonal ladder that is surrounded by the Silicon atoms in a helical 'chimney' formation encasing the system [40]. Recent studies into doping these materials to improve the thermoelectric properties have centralised around the use of group 13 and 14 elements [41]. The advantage of these materials is that they are relatively low cost and consist of safe materials. Coupled with their high-temperature tolerance; this makes them a very desirable set of TE materials to work with.

A standard problem with Mg_2Si production is the difficulty in producing the phase by ball milling. It is possible to produce this phase in the lab but a more scalable industrial method needs to be developed. Research groups have failed to produce clean phases of this even with 100's or 1000's of hours of ball milling. More recently, an incremental milling procedure has been developed [S.K. Bux *et al*] which can produce a clean Mg_2Si phase in less than 8 hours. In this case, the dopant is bismuth is added in a stoichiometric amount with silicon. The magnesium is added at intervals during the milling process in 200 mg increments to produce a single phase Mg_2BiSi powder that is hot pressed into a dense disc. Figure 37Figure 38 show the properties of this material [42].

Another well-known issue for Mg_2Si is the sublimation limit of 775 K. The thermoelectric properties of this material were tested up to this temperature and a maximum ZT of 0.7 was

measured. The low ZT was caused by a particularly high thermal conductivity, which was unexpected for this type of synthesis technique. Analysis showed that the high thermal conductivity was caused by grain growth/coelescence during the compaction stage. Due to the reduction of grain boundry scattering of phonons the thermal conductivity was similar to that of bulk polycrystalline magnesium silicide.

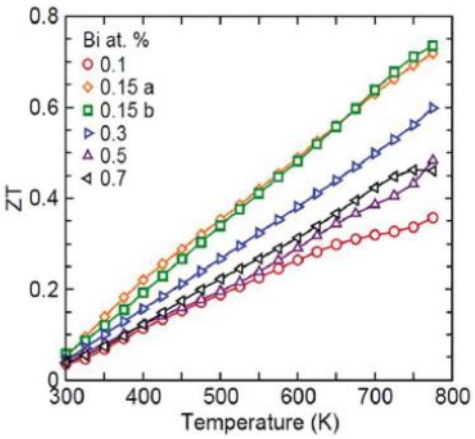

Figure 37. ZT curve for Magnesium Silicide with varying dopant levels of Bismuth[42].

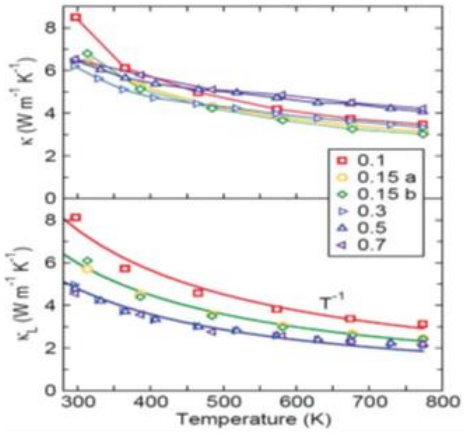

Figure 38. Thermal conductivity and the lattice parameter of the thermal conductivity against temperature for optimised MgBiSi samples[42].

Zaitsev *et al* showed how a ZTmax of 1.1 can be achieved by doping of magnesium silicide with tin. They claim for this to be a very reproducible result, having repeated the study numerous times. Magnesium, silicon and tin is directly melted followed by 'long-time annealing' to induce homogeneity in the material. Although not stated in the literature, annealing processes typically take a number of hours or days [43, 44] meaning the process is less likely to be suitable for industrial scale manufacture. Nonetheless, this material has shown to have a high ZT, comparable to lead telluride and cobalt antimonide, as shown in Figure 39, and is comprised of environmentally friendly materials [45]. A possible route for further study would be in ball milling of the constituents, possibly incrementally as described by Bux *et al* [46], with high energies to get a small grain structure.

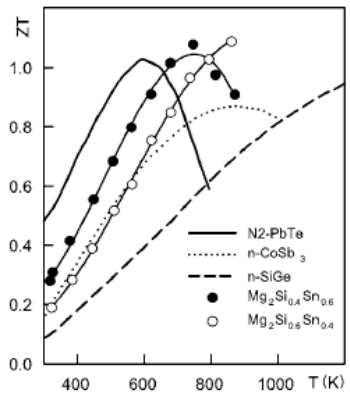

Figure 39. Comparison of best modern day TE materials to Tin loaded Magnesium Silicide samples[45].

Similarly to magnesium silicide, ball milling of higher manganese silicides (HMS) is also difficult. Gaining a single phase of manganese silicide with no oxidation had proven to be very demanding, even when the process carried out in an inert atmosphere. Zhou *et al* explored doping HMS with germanium and aluminium to tune the transport properties of the material. The addition of germanium resulted in a change to the microstructure due to modification of the Nowotny chimney structure spacing, which in turn modified the electrical and thermal properties. Two possible routes for the link between the microstructure and the resulting modification of electrical and thermal properties were proposed. Reports [47, 48] indicated that the band structure for HMS was directly affected by the position of Si atoms in the basic unit cell. In the case of germanium addition, this might have disturbed the arrangement of the Si sub cells leading to stacking faults. Alternatively, second phases of Si-Ge could also affect the carrier concentration and hence the electrical and thermal properties.

Stoichiometric amounts of manganese, silicon and germanium are melted together using an induction furnace at 1350^{o}C producing ingots that are ground with an agate mortar and pestle to a maximum grain size of 0.04 mm. Hot pressing is used to produce the final densified puck. The two best performing dopant levels were 0.8% and 1.6% ratio germanium to silicon, at which carrier concentration peaked. The dopant levels and Seebeck coefficient followed similar trends and so the difference in final ZT value was dictated by the thermal conductivity. It is revealed that the 0.8% dopant sample is the highest performing due to its considerably low thermal conductivity in comparison to the 1.6% sample. Figure 40 shows the differential in ZT over the temperature range measured up to 650^{o}C [42]. This may have occurred due to the increase in charge carriers causing an increase in phonon heat conduction.

More recent work by Luo *et al* builds on the fact that doping with aluminium will increase the carrier concentration in comparison to germanium doping, as aluminium provides fewer valence electrons. The method used to produce this material uses a stoichiometric mixture of

silicon, manganese and aluminium melted together using induction heating. This molten mixture is rapidly cooled using melt spinning and is pulverised into a powder for densification by SPS. The best performing dopant level was the 0.0015 ratio of aluminium to silicon sample. Although this material gave one of the lowest Seebeck coefficients in comparison to the other samples, its thermal conductivity was significantly lower than other samples giving it a peak dimensionless figure of merit of 0.65 at 850 K as shown in Figure 41 [45].

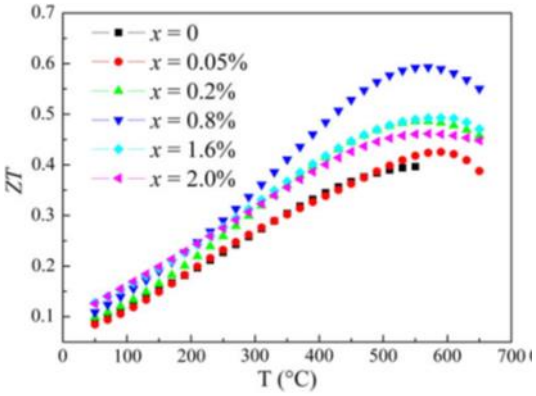

Figure 40. Temperature dependence of ZT for Mn(Si1-xGex)1.80[42].

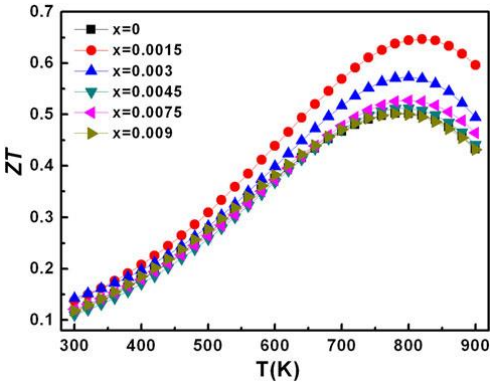

Figure 41. Temperature dependence of ZT for MnSiAl[45].

The following materials described are both used in this study for the development of a mid-temperature thermoelectric device.

The first material used to produce a prototype module is antimony doped magnesium silicide with un-doped higher manganese silicide; developed by Tokyo University of Science and supplied by Toyota and Yasunaga of Japan. This material is of interest as a large amount of work has been carried out to form nickel electrodes on the antimony doped magnesium silicide in particular. Nickel electrode formation on higher manganese silicide is trivial in comparison.

Monobloc sintering, also termed plasma-activated sintering (PAS), is used to form nickel electrodes onto the magnesium silicide pucks. This sintering method differs from SPS (described in section 1.1.2) as the plasma formed at the surface of the powder particles has a ‘cleaning’ effect, removing previously formed oxide particles or trapped gasses [49]. The sintering method uses a diffusion bonding approach to sinter the magnesium silicide powder with the addition of nickel powder or foil to the top and bottom faces of the puck.

The sintering process outlined in Figure 42a includes an additional powdered silicon oxide layer to avoid evaporation of nickel during sintering. The sintering is carried out at 1113 K for 5 minutes with a pressure of 30 MPa under an Argon atmosphere. The resulting cross section of the sample shows no significant reaction or diffusion at the interface shown in Figure 42b [50]. The equivalent material is supplied from the group for use in joining tests

(chapter 4.2) with higher manganese silicide contacted with nickel using the monobloc sintering process.

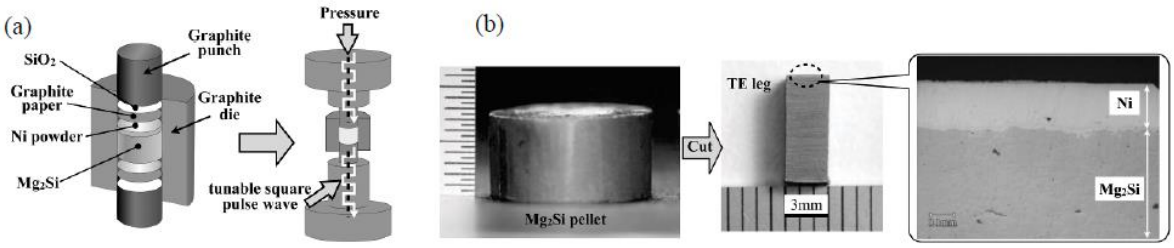

Figure 42. a) Setup for monobloc sintering of magnesium silicide and nickel electrodes. b) micrograph of Ni/MgSi interface of monobloc sintered sample[50].

Performance data is not reported in this paper but the corresponding data is supplied by Yasunaga and Toyota-Tsusho. Figure 43 displays the ZT curve against temperature for the MgSbSi, with a peak ZT 0.51 at 850 K.

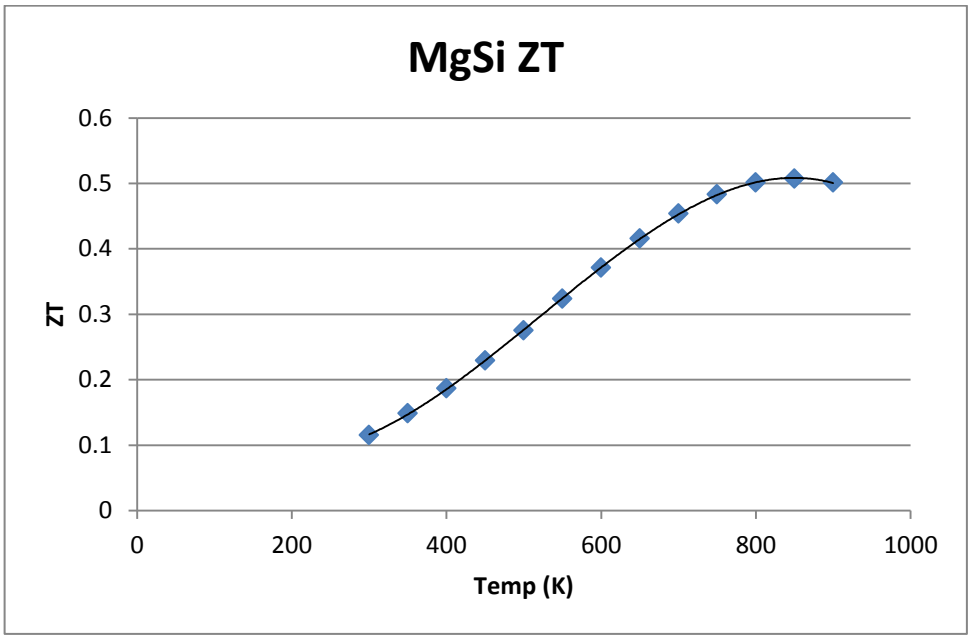

Figure 43. ZT curve for Antimony doped Magnesium Silicide (data provided by Yasunaga and Toyota-Tsusho).

The second material used in this study is prepared by IntrinsiQ materials, London, and Queen Mary University, London (QMUL/IML). Spark plasma sintering was used to consolidate a tin and antimony doped magnesium silicide alloy. Doping with tin leads to an increase in ZT for magnesium silicide but increases the reactivity of the material at elevated temperatures. The group report a maximum ZT of 1.39 when sintering at 1023 K under a pressure of 50 MPa for 3 minutes [5]. Due to the reactivity of this alloy and lower sintering temperature, it is not

possible to apply a barrier layer via the approach reported by Sakamoto *et al*. Nonetheless, the recorded ZT is marginally higher than the state of the art value of 1.0 – 1.3 [5, 51, 52].

In the same paper, the group also report a further advancement in ZT by using pressure-less sintering. Pressure-less sintering uses SPS equipment without the uniaxial pressing of the sample. The process induces porosity into the material that in turn reduces the thermal conductivity [53]. A peak ZT of 1.63 was measured at approximately 615 K for a porous sample with a relative density of 63%. Sintering was carried out at 1123 K for 2 minutes under a vacuum pressure of 5Pa [5] and the corresponding ZT curves are displayed in Figure 44. The increase in ZT arises from a decrease in thermal conductivity. Unexpectedly, the Seebeck coefficient was also enhanced. The cause for the increase in Seebeck coefficient is unclear, but it is likely to arise from a modification of band structure and carrier concentrations due to changes in the microstructure as described in [47, 48].

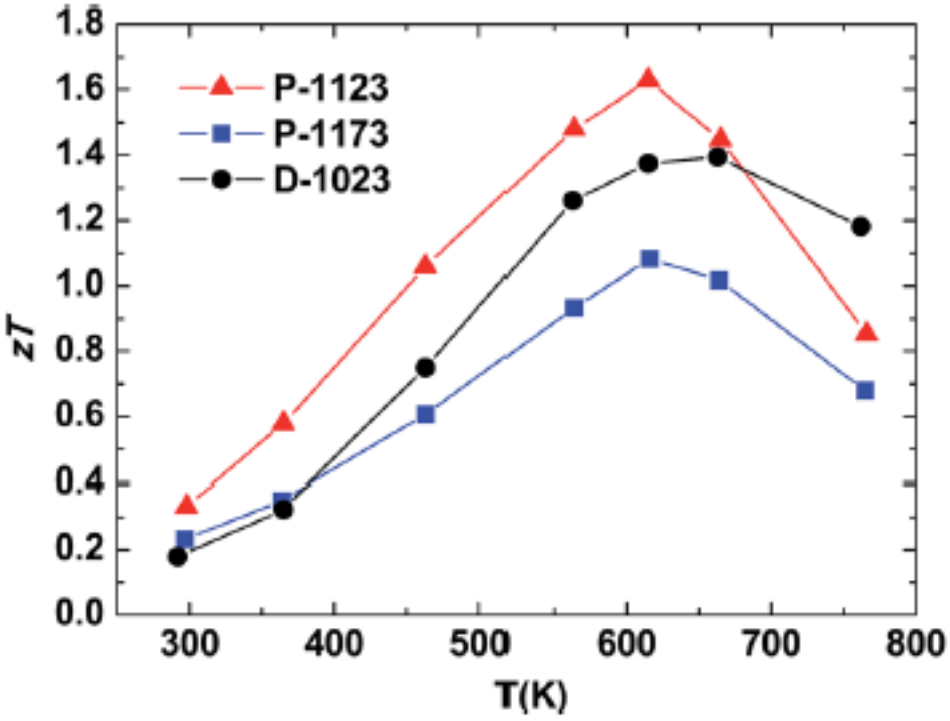

Figure 44. ZT plot for two pressureless sintered MgSiSnSb samples (P-1123 & P-1173) and the MgSiSnSb alloy used in this study (D-1023[5]).

The state of the art thermoelectric materials for mid temperature operation have been considered in this chapter. Skutterudites and half heusler materials provide modest ZT performances, but to reach higher thermoelectric performance, rare earth elements are used as dopants. Tellurides are the highest performing thermoelectric materials for the mid-high temperature region. A drawback to the use of telluride materials is primarily the cost and limited abundance of tellurium. Without a system for tellurium recovery, sources would be

rapidly exhausted should large-scale manufacture be carried out with this class of material. Furthermore, toxic materials such as Lead prohibit the use of Tellurides in many industries. Silicides offer a high performance, low toxicity and abundant supply of material for industrial energy harvesting thermoelectric materials. A limiting factor of this material is the reactivity of the n-type silicide semiconductor alloy which makes it difficult for incorporation into a thermoelectric module. Nonetheless, this material is chosen for study, with focus on joining characteristics for incorporation into a module.

3.6 Materials Summary

Table 4 outlines the findings from the literature study. Each material covered in the survey is evaluated based on working temperature, ZT, material stability, availability of raw materials and material toxicity. A scoring system is used to assess the suitability for use in a mid-temperature thermoelectric module: 3 points are awarded for a desirable quality/value, 2 points for a reasonable quality/value and 1 point for an undesirable quality/value. The final score is calculated by adding up the scores of each category for the individual material. The scoring is set so that a higher value represents the most desirable material.

Material	Peak Working Temperature (°C)	Peak ZT	Stability Under Operation (High/Medium/ Low)	Availability of Raw Materials (High/Medium/ Low)	Material Toxicity (High/Medium/ Low)	Score: Green=3pt Amber=2pt Red=1pt Score Sum
Bismuth Telluride	250°C -300°C	1.0 (473K)	High	Low	n-type – High	8
					p-type – Med	9
Skutterudite	600°C – 650°C	0.8 (700K)	Medium	Medium	Medium	10
Lead Telluride	500°C	1.6 (723K)	Medium	Low	High	10
Silicides	650°C	MgSi 1.6 (615K)	Medium	High	Low	14
		HMS 0.7 (800K)	High			13
Half Heusler	700°C	1.0 (600°C)	Low	Medium	Medium	10

Table 4. Summary table of material parameters reviewed from the literature. Final scores are calculated by adding up the individual scores of each category for the individual material. A higher score represents a more desirable material for a mid-temperature thermoelectric device.

The summary analysis shows that for development of mid-temperature thermoelectric modules silicides represent the most desirable material. It must be noted that the summary

table is designed for generic industrial applications, whereas alternative applications may favour particular material metrics. An example of this is in space applications where availability of raw materials and material toxicity is not as important as categories such as operating temperature, power density and long life performance [54]. Nevertheless, this table indicates the importance of developing modules using silicide materials.

3.7 Module Assembly and Silicide Joining

Due to the commercial sensitivity of module assembly processes, it is difficult to find literature regarding this particular field of study. Papers by Aoyama *et al*, Kim *et al* and Tarantik *et al* are identified as the most relevant papers which cover module assembly of silicide modules.

Komatsu Ltd is a thermoelectric module manufacturer based in Japan. The research division reports the development of a thermoelectric generating cascade module using silicides and bismuth telluride. Aluminium doped HMS and a tin doped magnesium silicide are used for the silicide component of the cascade device. Prior to the fabrication of the module, the effect of aluminium doping on the thermoelectric properties of the HMS is explored. Stoichiometric mixing of the manganese, silicon and aluminium is carried out followed by melting, grinding and final crystallisation using the Bridgman technique. Due to its structure, the HMS forms the metallic backbone (Nowotny chimney) in the c axis of the material shown in Figure 45. The effect of directionality on the electrical and thermoelectric properties is explored. It is found that at an aluminium doping level of 0.0035 gave a peak thermopower in the parallel direction to the c axis, with a Seebeck coefficient in the region of 200 μV/K. The n-type $Mg_2Si_{0.4}Sn_{0.6}$ is prepared by induction melting of stoichiometric amounts of material followed by ball milling and then SPS.

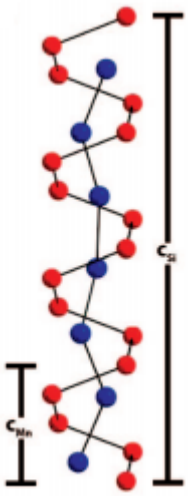

Figure 45. Nowotny chimney structure for higher managnese silicide. Labels show direction of c-axis [55].

Focussing on the silicide module assembly process outlined in the paper by Aoyama *et al*. Three joining processes were considered: brazing, thermal spray and mechanical contact. Brazing offers a high-performance joint but lifetime stability is questionable. Mechanical joining is considered to have a lower performance electrical contact but lifetime stability is improved. Thermal spraying is seen as a compromise between the two processes and was used to manufacture the prototype modules in the study. Two modules are produced using the thermal spray joining process; each consisted of 16 legs with dimensions of 4.5 x 4.5 x 6.75 mm^3 shown in Figure 46. The first module has pellets arranged with the c-axis in-plane to the thermal gradient and the second has pellets arranged with the c-axis perpendicular to the thermal gradient. The module assembly process uses ceramics with voids that act as a mask for the thermal spray process. Pellets are arranged under the ceramic and the thermal spray technique deposits aluminium into the voids. This process attaches the pellets to the ceramic and bridges between the pellets are made to provide the series circuit. Characterisation of the module is carried out and Figure 47 shows how the parallel pellets gave the best power density [42].

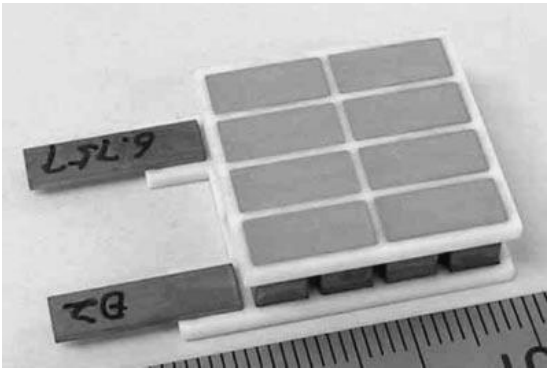

Figure 46. Silicide module with HMS and MgSi legs Typical pellet dimensions are 4.5 x 4.5 x 6.75 mm3[42].

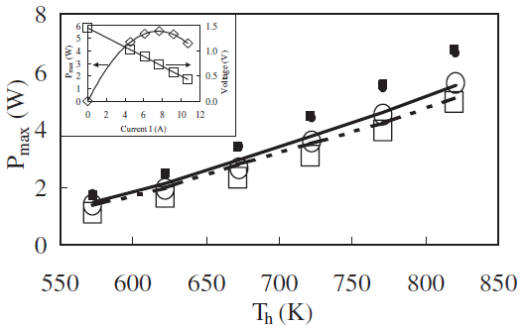

Figure 47. Max power from modules. Solid points are estimated values and open points are measured values. Circles represent the parallel module and squares represent the perpendicular module[42].

Contact and overall module resistances are not cited in the paper. A module efficiency of 6.4% is quoted, which is lower than the expected 7.5%. This is stated to arise from insufficient contact performance both electrically and thermally. Using the data from Figure 47 and the pellet dimensions stated in the paper, for a temperature differential of 300°C the power density of the module can be approximated at 617 mW/cm^2.

The next paper by Kim *et al* reports the successful joining of a 'π-shaped' generator consisting of segmented legs. The materials used are bismuth-doped magnesium silicide (MgSi), higher manganese silicide (HMS) and n and p-type bismuth telluride (BiTe).

The module consists of a single thermocouple segmented pair with each leg having a cross-sectional area of 4 mm x 4 mm. The n-type leg comprises 1 mm bismuth telluride and 5 mm magnesium silicide and the p-type leg comprises 2.6 mm bismuth telluride and 3.4 mm higher manganese silicide. Pellet geometries are calculated using computer simulated models.

Four joining mediums are tested in this study, two brazing alloys and two solders. The brazing alloys are intended for the hot side of the silicide pellets and the solders are tested for joining properties at the cooler interfaces of the module. The first brazing alloy contained silver, copper, tin and zinc (Ag-Cu-Sn-Zn) and the second was silver and cadmium (Ag-Cd) with processing conditions of 680°C – 5 min and 425°C – 3 min respectively.

A barrier coating is deposited by electron-beam evaporation onto the contacts of the silicide material. An adhesion layer of 50 nm titanium is deposited followed by 1 μm thick layer of silver as the barrier layer to improve wetting and adhesion of the brazed junction.

Brazing tests were carried out under a flowing atmosphere of 95% Argon and 5% Hydrogen at a flow rate of 2 l/minute. The contact resistance measured between the copper contact and the n-type and p-type silicide material using the Ag-Cu-Sn-Zn braze alloy is 4.8 μΩcm^2 and

3.2 μΩcm^2, respectively. Lower performance results are achieved with the Ag-Cd alloy that is characterised at 14.07 mΩcm^2.

Thermoelectric performance data is taken for a segmented module made using the Ag-Cu-Sn-Zn braze for the silicide-copper joint and a Pb-Ag-Sn-In solder for the silicide-telluride and telluride-copper joints. Figure 48 shows the power data at various temperature differentials for the segmented module.

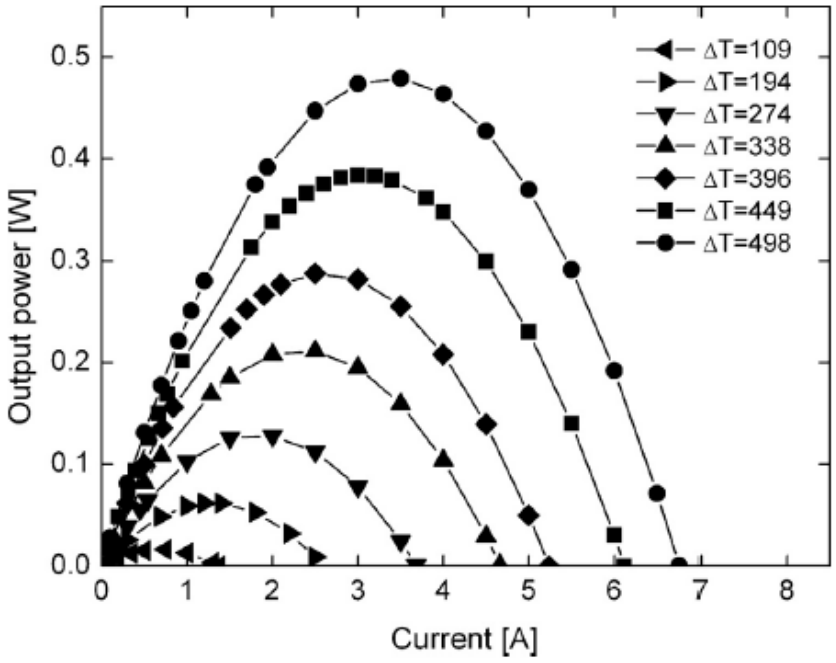

Figure 48. Thermoelectric performance of a segmented π-shaped thermoelectric generator at various temperature differentials[46].

The maximum output power achieved at a temperature differential of 498^{o}C is 480 mW. At a temperature differential of 338^{o}C, the peak power is measured at approximately 200 mW, which translates to a power density of ~625 mW/cm^2.

The final paper related to Silicide joining is by Tarantik *et al* from the Fraunhofer Institute in Germany. Ten joining processes were screened and four prototype modules were assembled using magnesium silicide and higher manganese silicide semiconductor materials for characterisation.

N-type magnesium tin silicide with the stoichiometric ratio of 2:0.4:0.6 and p-type un-doped higher manganese silicide was used to produce several joining trials, summarised in Table 5. ZT measurements show that the material has a poor thermoelectric performance with the n-type peaking at 0.3 and p-type at 0.05. It is stated that although the performance of the materials is low, it is not crucial for exploring assembly processes. In some respects, this

statement is valid but is known that in general un-doped materials are significantly less reactive in comparison doped samples. When attempting to apply the process to a doped sample, it may not be suitable as the material characteristics may have changed significantly.

The semiconductor material was protected with a barrier layer of 1 μm sputter coated nickel and is contacted to various suitable substrates, outlined in Table 5. The ten unicouple trials yield unsatisfactory results. Test UC_06 (see Table 5) is repeated under 550°C for 120 minutes with a Nickel based braze alloy and produces a successful result. Subsequently, a number of modules are assembled for characterisation, ranging from 2-couple modules to a 31-couple module. Figure 49 shows and example of the 31-couple device.

At a temperature differential of 531°C, the peak power output of two 2-couple devices with pellet dimensions of 5 mm x 5 mm x 3 mm (l, w, h) are recorded at 99 mW and 110 mW. This represents a power density of ~100 mW/cm^2 [5].

Unicouple (UC) #	Contact material	Brazing material	Processing condition	Comment
UC_01	Ni	Ag-Cu-Zn	770 °C – 10 min	HMS leg cracked
UC_02	Ni	Ag-Cu-Zn	730 °C – 20 min	HMS leg cracked
UC_03	Ni	Ag-Cu-Zn-Sn	730°C – 20 min	HMS leg cracked
UC_04	Ni	Ag-Cu-Zn-Sn	730°C – 20 min	mechanically stable, but REM/EDX analysis detects reaction of TE material with braze
UC_05	Cu on Al_2O_3	Sn	400°C – 120 min	no stable joint
UC_06	Ni/Cu on Al_2O_3	Ni (main component)	280 °C – 120 min	no stable joint
UC_07	Cu on Al_2O_3	Cu (main component)	500 °C – 120 min	stable after brazing; cracks after mechanical treatment
UC_08	Ni/Cu on Al_2O_3	Sn-Te	900 °C – 10 sec	mechanically stable, but very high R_i > 50 Ω
UC_09	Ni/Cu on Al_2O_3	Al	615°C – 15 min	no stable joint
UC_10	Ni/Cu on Al_2O_3	Al	700°C – 5 sec	mechanical stable, but very high R_i > 0.9 Ω

Table 5. Summary of brazing tests carried out on silicide couples by Fraunhofer IPM [5].

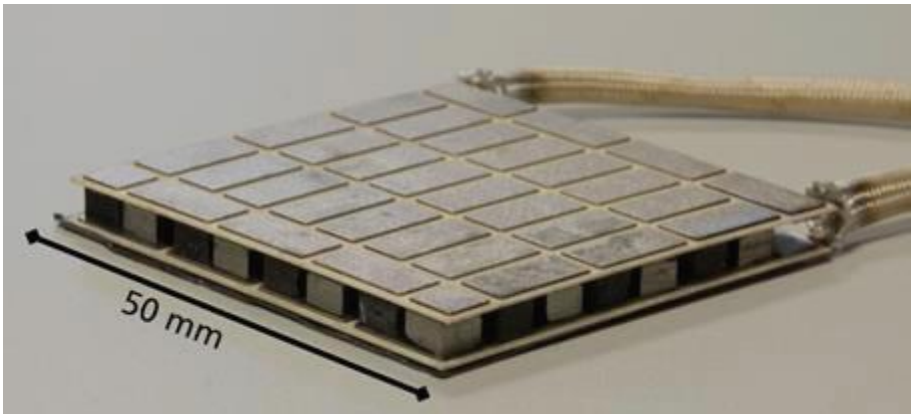

Figure 49. Silicide module produced by Fraunhofer IPM containing 31 couples of magnesium silicide and higher manganese silicide[56].

The relevant literature has been reviewed for silicide module assembly and joining. Three separate joining techniques have been tested with varying success. Power densities of modules in the range of 100 to 625 mW/cm^2 have been presented using different varieties of n-type and p-type Silicide material. Power densities of prototypes produced in this study will be compared to the state of the art data which has been reviewed.

4. Thermoelectric Joining and Module Fabrication

In this section, results are presented and discussed for the development of a high-performance silicide based thermoelectric generator. A study of pre-contacted material supplied by Toyota is initially carried out and the results are attempted to be replicated using high-performance material supplied by IntrinsiQ materials, London, and Queen Mary, University of London.

Two sources of semiconductor are used in this study. The first is produced by the combined groups of IntrinsiQ materials and Queen Mary University of London (QMUL). The powders of magnesium silicide and higher manganese silicide are produced by IntrinsiQ materials via the plasma-torch technique. The plasma-torch method produces nanoparticles of the desired alloy to a specifically controlled diameter. The nanopowders are then consolidated into densely formed pucks via spark plasma sintering; carried out by QMUL. The resulting pucks are very close to the theoretical maximum density (98%) and are comprised of nanoscale grains that improve the thermoelectric properties with respect to reduced thermal conductivity. The n-type material is doped with tin and the highest performance dopant level is found with a stoichiometric formula of $Mg_2Si_{0.4}Sn_{0.6}$ and the p-type has the composition of $MnSi_{1.7}$. The pucks were received in a raw state and so it was necessary to process the materials into pellets before joining trials were carried out. Section 2.1 outlines the process that was used for pelletization of the materials. The magnesium silicide is particularly high performance, with a peak ZT of >1.1 achieved by tin doping [26, 45]. The lower performance p-type higher manganese silicide has a peak ZT of approximately 0.7 [42] and offers a suitable semiconductor to produce the thermocouple arrangement necessary to assemble a thermoelectric module.

The second group of silicides were produced and manufactured by Toyota-Tsusho and Yasunaga in Japan. There are a few differences between the materials in comparison to the samples produced by QMUL and IntrinsiQ in that the dopants are different and a barrier coating is in place to improve the joining process. The higher manganese silicide remains undoped but the Magnesium silicide is doped with antimony at 1.5% with formula $Mg_2SiSb_{1.5}$at%. The samples are received in processed form, diced into pellets using a multi-wire diamond saw with dimensions 2.5 mm x 2.5 mm x 3 mm (l, w, h respectively).

The purpose of using this material is for developing a joining process with a material that already has a good barrier layer in place. From this study, know-how can be replicated for the IntrinsiQ/QMUL material.

4.1 Filler metals and Processing Conditions

The primary brazing alloy used in this study is a silver-based product. Johnson Matthey Silver-flo 56 is supplied in paste form that consists of the powdered alloy suspended in a liquid flux. The composition of the alloy is Ag56 Cu22 Zn17 Sn5 and has a melting range of 618^{o}C to 652^{o}C.

This is the lowest melting temperature silver brazing alloy that is readily available. Lower temperature brazing alloys do exist, but in the 450^{o}C to 600^{o}C melting temperature bracket, the alloys primarily consist of aluminium and silicon. These alloys are notoriously difficult to use and their properties once brazed are more suited for mechanical purposes and less so for electrical connections.

Above the silver alloy melting bracket, alloys tend to consist of gold and approaching 1000^{o}C, nickel becomes more common. In this bracket of alloys, the flow temperature is higher than the semiconductor material can withstand and the pastes become more expensive. Although the melting temperature of the silicon semiconductor materials is closer to 1000^{o}C, it is the sintering temperature that must be considered as exceeding this temperature will cause physical changes in the material, grain growth and a reduction in density is likely to occur.

4.1.1 Preliminary Tests

A variety of joining mediums were tested in preliminary studies. Initial tests are carried out prior to joining with the addition of a barrier layer on the QMUL/IML silicide material. The materials are tested without barrier coatings for high throughput of joining trials, as the processes for deposition are lengthy. Furthermore, baseline results can be obtained for comparison with later results to quantify the effect of including a barrier layer.

This section summarises results with four commercially available joining materials. The vacuum brazing assembly described in Section 2.2 is used for trials along with the wire jig for pellet positioning described in Section 2.3. At the preliminary stage, specific characterization is not available. As a result, several couples are assembled for each joining trial for resistance measurement using a handheld AC resistance meter. This is done because the minimum resistance measurement for the handheld device is 5 mΩ. If an ideal junction is achieved, the resistance would be below the measurement range of the equipment. At this stage, the mechanical strength of the joint is given more importance.

The most successful joining material will be used to assemble a 49 couple device for maximum power point characterisation on the module test rig described in Section 2.5.3.

4.1.1.1 Silver Brazing Rod

Initial tests were carried out using silver brazing rod, Castolin XFC. The rod is flattened using a cold press and small squares of the alloy are formed out of the flattened rod using a square headed punch. Superflux 1802 flux paste is used to improve the flow of the alloy during brazing and adds stability to the assembly when positioning pellets. The melting temperature of the brazing alloy is 625^{o}C and so a range of temperatures above this are tested for rapid heating and cooling.

Samples joined using this process exhibited poor mechanical strength due to the formation of brittle intermetallic phases. Achieving a mechanically strong junction is important as the thermoelectric material represents a structural part of a module. At a brazing temperature of 700^{o}C for 10 minutes under a vacuum pressure of 5x10^{-2} Torr, a junction could be fabricated which was sufficiently strong enough for electrical characterisation. Resistances were measured using a handheld AC resistance meter. The resistance across an MgSi pellet attached to two nickel conductors would vary between 0.2 – 2 Ohms for multiple samples, indicating that repeatability of this experiment is very low. Furthermore, difficulty in controlling volume of alloy and the subsequent difficulty in assembly made using brazing rod unfeasible. Figure 50 shows a cross sectional stereoscope image of one of the samples brazed at 700^{o}C for 10 minutes under a vacuum pressure of 5x10^{-2} Torr. Severe diffusion of elements has occurred which explains the reduced mechanical and electrical properties. A crack has propagated above the bond, emanating from the edge of the pellet where the diffusion has leached along the edge of the pellet.

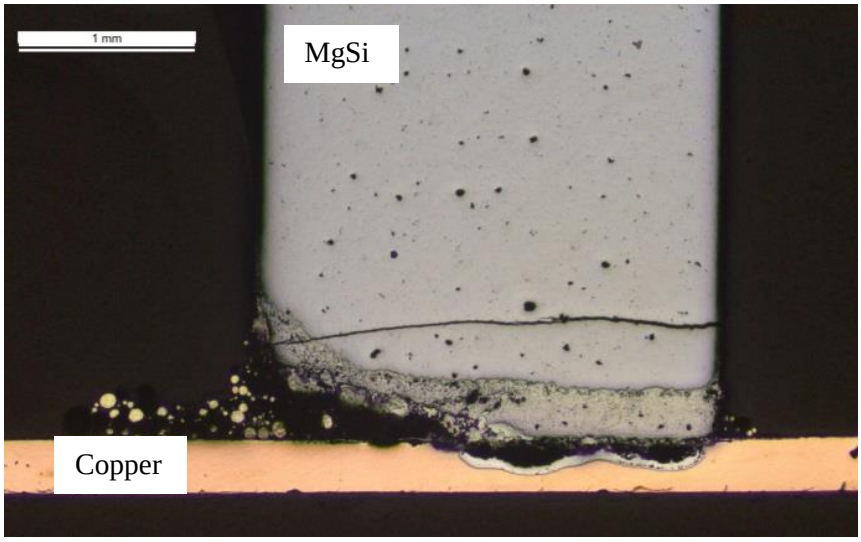

Figure 50. Stereoscope image of a MgSnSbSi pellet brazed at 700C for 10 minutes at a vacuum pressure of 5E-2 Torr, using Castolin XFC brazing rod and Superflux 1802.

4.1.1.2 Silver Brazing Ribbon

Ribbon of silver brazing alloy is identified as a replacement to the brazing alloy rod. This addresses the issue of the uneven brazing alloy pieces causing difficulty in assembly. Braze alloy tabs of a uniform height are cut using scissors without the need for pressing and punching. The ribbon alloy is the same composition as the brazing rod supplied by Castolin. An identical brazing profile to the brazing rod is used for comparison. Tests showed that the ribbon alloys join the thermoelectric material with similar properties to the brazing rod, with thermocouple resistances ranging from 0.2 – 2 Ohms, measured using a handheld AC resistance meter.

A reoccurring problem with using the solid alloys was that the bond line was particularly large in most cases, although the variability in bond line thickness was reduced by the use of a more controlled thickness. Furthermore, alignment of the pellets was still an issue as during assembly, in essence, the process involved balancing the components on top of each other with flux adding a small amount of stability. To address the issue of assembly difficulty, brazing pastes are tested as they provide more control over alloy volume applied and the adhesive properties of the liquid flux suspension gives stability to the pellets during positioning.

4.1.1.3 Silver Brazing Paste

Silver brazing pastes consist of a microparticulate suspension of brazing alloy in a high-temperature flux. This offers a simpler method for assembly of the thermo-elements and better control over volumes of alloy used. The two pastes tested in this section can only be acquired in sample form as they are not commercially available.

Two silver based brazing pastes samples are tested: Fusion STL-126 braze paste with 56% silver content and Castolin XFC braze paste with 57% silver content. Both had the same solidus temperature of 620^{o}C and liquidus in excess of 650^{o}C. Identical brazing processing conditions are carried out as the solid alloy tests at 700^{o}C for 10 minutes under a vacuum pressure of 5x10^{-2} Torr. Resistances are measured using a handheld AC resistance meter. Junction resistances of 0.1-0.2 Ohms were achieved in some cases but repeatable results were not attainable. Figure 51 shows an SEM image of the broken braze interface; it was observed that in most cases flux was still present in the joint and large voids were observed. The voids may have arisen due to flux evaporating out of the joint, leaving a hole, or the alloy not fully melting and so spaces are left between the particles. The bond line, ease of assembly, and therefore, alignment of the pellets was significantly improved using a silver based brazing paste. It is expected that ideal contact resistances were not achieved as severe diffusion reactions occurred. This study shows the importance of a barrier layer for protection of the semiconductor material.

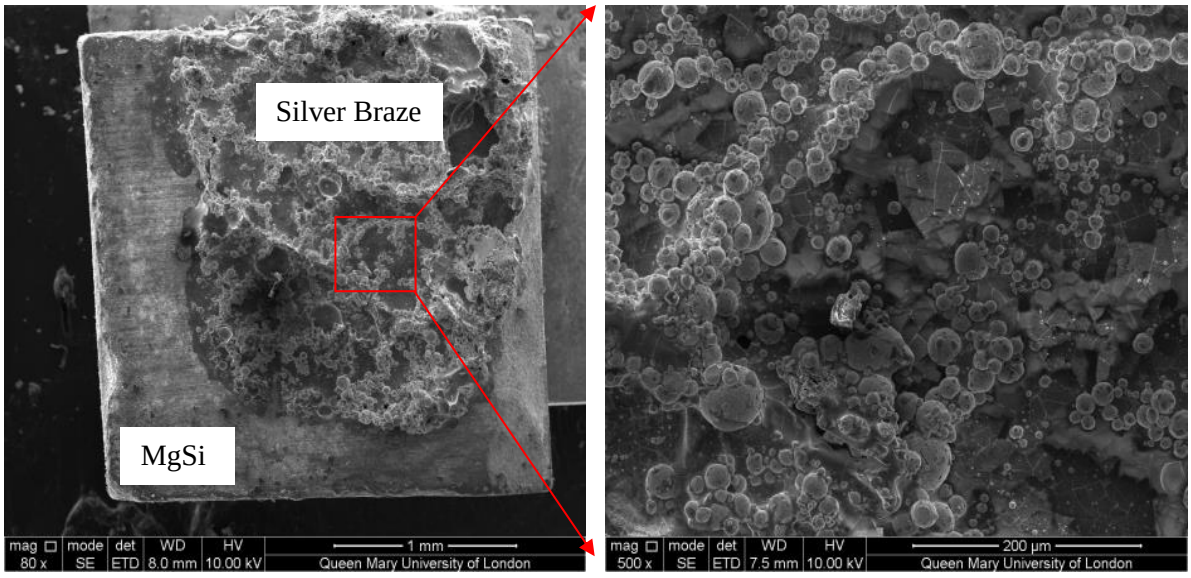

Figure 51. SEM image of MgSiSnSb pellet with brazed Castolin XFC paste. Sample shows poor flowing of the alloy in the junction that caused removal of the pellet from nickel metallic strap.

4.1.1.4 Silver Loaded Screen Printing Paste

Due to the difficulty of finding brazing pastes that have suitable commercial availability and joining properties for the silicide material; thick film screen printing pastes were identified as an alternative. Screen printing pastes comprise of a mixture of silver particles and a glass/ceramic matrix called Frit. A high silver screen printing paste is identified which has a recommended curing range of 580-680^{o}C for between 40-60 minutes. Q-Inks AG2300 is expected to offer a less aggressive approach to joining the samples as a flux is not present in the paste.

To protect the magnesium silicide material, a curing regime is used at the lowest temperature of 580^{o}C for 60 minutes under a vacuum pressure of 5x10^{-2} Torr. Single cured elements have an average resistance of 0.05 Ω over five samples, measured using a handheld AC resistance meter. The junctions are mechanically joined but the contact resistance is still extremely high.

Nonetheless, silver loaded screen printing paste represents the most successful approach for joining magnesium silicide without the presence of a barrier layer. For comparison with future tests, a 49 couple device is assembled, shown in Figure 52, using the screen printing paste and is characterised using the test rig described in section 3.4.

The optimal curing temperature was at 580^{o}C for 60 minutes under a vacuum pressure of 5x10^{-2} Torr.

Using an Agilent U1732B LCR set to 120 Hz, a total module resistance of 2.8 Ω is measured. The measurement is taken including wires that are soldered using a 60/40 Tin/Lead solder.

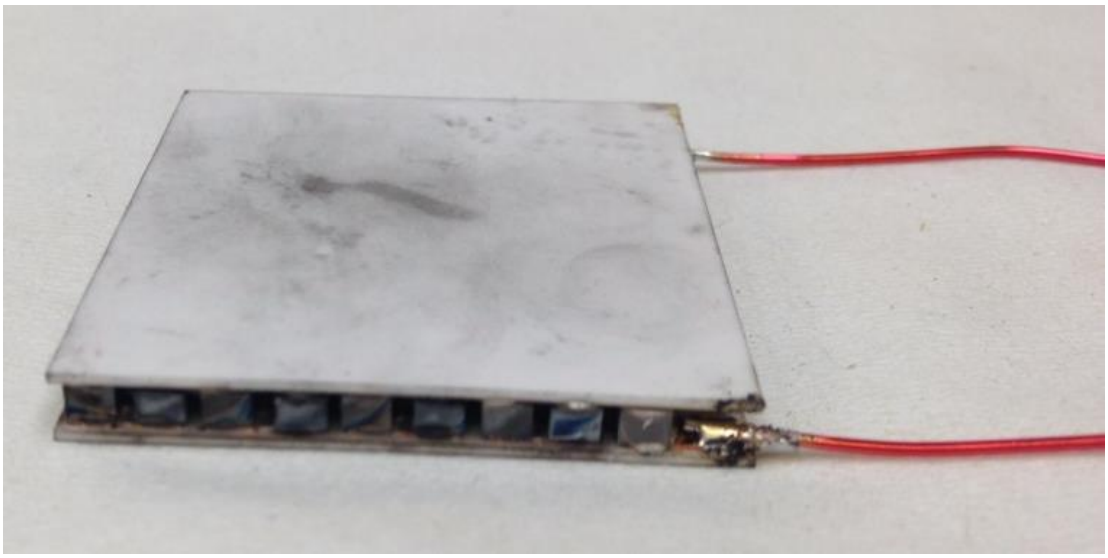

Figure 52. A 49-couple module fabricated using Magnesium Silicide and Higher Manganese Silicide and Silver loaded conductive ink.

The devices power output is measured using bespoke testing equipment described in section 3.4. The module is clamped between two plates and a temperature gradient imposed on the device. The cold side is maintained at 23°C and measurements taken when the hot side reaches 323°C; this gives a 300°C temperature drop. The voltage and current characteristics of the module are measured at increasing loads. Figure 53 shows the power graph at different loads on the module at a 300°C temperature drop.

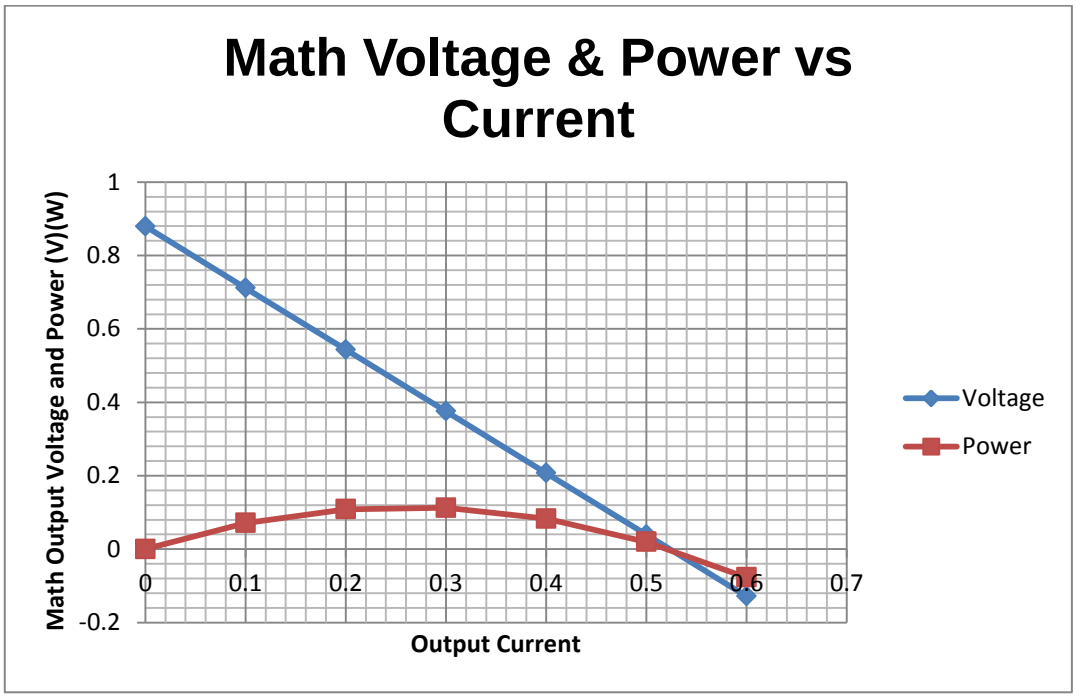

Figure 53. Power and IV curve for a 49-couple silicide module under a temperature gradient of 300oC.

The open circuit voltage is measured at 872 mV with a maximum power output of 112 mW occurring at a voltage of 364 mV and current of 306 mA at matched load.

The module is then taken to a delta T of 500°C with the hot side at 525°C and cold side at 25°C. The open circuit voltage is measured at 1.9 V with a maximum power output of 581 mW occurring at a voltage of 960 mV and current of 605 mA at matched load.

4.1.2 Preliminary Test Summary

The preliminary tests show that a metallic barrier layer is essential for joining magnesium silicide. Silver based screen printing ink is shown to produce mechanically strong joints but the high resistance incurred indicates that this process is not suitable for industrial scale manufacture of modules. From the literature review, brazing alloys are used in conjunction

with barrier layers on the silicide material. For this reason, further joining trials were carried out with a silver-based braze paste. After contacting a number of brazing alloy manufacturers, a commercially available braze paste was identified. Johnson Matthey Silverflow-56 was supplied for further study in joining the silicide material. The alloy contains silver, tin, zinc and copper and has a melting temperature of 630^{o}C and a recommended brazing temperature of 700^{o}C.

4.2 Toyota and Yasunaga Material Study

Magnesium silicide and higher manganese silicide pellets were received pre-cut and pre-contacted for joining trials. Johnson Matthey Silver-flow 56 was used as a brazing medium for the joining of the pellets to nickel straps for contact resistance measurements (described in section 1.2.1). Initially, the layer thicknesses at the interface were analysed and compared to joined cross sections to determine the effect the brazing process on the layers. A joining process was then developed which is suitable for brazing of the high-performance QMUL/IML silicide material.

4.2.1 Toyota MgSi Pellet Cross Section

The layer thickness results shown in Table 6, corresponding to Figure 54, indicate that co-sintering has been carried out on the sample. This is identified due to the layer thickness that is in the order of 10's of microns and the diffusion layer between the nickel and magnesium silicide layer. It would not be possible to achieve these thicknesses or phases by plating or sputter coating. The regions closest to the semiconductor material consist of a 7 μm thick silicon/nickel intermetallic phase. Three layers are present within this intermetallic region, each separated by varying nickel/silicon ratios. The top nickel layer is approximately 18μm thick and contains negligible amounts of silicon.

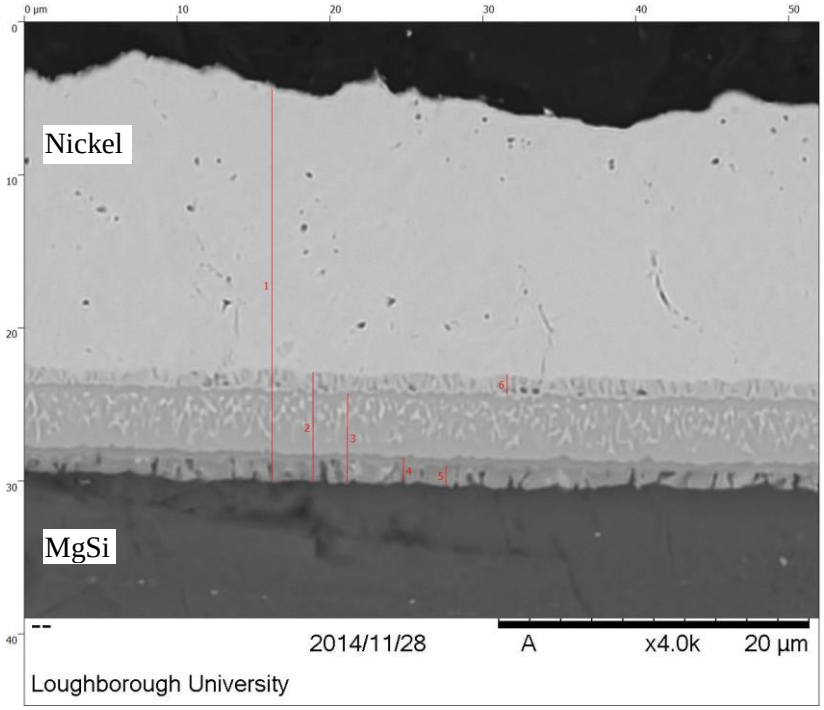

Figure 54. SEM image of the metallised surface of a magnesium silicide pellet produced by Toyota. Figure 53 displays the corresponding measurement data from this image.

Line Number	R [µm]	Layer Composition
1	25.62	Junction
2	7.18	Reducing amount of Si and increasing amount of Ni across interface layer
3	5.87	Reducing amount of Si and increasing amount of Ni across interface layer
4	1.66	Nickel and silicon are main constituents. As Nickel silicide has formula Ni2Si in most cases and Silicon is the main element in this layer, indicates that there is little Ni2Si and is more of a solid solution of the two elements.*
5	1.24	
6	1.31	Majority Nickel, small trace of Silicon.
Layer 3 – layer4	~4	Even split between Nickel and Silicon. *

Table 6. Measurement and estimated compositional data for the metallised surface layers of a magnesium silicide pellet produced by Toyota, corresponding to figure 52.

4.2.2 Toyota Magnesium Silicide Brazed Junction

The first test on the Toyota magnesium silicide was carried out at 700°C for 10 minutes under 0.25 Bar argon inlet pressure in the small prototyping jig described in section 2.2. The brazing duration of 10 minutes was timed from initial insertion of the assembly into the tube furnace, which is preheated at 700°C, to removal for cooling at ambient temperature surroundings. SEM cross-sectional analysis, compositional line scanning EDS and four probe contact resistance is used to characterise the sample.

Figure 55 shows a cross-sectional SEM image of the interface between the magnesium silicide and nickel contact. The joint is mechanically strong and no diffusion can be observed in the interface due to brazing. The bond line is measured at approximately 80µm thick as shown in Table 7.

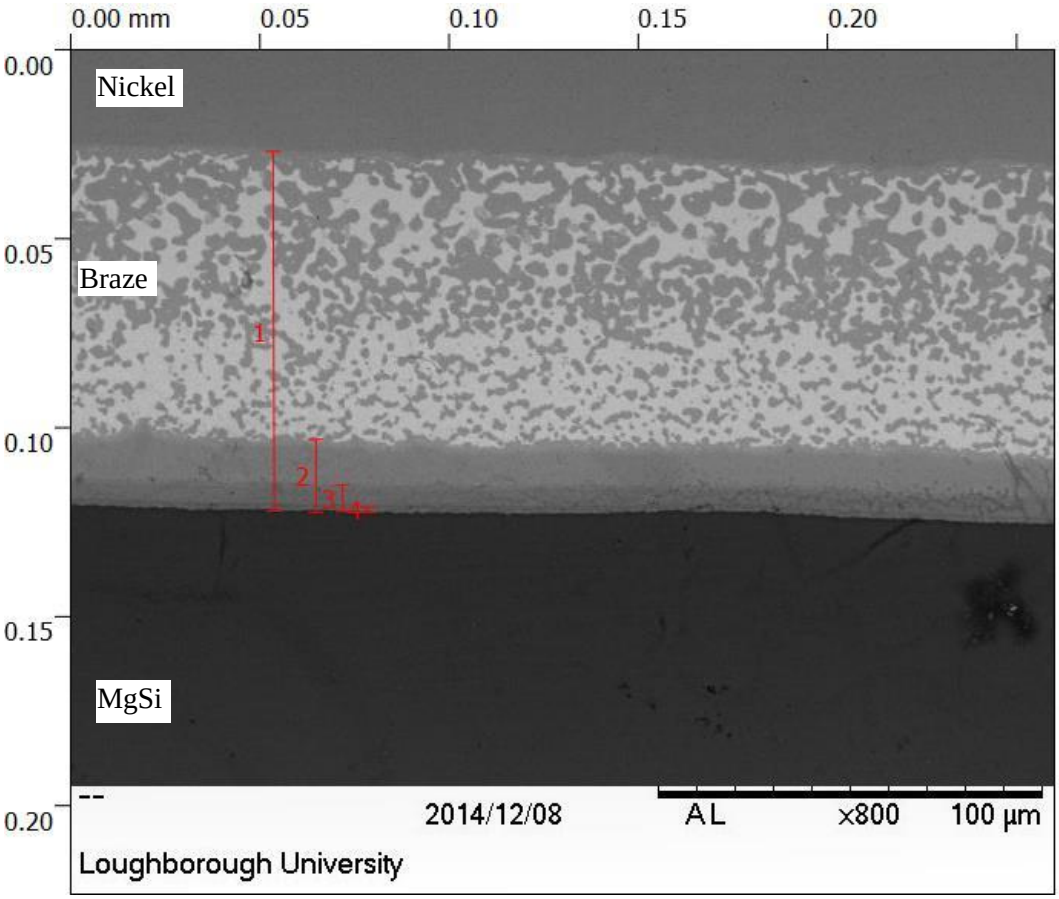

Figure 55. SEM image of the brazed interface of a nickel strap to a magnesium silicide pellet produced by Toyota, using Silver flo-56. Figure 55 displays the corresponding measurement data from this image.

Line Number	R [µm]
1	95.3
2	19.3
3	6.9
4	1.4

Table 7. Measurement data for the brazed interface of a nickel strap to a magnesium silicide pellet produced by Toyota, using Silver flo-56, corresponding to figure 54.

The EDS spectrograph in Figure 57 for the line scan in Figure 56 shows that the barrier layer is unchanged due to the nickel peak and gradual drop of Silicon around the 50 um mark. Comparing the Silicon graph to the un-brazed sample, there is a likeness with respect to the shoulder that occurs midway through the barrier layer.

The thicker layer above the barrier coating comprises expected elements for the silverflow-56 braze alloy. The low readings of magnesium, silicon and nickel indicate that the barrier layer is successful in preventing elemental diffusion.

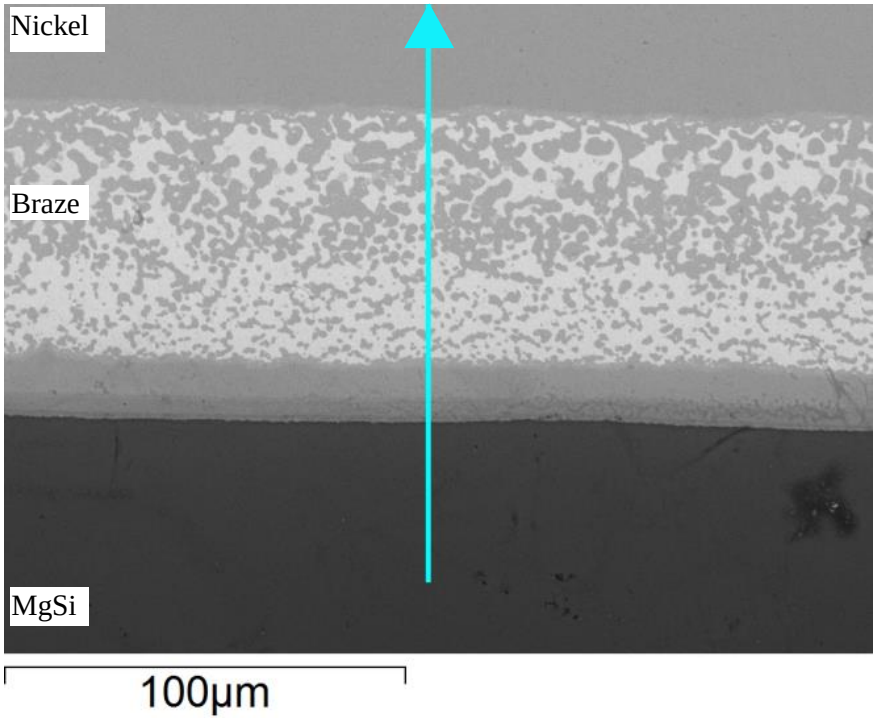

Figure 56. SEM image of the brazed interface of a nickel strap to a magnesium silicide pellet produced by Toyota, using Silver flo-56. The cyan line represents the area of data taken for XPS line scanning for compositional analysis, shown in figure 57.

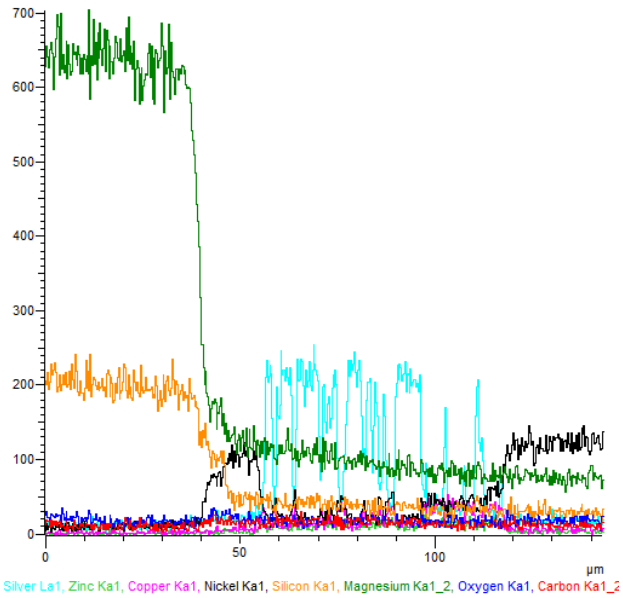

Figure 57. XPS line scan data for the compositional dependency along an intersection of the brazed interface of a nickel strap to a magnesium silicide pellet produced by Toyota, using Silver flo-56.

XPS analysis shows little to no measurable diffusion of components from the semiconductor to the braze joint and vice versa. The slightly higher reading of magnesium in the joint may arise from some diffusion which is possible but can also arise from the sample preparation process causing magnesium particles to be embedded on the surface of the sample and background readings from the electron detector.

The specimen was joined strongly enough for characterisation tests and the junction cross section shows no signs of diffusion occurring. To complete the analysis, contact resistance must be defined for the sample as this is a major factor in junction quality. Figure 58 shows the linear dependence of resistance across the sample, from which the contact resistivity is calculated. The results for all tests in this study are tabulated and are displayed in Figure 58.

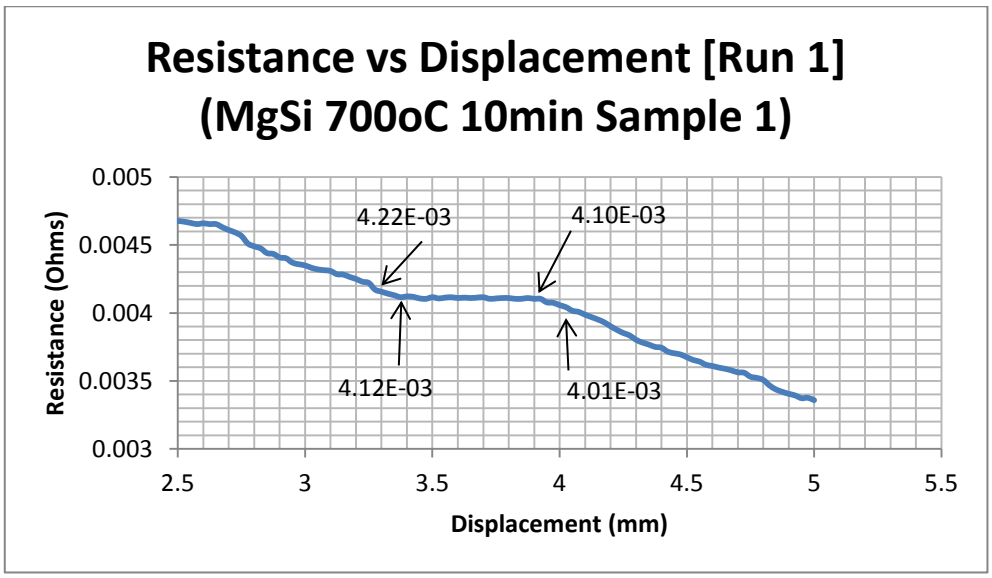

Figure 58. Graph showing resistance dependence of a joined sample to displacement from the starting point of measurement.

Material	Time (s)	Sample	Run	Average Resistivity (Ohm.cm)	Sample Average Resistivity
MgSi	10	1	1	4.27E-04	4.47E-04
		1	2	4.01E-04	
		1	3	5.13E-04	
		2	1	5.95E-03	5.95E-03
	12.5	3	1	3.95E-04	4.17E-04
			2	4.31E-04	
			3	3.37E-04	
			4	4.44E-04	
			5	4.80E-04	
HMS	10	1	1	2.49E-03	3.30E-03
			2	3.04E-03	
			3	4.37E-03	
	12.5	1	1	2.36E-03	2.13E-03
			2	1.66E-03	
			3	2.37E-03	

Table 8. Contact resistivity values for different samples with various brazing durations.

The first row of results in Table 8 show that, for the magnesium silicide sample, the average junction resistivity ranged between 0.45 μΩ.m and 5.95 μΩ.m. This is an acceptable range when comparing to the bulk resistivity, but the variation in results indicates that the onset of reactions may be occurring in other parts of the interface, this is postulated as the SEM data only represents a small sample of the whole junction. To explore this, the relationship between brazing time and junction resistivity is measured. A brazing temperature of 700°C for 12.5 minutes is tested and data is collected on the junctions produced.

The SEM imaging and EDS line scan data in Figure 59 Figure 61 show that a reaction has occurred during the brazing process in which silver and magnesium has cross diffused due to

a breakdown in the barrier layer. The contact resistivity result in Table 8 does not reflect this damage as an average resistivity of 0.42 μΩ.cm is measured. This suggests that in other parts of the interface, the barrier layer may not have broken down due to variations in temperature across the sample. It is likely that operation lifetime of a module with this brazing process would degrade significantly during its operational lifetime due to the defects in the joining interface. For this reason, it can be concluded that lower temperatures or brazing times are necessary.

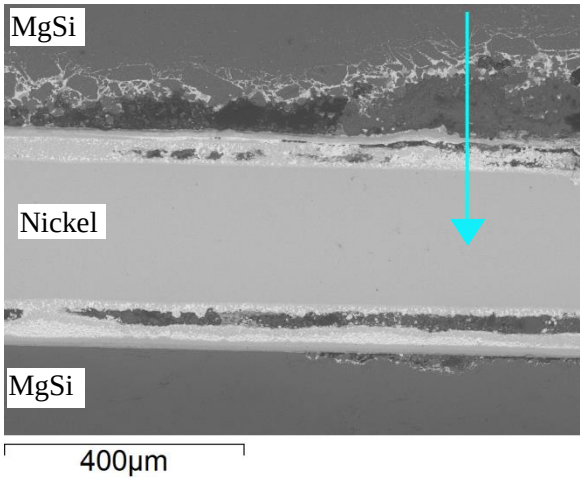

Figure 59. SEM image of junction interface after brazing for 12.5 minutes at 700oC. The cyan line shows the sample area taken for EDS line scanning.

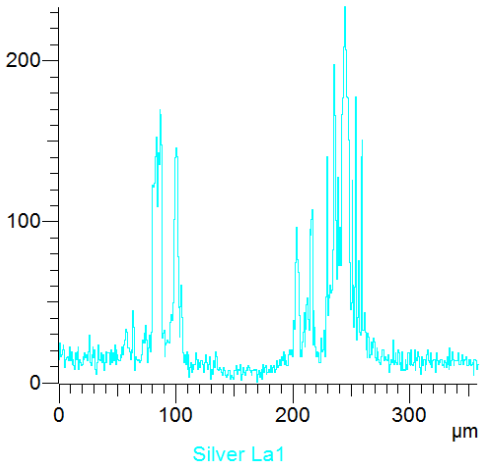

Figure 60. EDS line scan data for silver across the braze interface.

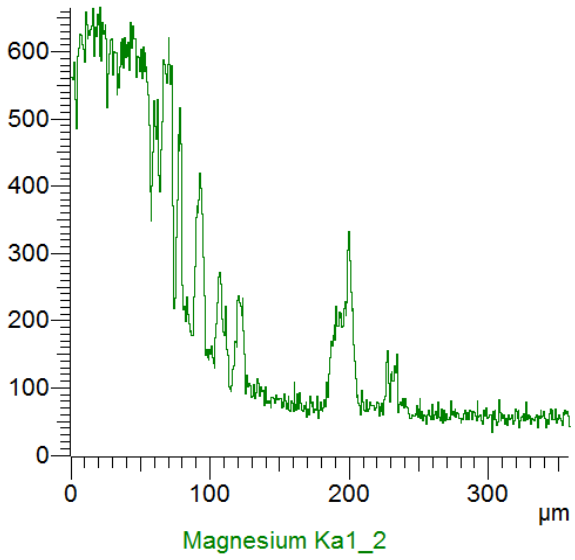

Figure 61. EDS line scan data for magnesium across the braze interface.

The recommended brazing temperature for the Silver-flow 56 is 700^{o}C but the alloy melting temperature is between 630^{o}C and 680^{o}C. As the aim is to develop a joining process that can be replicated for the IML/QMUL material, brazing temperatures must be significantly lower than the sintering temperature of the magnesium silicide. The sintering temperatures are unknown for the Toyota material but we know that the IML/QMUL material is sintered at 750^{o}C. A safety margin of a minimum of 100^{o}C is necessary for limiting damage to the material and so temperatures at or below 650^{o}C are tested.

Unicouple samples are joined under argon flow at 630^{o}C and 650^{o}C for 10 minutes braze time with a gas pressure of 0.25 Bar. Appendix item 3 (**A3**) details the contact resistance values for various samples. At 650oC for 10 minutes, the average contact resistance per area is measured at 8.58 ± 0.61 μΩ.m^{2} and at 630oC for 10 minutes, the average contact resistance per unit area is measured at 5.13 ± 0.55 μΩ.m^{2}. The variation of resistivity between the two samples is significantly lower than the samples brazed at 700^{o}C and the resistivity value for the 630^{o}C brazed sample is of an acceptable order in comparison to the bulk material resistivity value. When comparing the resistance of the junction to the bulk resistance of the magnesium silicide, the 630^{o}C brazed sample is approximately 20% of the bulk resistance. By reducing this ratio of resistances, resistive losses in a module will be decreased thus increasing efficiency and power output.

4.2.3 Toyota Higher Manganese Silicide Brazed Junction

As a thermoelectric module contains both ‘n’ and ‘p’ type semiconductors, the joining process has to satisfy conditions for both corresponding materials. Identical processing conditions for the p-type higher manganese silicide as the n-type magnesium silicide have been tested and the samples are characterised.

Figure 62 shows the HMS metallization layer. It is unclear as to how this layer was deposited but it is expected that co-sintering has been used owing to the thin, discoloured layer at the interface between the nickel and HMS (circled in red). This thin layer is typical of an interface between two diffusion bonded materials. Reliable XPS data could not be obtained on this sample as the layer was not well defined well enough to collect accurate compositional data.

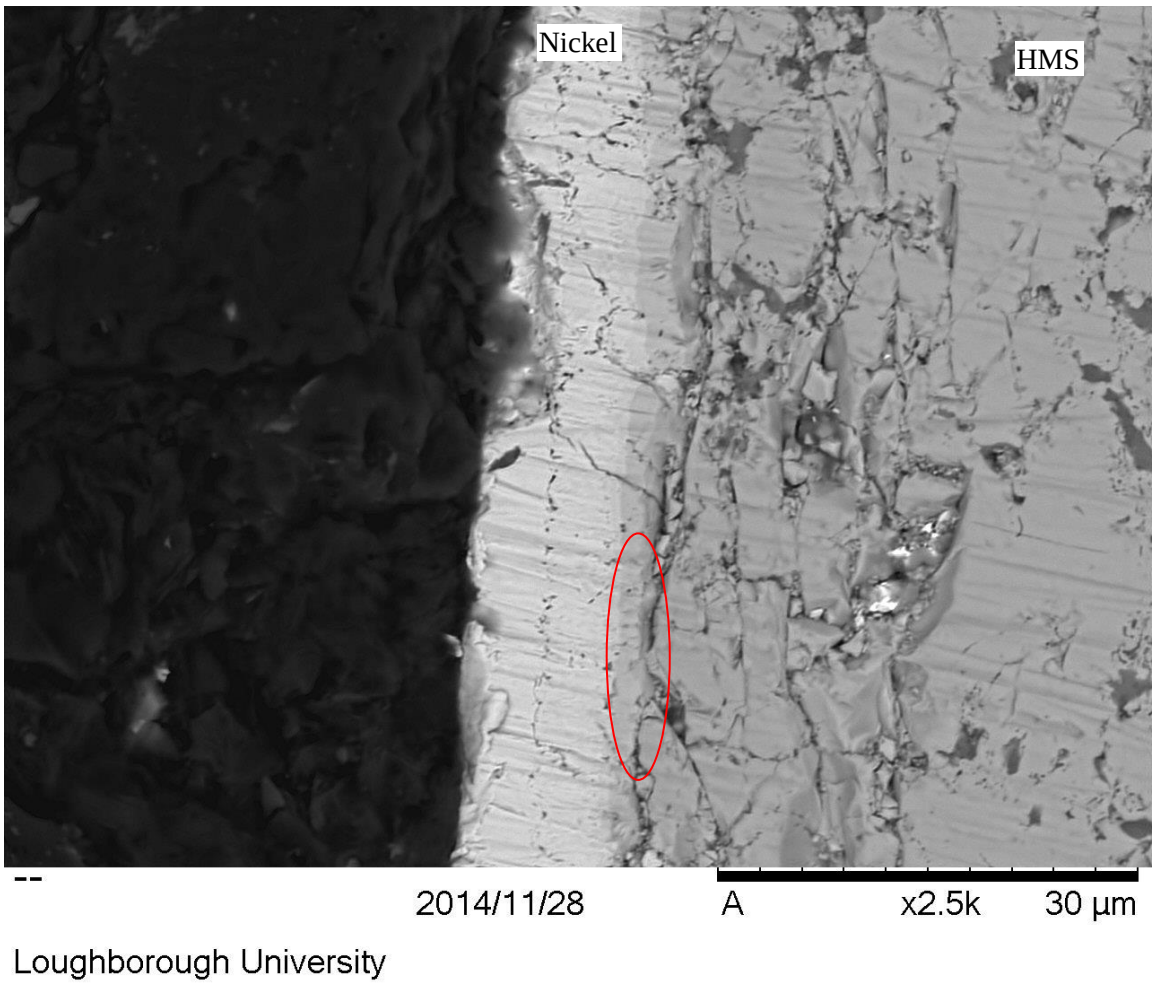

Figure 62. SEM image of metallised Toyota HMS, showing less distinct layers in the barrier layer.

The HMS sample was joined to a nickel contact using silver flo-56 at 700^{o}C with a brazing time of 10 minutes. Cross sectional SEM analysis in Figure 63 shows that the diffusion barrier has broken down and allowed silver to diffuse into the semiconductor material.

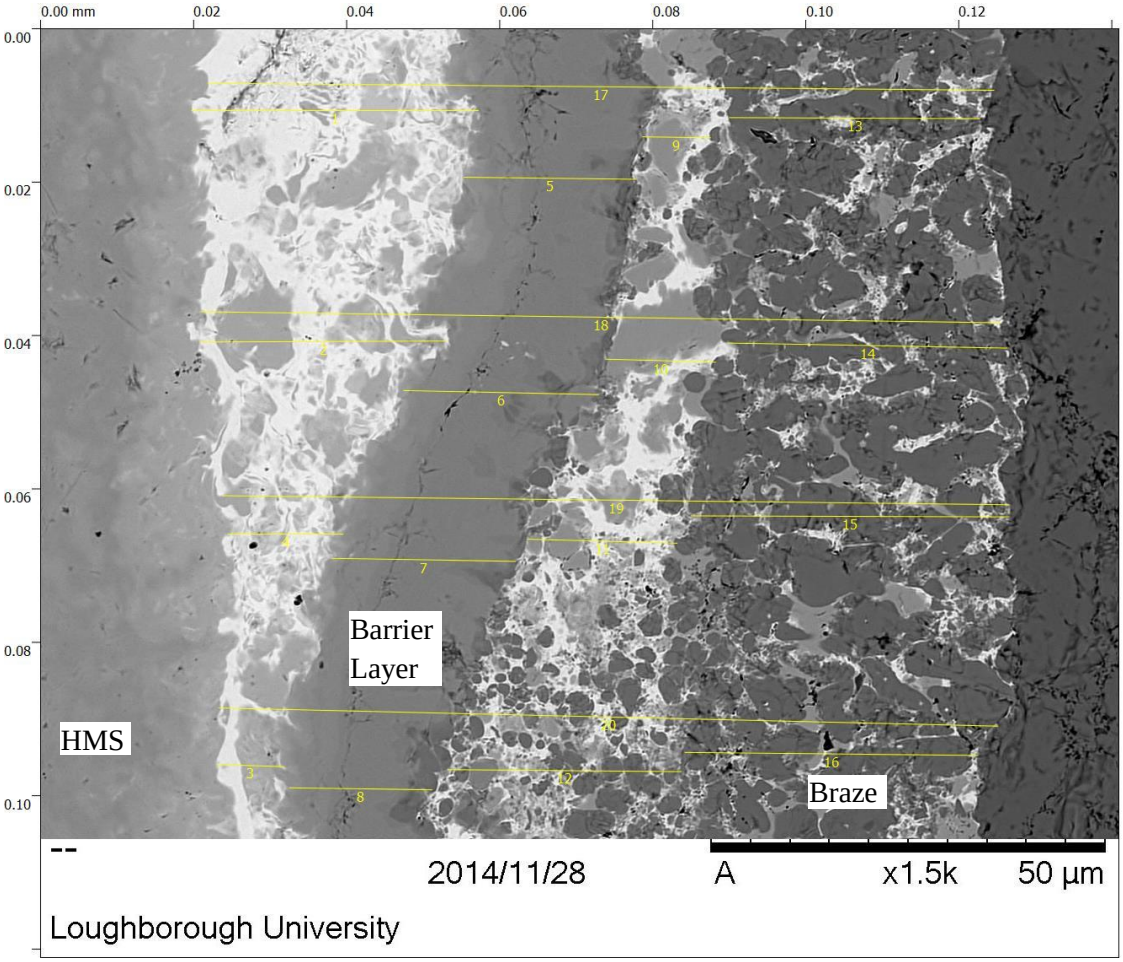

Figure 63. SEM image of junction interface after brazing for 10 minutes at 700oC. Measurements of layers in the bond line are taken which are displayed in appendix item 4 (A4).

It is clear from the image in Figure 63 that regardless of the contact resistance, this is a poor junction that would fail rapidly in operation. Dimensional and compositional measurements were taken on this image and are summarised in appendix item 4. A variety of intermetallic phases have formed on either side of the nickel barrier layer. The distortion of the barrier layer is caused by the different intermetallic phases which have formed between the barrier layer and higher manganese silicide. Copper, nickel and silver have diffused through the nickel barrier layer and formed thick layers. Manganese has also diffused into the nickel barrier layer, but has not transferred into the silver braze. Overheating of the assembly during the brazing process may have caused the breakdown of the barrier coating. This is possible as at there was no direct measurement of temperature inside the jig or on the sample.

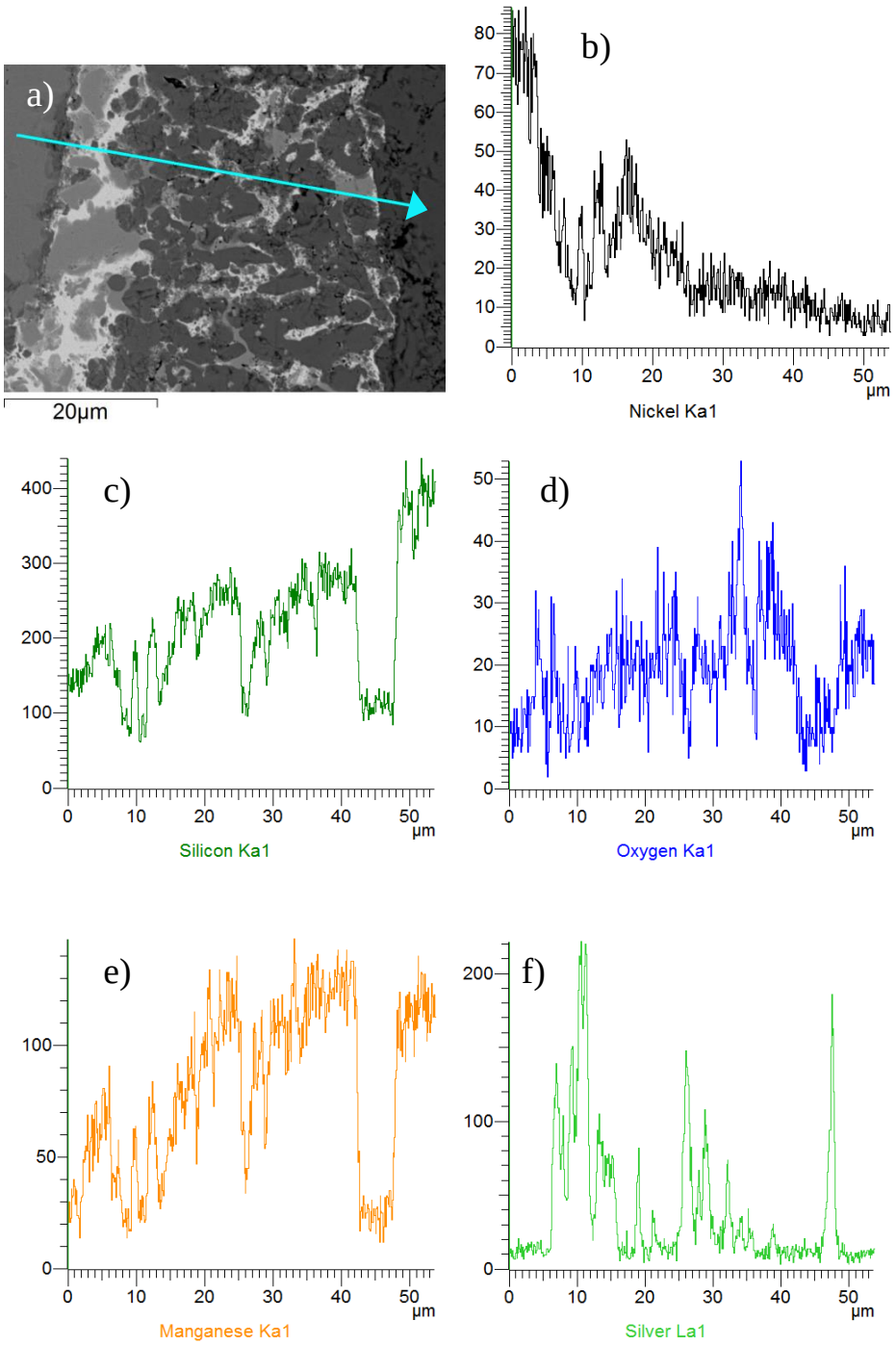

Figure 64. a) SEM image of junction interface after brazing for 10 minutes at 700oC. The cyan line represents the line scan XPS data area. b-f) EDS line scan data for the HMS interface.

XPS analysis represented in Figure 64 shows how silver has diffused into the manganese silicide and has collected around the separated semiconductor grains. Comparing the silicon and manganese signatures (‘e’ and ‘c’), it can be observed that the two readings match, implying that a compositional breakdown of the semiconductor material has not occurred in the presence of silver. The silver trace also peaks where the manganese-silicon signatures trough, further indicating that the silver has collected as opposed to reacting. Finally, the

junction contains very low readings of oxygen which show promise for the process should the processing conditions be improved.

The contact resistivity for the 10-minute sample is measured to be 33.00 μΩ.m, shown in Table 3. At 12.5 minutes brazing time the contact resistivity drops to 21.30 μΩ.m. It is clear that if damage occurs after 10 minutes of brazing at 700^{o}C, the damage will worsen as time increases.

Similarly to the magnesium silicide sample, the manganese silicide material is tested at brazing temperatures of 650^{o}C and 630^{o}C for 10 minutes, to better suit the IML/QMUL material processing requirements. Appendix item 3 contains the characterization data for these samples. The sample brazed at 650^{o}C had an average contact resistivity of 17.10 μΩ.m and the sample brazed at 630^{o}C had a contact resistivity of 17.40 μΩ.m. Both samples have a lower contact resistivity than the 700^{o}C brazing samples which indicates that less damage to the interface is incurred during the brazing process. It is intended that in future work, compositional analysis will be carried out on cross sections of these samples to verify the properties of the junction that is brazed at the lower temperature end. It is known from the chemistry of the samples that higher manganese silicide is much less reactive in comparison to the magnesium silicide material and so it is believed that there is sufficient enough data to conclude that these processing parameters are acceptable.

4.2.4 Toyota 7-Couple device characterisation

A 7-couple prototype device is built using the pre-contacted magnesium silicide and higher manganese silicide produced by Toyota. Johnson Matthey Silver-flow 56 braze paste is used as the joining alloy and the brazing conditions identified for lowest contact resistance were used (argon flow at 630^{o}C for 10 minutes with a gas pressure of 0.25 Bar).

An image of the prototype module is shown in Figure 65. The device was then tested using the module characterisation equipment described in Section 2.5.3.

Figure 65. 7-couple silicide module made using Toyota/Yasunaga semiconductor material.

Figure 66 shows the I-V characteristics and power output from the module when in operation under a 300°C temperature differential between 18°C and 318°C.

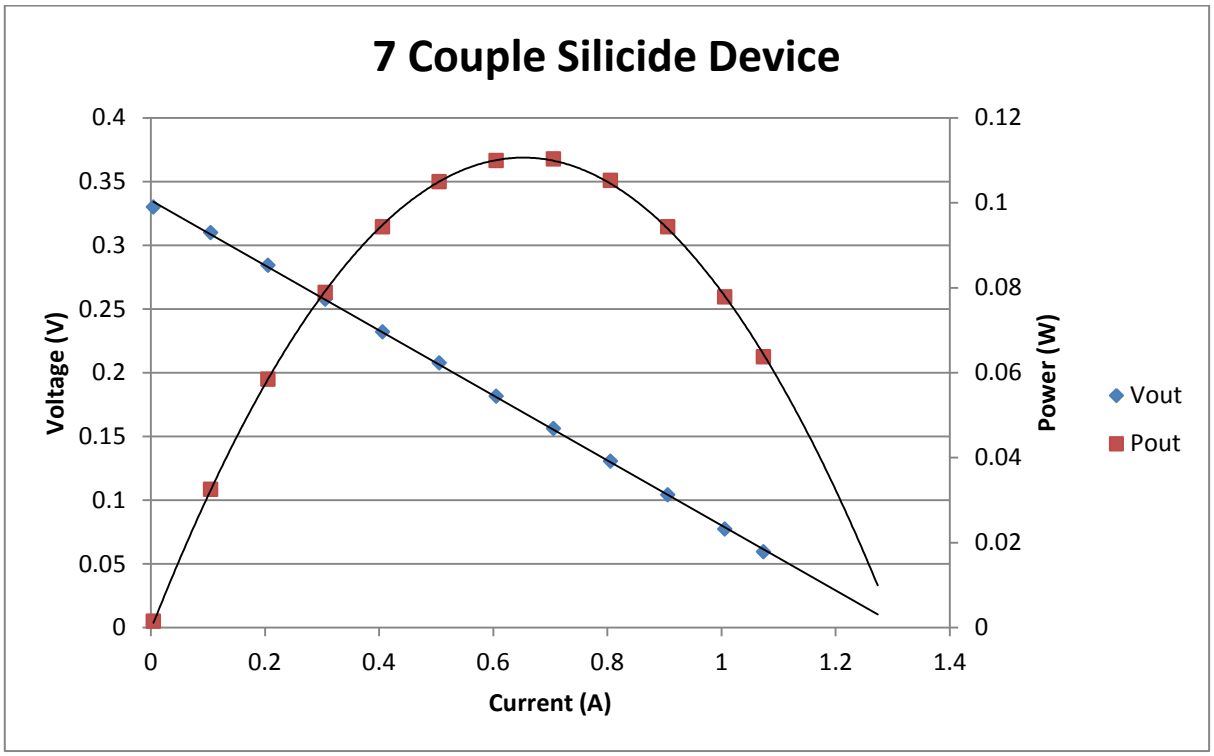

Figure 66. Module output graph for a 7-couple device characterised in a temperature differential test rig, showing I-V characteristics and derived Power output for the device.

The maximum power output is measured to be approximately 115 mW at 175 mV and 650 mA. The resistance of the module before testing is taken at 130 mOhms. After testing the device, the resistance is measured at 350mOhms. The peak power operating data indicates

that the maximum power point occurs at approximately 270 mOhms. Finally, the power density is calculated at 130.29 mW/cm^2 for a temperature difference of 300^oC.

A number of factors can be taken into account for this resistance change. Oxidation of the braze contacts is the most likely cause of the increased resistance. If components of the braze alloy react with oxygen the electrical conductivity will be reduced and the cross sectional area of the contact will reduce, leading to a higher resistance. Secondly, oxidation and sublimation within the pellets could occur thus changing the overall resistivity or effective size of the pellets. This issue can be addressed using oxidation and sublimation coatings for the pellets or running the device in an inert atmosphere.

4.3 IntrinsiQ materials and QMUL Material Study

As mentioned at the beginning of this chapter, the aim is to replicate the joining process developed for the Toyota silicide material with the material produced by IML and QMUL. The magnesium silicide material is doped with tin, in replacement to antimony; this increases the average ZT and peaks at a maximum value of 1.2-1.4 at approximately 720 K. This greatly outperforms the Toyota material but in turn is more reactive, causing it to be more difficult to achieve a good ohmic junction. In this section, the development of barrier layers on magnesium silicide and higher manganese silicide are outlined in an attempt to passivate the surface to achieve acceptable electrical, mechanical and thermal junctions between the semiconductor and metallic straps.

4.3.1 Plating of Magnesium Silicide Barrier Coatings

Preliminary studies showed that electroplating directly onto the magnesium silicide material is not feasible due to the reactivity of magnesium alloys and acidic solutions. Certain methods can be employed which have specific chemical etching processes to remove the native oxide; involving hydrofluoric acid, thus being out of scope for this line of research. As a result of this, sputter coating is employed to form a seed layer on which to electroplate a thicker contact layer onto.

Initially, alternative methods to the standard plating processes for electrodepositing onto the magnesium silicide are attempted. A process used for plating aluminium is tested for its ability to deposit a nickel barrier layer onto the magnesium based semiconductor. Magnesium-based alloys and aluminium have certain similarities in that both form a native oxide on the surface that causes difficulty in effectively depositing metals onto the surface via a chemical process. A chemical process is desirable for cost effectiveness and upscaling; also it involves minimal wastage of materials. The method in question is based around an acid activation followed by zinc deposition to prepare the surface for plating. An acid bath is used to remove the native oxide layer to expose the alloy; this is known as an activation stage. The sample is then cleaned and submerged into a zincate solution; during this stage, zinc deposits onto the surface of the material creating a passive and electrically conductive base layer. Typically, the first two steps are repeated to produce a dense zinc seed layer for the final plating step. The nickel plating step comprises of a standard Watts bath with a nickel anode that provides ions for cathodic electrodeposition onto the sample. The solution contains deionized water, nickel chloride, nickel sulphate and the pH is stabilised with boric acid.

Equation 5 is used to calculate the plating duration for a particular current density to control the thickness of the deposited layer.

$$t = \frac{d}{0.205eJ} \qquad (5)$$

Where:

t = time of deposition (min)
d = thickness of deposition (μm)
e = cathode current efficiency
J = current density (A/dm^2)

A starting current density is chosen at 7 A/dm^2 and an efficiency of deposition of 95.5% is estimated for this process [57]. For a 5 μm deposit, a plating time of 3 minutes and 36 seconds is calculated for a 1.767 cm^2 sample.

Table 9 outlines the composition of the plating baths and the temperatures they are held at during the process.

Bath Type	Composition	Temperature (^{o}C)
Activator	100ml deionised water +25g of acid salts	Room Temperature
Zincate	30ml deionised water + 10ml Zincate solution	Room Temperature
Nickel Plating	100ml deionised water + 37.5g nickel plating salts	50^{o}C

Table 9. Compositions of the baths used for plating of magnesium silicide.

The following process is carried out for plating of the samples:

1. MgSi surface polish with P2500 grit SiC paper.
2. Clean with acetone followed by isopropanol.
3. Immediately immerse in Activator for 20s.
4. Rinse 5s in DI water.
5. Immerse in Zincate 20 s.
6. Rinse 5s in DI water.
7. Immerse in Activator 20 s
8. Rinse 5s in DI water.

9. Immerse in Zincate 20 s.
10. Rinse 5s in DI water.
11. Immerse in Plating bath.
12. Apply voltage for 3 minutes and 36 seconds.
13. Clean with DI water, acetone and isopropanol followed by drying using dry nitrogen supply.

The plating approach is carried out on two samples; one sample is heat-treated under the regime developed for the Toyota material (10 minutes at 730^{o}C under argon flow with a gas pressure of 0.25 Bar) after plating and the second sample remains untreated.

Immediately after the plating process, significant damage to the surface can be observed as the plated layer is loosely attached and a black layer is exposed in the interface. After the heating process, further degradation occurs. Figure 67 shows a cross-sectional SEM image of the sample interface.

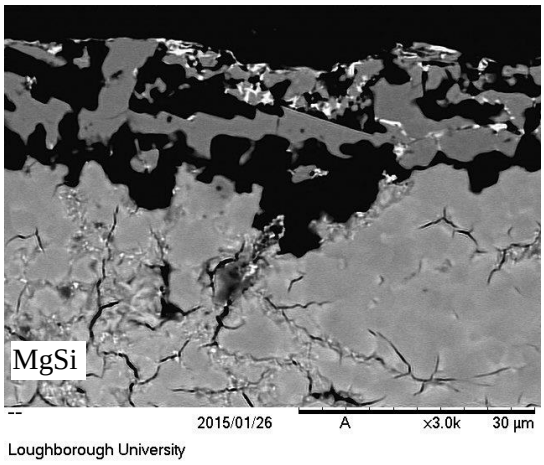

Figure 67. SEM cross-sectional image of a nickel electroplated sample of magnesium silicide manufactured by IML/QMUL, after undergoing the developed brazing conditions for the Toyota manufactured material.

Severe degradation of the surface occurs during the process and after further heat treatment it is clear that the conditions used in this process would not provide a suitable surface for brazing to achieve an electrically and thermally stable contact. A possible cause for this occurrence is that the deposit is either being formed too quickly (violently) or too slowly (exposed to acid for too long). If the deposit is applied too quickly, the liberation of hydrogen in the reduction process at the surface may cause damage. Bubbles form which can cause mechanical damage to the surface and cause the deposit to develop unevenly as the solution is separated from the surface. Residual stresses in the plating layer which may be why cracks can be observed under the surface of the magnesium silicide material. Furthermore, if the

deposition rate is too slow, prolonged exposure of the surface to water molecules increases the possibility of the free magnesium in the semiconductor material to reduce the water molecules forming magnesium oxide and hydrogen gas. The time parameter can be modified by changing the current density during electrodeposition; this is effectively the rate of deposition. To verify if the deposition rate affects the quality of the deposit, two current densities are applied at 5 A/dm^2 and 9 A/dm^2. A 5μm deposit is maintained; to achieve this, a corresponding plating time is calculated for each current density at 5 minutes and 8 seconds and 2 minutes and 51 seconds respectively.

Figure 68 shows the SEM cross section for the 5 A/dm^2 sample. A degradation layer has formed at the barrier interface causing delamination of deposit. The deposit is measured with an average thickness of 4um which indicates that the actual deposition efficiency is 0.76 (0.8 x 0.955) in comparison to the estimated efficiency of 0.955. Severe parallel cracking can be seen in the inward layers from the deposition surface. Notably, the cracks occur through grains that may indicate that internal stresses are being relieved in the thermoelectric material. This shows a different mode of degradation, as previous results have shown inter-granular cracking that could arise from a reaction in the phase material between the crystals in the solid solution.

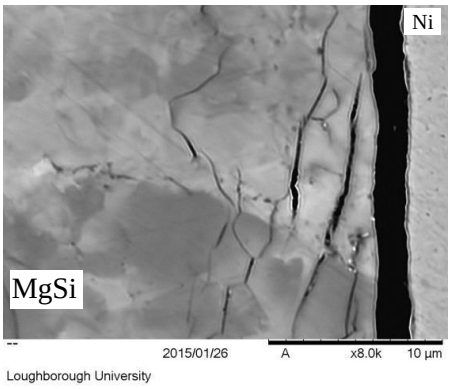

Figure 68. SEM cross-sectional image of a nickel electroplated sample of magnesium silicide manufactured by IML/QMUL. The deposition is carried out with a current density of 5A/dm^2.

Figure 69 shows an SEM cross-section of the sample deposited with nickel at a current density of 9 A/dm^2. Severe degradation in comparison to the lower current density plating trials is observed. The deposit is not in contact with the thermoelectric material and cracking has occurred in the inner layers of the material. Cracks have formed at angles that are normal to the surface indicating that there could be a relationship between the deposition rate and degradation. The grain structure is less defined at the surface that indicates that the material has reacted with the electrolyte solution.

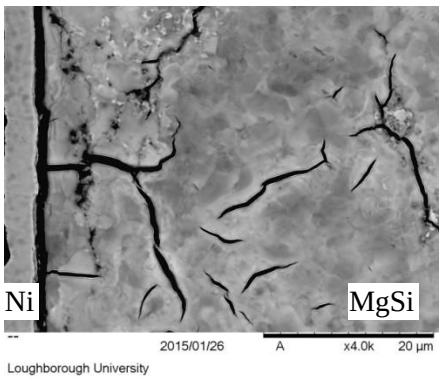

Figure 69. SEM cross-sectional image of a nickel electroplated sample of magnesium silicide manufactured by IML/QMUL. The deposition is carried out with a current density of 9A/dm^2.

The results show that a complete decomposition of the thermoelectric material occurs at the surface of the pellet. Widespread delamination of the plating layer and sputter layer occurs and the interface and etching has occurred at the semiconductor surface. One possible mode of this occurrence could arise from low-density magnesium oxide production on the semiconductor surface which is then liberated into the solution aided by agitation from hydrogen gas production in the process. The spectrum shows a high oxygen content in all of the phases between 20-30%. Cracks are formed to a depth of up to 300 um which may have arisen from inter-granular corrosion.

It is proposed that electroless deposition of nickel may be more effective as it offers greater control over the deposition process due to the simpler equipment setup. Electroless deposition works by a surface chemical reaction assisted by acid etching to activate the surface. Due to the nature of magnesium silicide, it is particularly reactive with acids; forming a nonprotective oxide layer as explained by the Pilling-Bedworth ratio of 0.806. Electroplating solutions tend to have a lower pH due to the inclusion of Boric acid for surface sensitization during the process; whereas electroless solutions rely on pre-sensitization and an autocatalytic process for deposition with a more neutral pH. Many literature studies [56, 58] state that hydrofluoric acid (HF) is the most effective pre-treatment etch for magnesium based alloys; this chemical is highly corrosive and needs specific handling conditions that are not suitable for this study. The HF etch produces a thin film of magnesium fluoride which improves the deposition efficiency of the electroless process. As an alternative, dry polishing is carried out as the pre-treatment process and an acetone and isopropanol cleaning stage is used for de-greasing. This has been shown to produce a thinner oxide layer in comparison to wet polishing, shown in the histogram in Figure 70 [59].

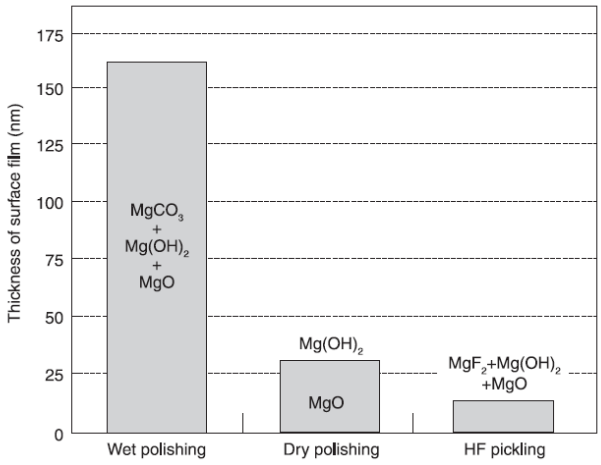

Figure 70. Histogram comparing the thicknesses of oxide films on magnesium alloys after three different polishing/etching methods [31].

The electroplating process is modified by replacing steps ‘11’ and ‘12’ with a timed dipping step into an electroplating solution to deposit a 5µm film. The plating bath formulation deposits at a rate of 7.06 nm/s and so a total plating time for a sample is calculated at 11 minutes and 49 seconds.

The plating bath relies on the reduction of nickel chloride and nickel phosphate at the surface. A number of additional additives are included for pH stabilisation and aiding in the dissolution of the plating salts. The plating bath chemicals are supplied by Caswell Inc (www.caswellplating.com) in a two part system that involves mixing specific quantities of

the solutions with deionized water. The plating process is carried out at an elevated temperature of 80^{o}C as required for the autocatalytic deposition process.

The electroless plating process is carried out on a magnesium silicide sample after the ten preparation steps from the cathodic deposition process are applied. A sample is cross sectioned and analysed using SEM imaging which is shown in Figure 71.

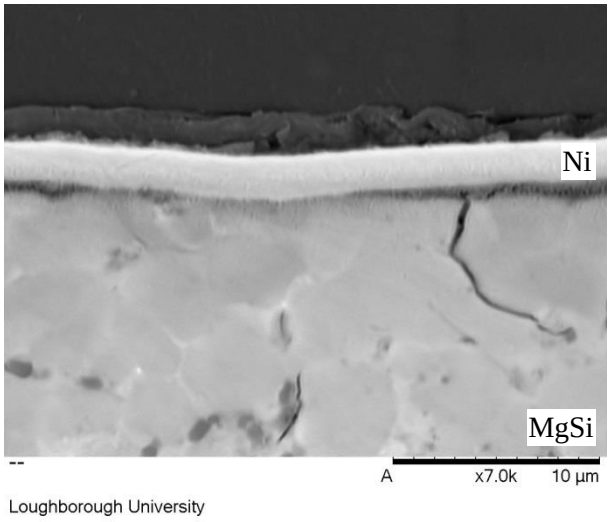

Figure 71. Cross-sectional SEM image of a magnesium silicide sample with a 5µm nickel layer deposited using an electroless nickel process.

The results of this test show a small improvement in barrier layer adhesion in comparison to the samples that are electroplated. Cracking under the surface is observed which increases the surface area, allowing the mildly acidic solution to react with the surface producing an oxide layer. In places, the oxidation reaction dominates the process and so the reduction of the nickel salt does not occur directly onto the semiconductor surface. In some locations, the nickel layer appears to have deposited onto the surface with no interstitial layer but this occurs less frequently along the layer then when an interstitial layer is observed.

This experiment shows an improvement of the process by switching from an electrical potential driven process to an autocatalytic process. Nonetheless, it is clear that the surface preparation stages are not sufficient to enable effective chemical deposition of nickel onto the magnesium silicide alloy. The surface is etched too violently and an oxidation reaction produces a loosely adhered layer that is not sufficient to bond the nickel deposit. This is likely to produce a junction a low electrical, thermal and mechanical properties. It is expected that the cracking may arise from selective etching as the magnesium silicide is a solid solution of magnesium-tin, magnesium silicide and tin silicide. It is likely that the magnesium rich phases are etched more readily than the other phases. The cracking may also arise from

an expansion at the surface caused by the surface reactions which lead to internal mechanical stresses; these stresses eventually relax and manifest as cracks.

Literature [56, 58] suggests that a process using particular chemicals may be successful, using fluoride based etchants but the use of such chemicals means that specific equipment and expertise are required which is out of the scope of this study.

There are numerous alternative methods for deposition of metals onto substrates. Few of which are considered as economically viable for industrial processes in comparison to electroplating, but for this particular material, sputter coating is the second most economically viable process. A combination of sputter coating as a seed layer to aid the adhesion of a chemical plating process is explored as the next step.

A 30 mm diameter disc of tin-doped magnesium silicide is coated with a seed layer of nickel at a thickness of 1μm using a Quorum Q150T turbo-pumped sputter coater under an argon atmosphere. Of the two chemical plating processes previously tested, electroless plating is used to deposit a 5 μm nickel layer onto the nickel sputtered sample. The autocatalytic process is chosen, owing to the previous results showing more promise over the electrical potential driven process for effectively depositing a nickel layer. The surface preparation stages (1 – 10) from the electroplating process are not applied for this test as they are deemed too destructive and the acidity of the electroless plating solution is expected to remove any oxidation that has formed on the sputtered layer.

Following the deposition process, the sample is cross sectioned and characterised using SEM imaging. Upon initial inspection by eye, the deposit appears to have adhered to the surface effectively, but small protuberances are observed in an even distribution across the surface. Cross-sectional SEM imaging reveals that the protuberances are areas of the coating at which a reaction with the surface has occurred. This leads to increased internal stress forming at a point; upon sectioning, the surface breaks indicating that under brazing conditions the likelihood of a reaction with the surface is increased. Although a low electrical conductivity and high mechanically stable junction may be achieved with this type of barrier layer, the longevity of the junction would be compromised as the reaction would continue over time under operation. Figure 72 shows that the points at which the reactions occurred may have arisen due to breaks in the sputtered layer; an example of a break in the plated layer is shown in Figure 73.

Pits can be observed in the sputtered layer at high magnification as shown in Figure 72. In Figure 73, cracks can be observed which emanate from the surface of the semiconductor from points at which breaks in the sputtered layer are identified. The pits in the sputtered layer are likely to be a result of both the sputtering process and the surface preparation. The sputter

coater used is a research/lab scale piece of equipment which requires a particular setup for each sample; this is achieved by multiple experiments to tune the parameters. Due to a low number of samples being available, and limited availability of the equipment, an in-depth study of the setup parameters could not be carried out for this equipment and process. Furthermore, in some cases, thinning of the sputtered layer is observed where troughs are present. The troughs or scratches are likely to manifest during the grinding stage, at which debris is dragged across the surface causing a groove. This effect cannot be avoided completely, but can be reduced by grinding at a slower rate.

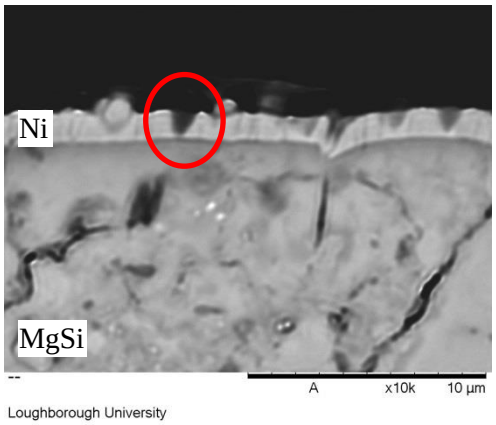

Figure 72. Cross-sectional SEM image of a magnesium silicide sample with a 1µm sputtered nickel seed layer. The area highlighted in red shows an area at which there is a break in the sputtered layer.

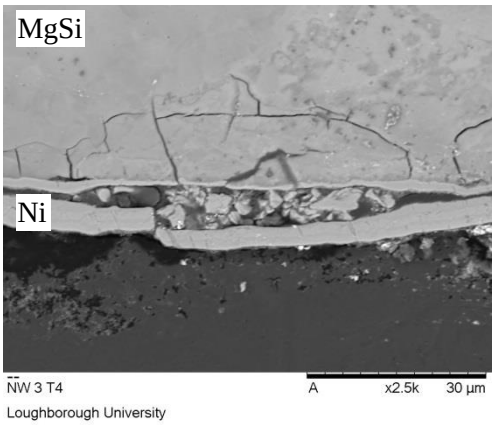

Figure 73. Cross-sectional SEM image of a magnesium silicide sample with a 1µm sputtered nickel seed layer and a 5µm nickel layer deposited using an electroless nickel process. A break in the plated layer is likely to arise from a break in the seed layer as shown in Figure 72.

It is clear that a more conformal sputter coating is necessary to define the suitability of a chemical deposition process for the nickel barrier coating. For this reason, the sputter coating is carried out by TEER Coatings Ltd, a company with vast experience in physical vapour deposition (PVD) and more advanced equipment for depositing barrier layers.

A dense 1µm nickel layer is deposited onto a sample of tin-doped magnesium silicide. Figure 74 shows a cross section of the magnesium surface with nickel deposited onto it. The deposit has few defects and there are fewer troughs in the surface owing to the slower grinding rate used for surface preparation.

After electroless nickel deposition, the sample is cross sectioned and analysed using scanning electron microscopy. Figure 75 shows an image of the interface cross-section. The sputter layer has been etched or dissolved off the surface of the semiconductor and a loosely attached nickel deposit is formed over the debris of the sputtered layer. The nickel layer is verified to be the electroless deposit due to the thickness, which in the image is approximately 4 µm. A possible explanation for the removal of the sputtered layer in this process is that internal

stresses were present in the deposited layer. Upon mild etching from the acidic electroless depositing solution, the sputter layer thickness will have been reduced to a point at which it breaks under the stresses. This causes a cascade effect that breaks up the remaining sputter layer. As there is still a surface available, the solution still creates a deposit as the debris enables nucleation of the depositing nickel ions to form a loosely bound surface layer of nickel.

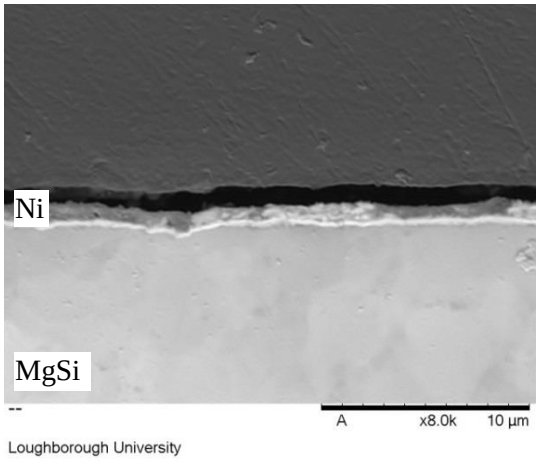

Figure 74. Cross-sectional SEM image of a magnesium silicide sample with a 1µm sputtered nickel seed layer by TEER Coatings Ltd.

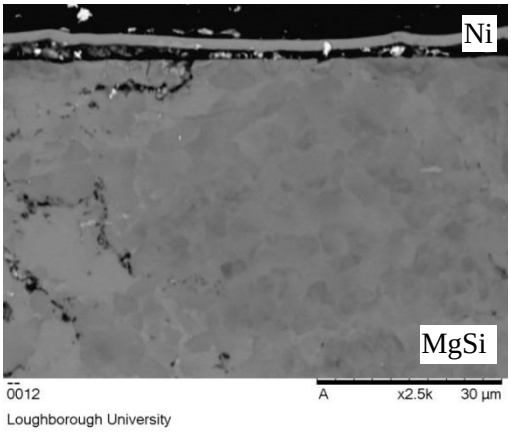

Figure 75. Cross-sectional SEM image of a magnesium silicide sample with a 1µm sputtered nickel seed layer (deposited by TEER Coatings Ltd) and a 5µm nickel layer deposited using an electroless nickel process.

Little improvement is made for depositing a stable barrier layer onto the magnesium-tin silicide. As this process is not suitable for the n-type magnesium alloy, it is not tested on the p-type manganese alloy. It is necessary to develop a process that is suitable for both silicide materials as the joining process is carried out for both materials at the same time on each material when producing a module. Having two different joining surfaces for the two types of pellets is undesirable, as the likelihood that both surfaces have the same bonding properties is unlikely. For this reason, thicker sputter layers are tested for their suitability as barrier layers for the silicide semiconductors.

4.3.2 Sputter Coating of Magnesium Silicide Barrier Layers

Results from the plating trials show that this method alone is not suitable as a metallization process for the magnesium based semiconductors. The acidity of the plating solutions causes an oxidising reaction between the surface of the semiconductor and the solution; thus damaging the electrical and mechanical properties of the surface. Sputter coating as a seed layer for electroplating is also explored and results show that this does not offer an effective approach for barrier coating. It is apparent that the thin seed layers are stripped away by the solution in a manner similar to an acid etch process. Another possibility is that the seed layer is discontinuous or slightly porous and so the solution is still able to reach the semiconductor surface and react. It is unclear from SEM imaging which mode of failure is causing the reaction alone, but it is seen in some cases that the sputtered layer is broken in places and so adhesion and surface roughness properties may be a factor in this process.

Sputter coating offers an approach for metallization that may be less damaging than plating. The deposition is carried out in an inert atmosphere and can enable a greater complexity of coatings in multiple layers and compositions while causing minimal damage to the surface from oxidation. Sputter coating alone is explored for its protective qualities in joining trials. The effect of adhesion layers and surface preparation are tested initially for their effectiveness as barrier layers.

Six different sputter coated trials are carried out on various magnesium silicide samples and one higher manganese silicide sample. The effect of polishing and grinding with water based or water free coolant/lubricant is explored with regards to coating adhesion and joining quality. Furthermore, various coating combinations are deposited onto the samples that are tested at brazing temperatures of 630^{o}C and 650^{o}C. Brazing temperatures at 650^{o}C and below are being explored to ensure that the samples do not exceed temperatures within 100^{o}C of the sintering temperature (750^{o}C). Due to the number of samples tested, the information will be omitted from the main body of this document, a list of samples can be found in the appendix.

The effect of a 300 nm titanium adhesion layer is investigated with a 1.2 μm thick nickel barrier layer; the inclusion of a 30 nm gold sealant layer is explored additionally; to reduce oxidation before joining trials. Characterization of samples is carried out using SEM analysis, energy dispersive X-ray spectroscopy (EDS) and four point probe contact resistance.

4.3.2.1 Ti/Ni Sputter Coated Samples: Brazing Time Dependency

Firstly, to demonstrate the importance of brazing time, tests with a number of TiNi samples are carried out at times around the 10 minute period for brazing developed for the Toyota material. The time periods within the furnace under an argon flow atmosphere are 6 minutes, 8 minutes and 12 minutes at 630^{o}C with a gas pressure of 0.25 Bar. Figure 76 Figure 81Figure 81 are acquired using a field emission gun-SEM (FEG-SEM) and compositional analysis is drawn from EDS data.

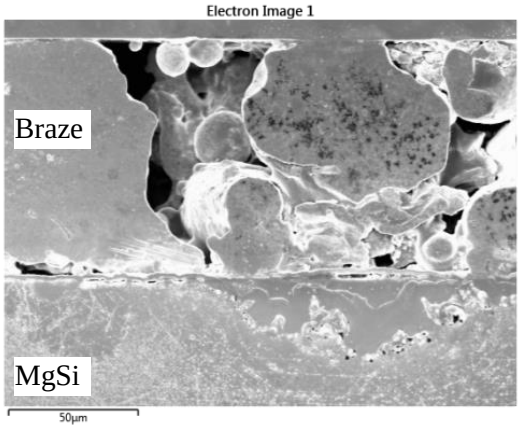

Figure 76. Cross-sectional SEM image of a magnesium silicide sample with a 300nm titanium adhesion layer and a 1.2µm sputtered nickel seed layer. Brazed at 630oC for 6 minutes.

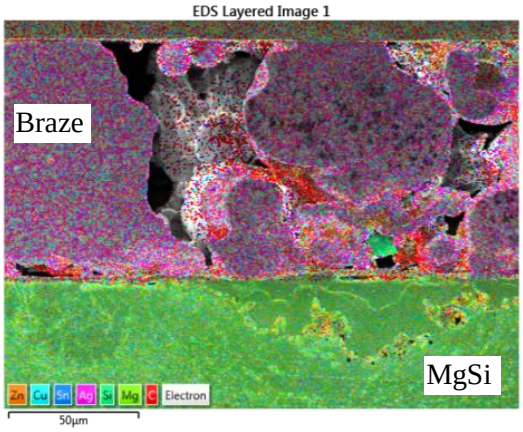

Figure 77. Cross-sectional EDS image of a magnesium silicide sample with a 300nm titanium adhesion layer and a 1.2µm sputtered nickel seed layer. Brazed at 630oC for 6 minutes.

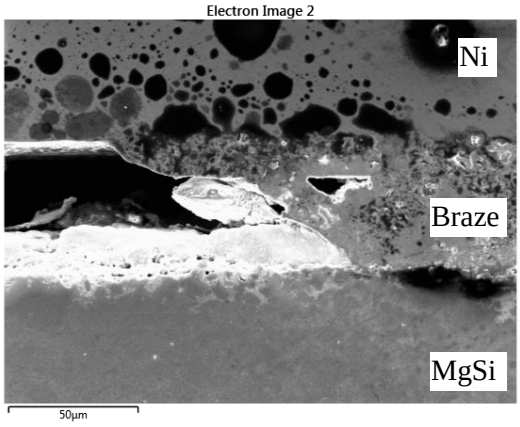

Figure 78. Cross-sectional SEM image of a magnesium silicide sample with a 300nm titanium adhesion layer and a 1.2µm sputtered nickel seed layer. Brazed at 630oC for 8 minutes.

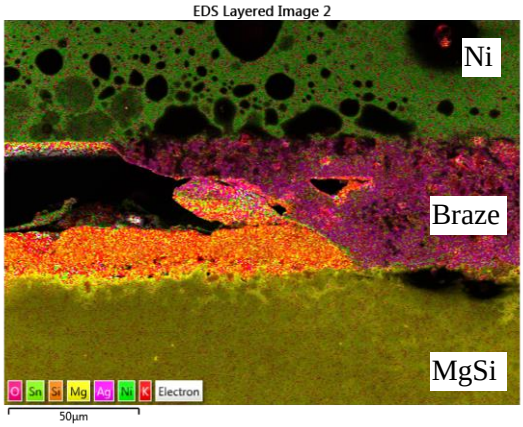

Figure 79. Cross-sectional EDS image of a magnesium silicide sample with a 300nm titanium adhesion layer and a 1.2µm sputtered nickel seed layer. Brazed at 630oC for 8 minutes.

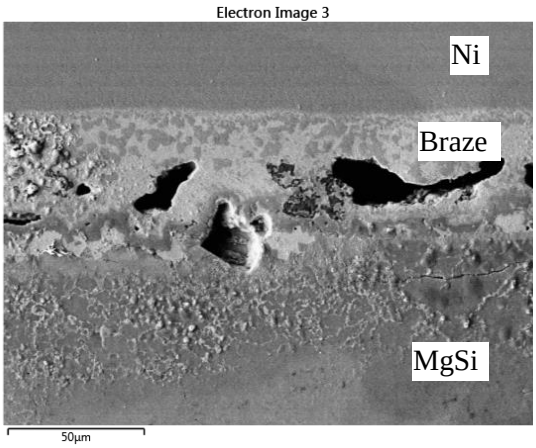

Figure 80. Cross-sectional SEM image of a magnesium silicide sample with a 300nm titanium adhesion layer and a 1.2µm sputtered nickel seed layer. Brazed at 630oC for 12 minutes.

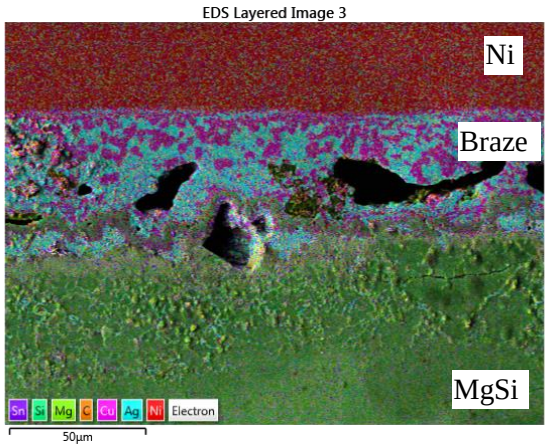

Figure 81. Cross-sectional EDS image of a magnesium silicide sample with a 300nm titanium adhesion layer and a 1.2µm sputtered nickel seed layer. Brazed at 630oC for 12 minutes.

Analysing the junction qualitatively, it can be seen that the alloy has not sufficiently flowed for the tests at 6 minutes and 8 minutes firing time. The alloy is clearly approaching the flow temperature but has not wetted in the joint thus leaving voids in the interface. Although this may give an acceptable contact resistance, the mechanical and thermal properties of the joint will be poor. After 12 minutes firing time, the alloy has flowed into the joint but due to the extended period at brazing temperature, diffusion of silver has occurred and the barrier layer has broken down, resulting in an interstitial layer of reacted magnesium and silver. The cyan coloured trace in Figure 81 represents silver which is split by a green layer representing magnesium and silicon. The nickel barrier layer cannot be distinguished on the surface of the magnesium silicide indicating that it has broken down and diffused into the junction. This has allowed the braze material to react with the magnesium silicide.

Brazing at 630^{o}C for 10 minutes results in a higher quality junction. Figure 82 and Figure 83 show how the braze filler metal has wetted into the joint evenly and has caused no damage to the magnesium silicide material. Four point probe resistance measurements on the sample give an average sheet resistivity for the contact as 835.00 ± 6.69 µΩ.cm^{2}. In comparison to the sheet resistivity of the Toyota magnesium silicide (refer to appendix figure 3), with a value of 5.13 ± 0.33 µΩ.cm^{2}, this is significantly more resistive. With no immediate signs of diffusion or barrier breakdown in the titanium nickel sputter layer, it can be estimated that the extra resistance may be arising from between the layers at the magnesium silicide-titanium, titanium-nickel or nickel-silver braze interfaces.

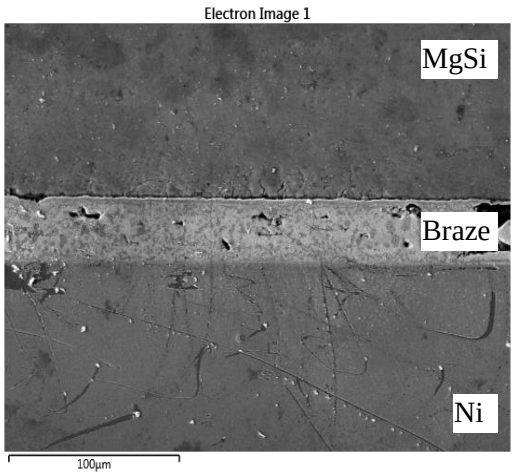

Figure 82. Cross-sectional SEM image of a magnesium silicide sample with a 300nm titanium adhesion layer and a 1.2µm sputtered nickel seed layer. Brazed at 630oC for 10 minutes.

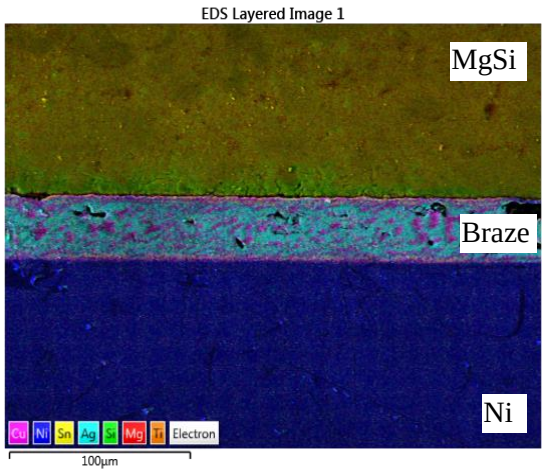

Figure 83. Cross-sectional EDS image of a magnesium silicide sample with a 300nm titanium adhesion layer and a 1.2µm sputtered nickel seed layer. Brazed at 630oC for 10 minutes.

As it is unclear as to how the extra resistance is occurring, a brazing test is carried out at a higher temperature of 650^{o}C for 10 minutes. This will give an indication of whether the braze is just beginning to degrade the barrier layer during the 630^{o}C brazing trial for 10 minutes. Figure 84Figure 85 show the cross-sectional SEM image and EDS data for this test.

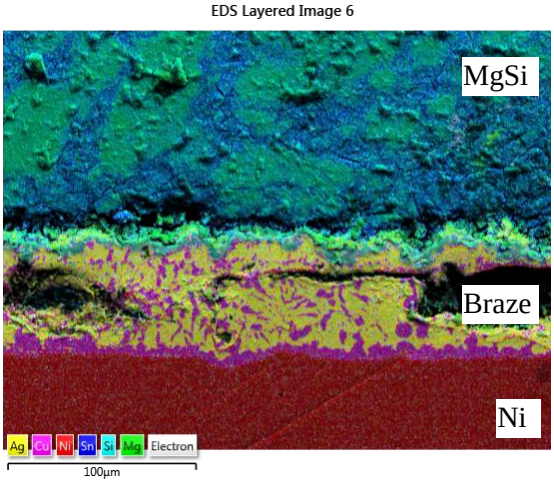

Figure 84. Cross-sectional SEM image of a magnesium silicide sample with a 300nm titanium adhesion layer and a 1.2µm sputtered nickel seed layer. Brazed at 650oC for 10 minutes.

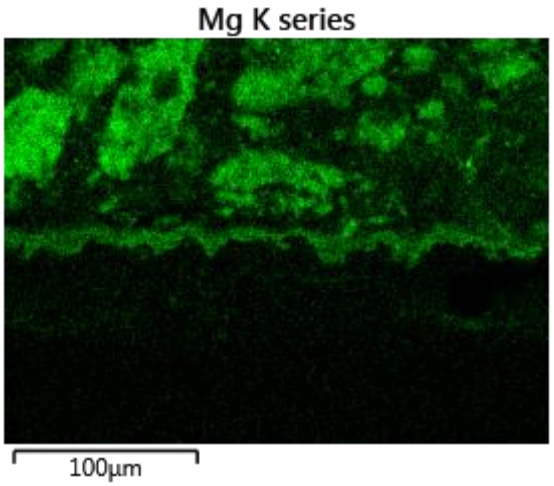

Figure 85. Cross-sectional EDS image of a magnesium silicide sample with a 300nm titanium adhesion layer and a 1.2µm sputtered nickel seed layer. Brazed at 650oC for 10 minutes.

The results show that for a sample heated at 650°C for 10 minutes, the braze alloy has flowed in the interface, but diffusion of magnesium has occurred. This gives a possible insight into what is happening during the 630°C brazing trial. The onset of barrier layer degradation may be occurring at the nanoscale, which cannot be easily identified with SEM or EDS.

It is important to continue testing braze temperatures of 650°C alongside tests of 630°C as if the braze is acceptable at both temperatures, it is likely to be more robust in operation at elevated temperatures. It will also verify that damage to the barrier layer is not beginning to occur during the lower braze temperature; this way it instils more confidence into the robustness of a barrier layer if it is successfully joined.

4.3.2.2 Ti/Ni/Au Sputter Coated Samples and the Effect of Aqueous and Non-Aqueous Cutting Fluid

A test that can be carried out to identify if any of the particular interfaces in the barrier layers are responsible for the increased resistance is done by applying a thin layer of gold as the final step of the coating. This prevents oxidation of the surface as gold is nobler than nickel. If the braze joint is improved, it can be deduced that an oxide layer has formed in the nickel layer for the non-gold sample. If there is a thick enough oxide layer, the flux in the braze paste will remove this, causing thinning of the barrier layer. Figure 86 toFigure 89 shows the cross-sectional SEM images of this test.

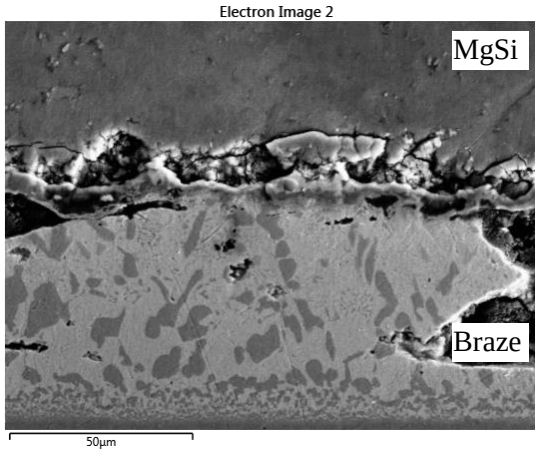

Figure 86.Cross-sectional SEM image of a magnesium silicide sample with a titanium nickel barrier and a gold capping layer. Brazed at 630oC for 10 minutes.

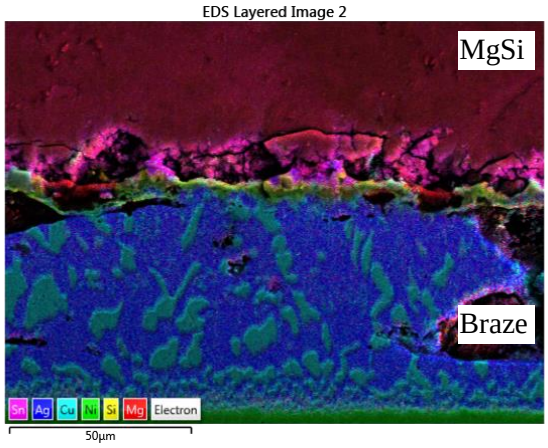

Figure 87. Cross-sectional EDS image of a magnesium silicide sample with a titanium nickel barrier and a gold capping layer. Brazed at 630oC for 10 minutes.

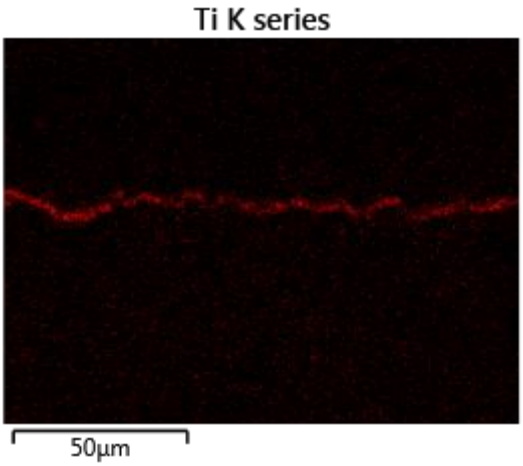

Figure 88. Cross-sectional EDS titanium map of a magnesium silicide sample with a titanium nickel barrier and a gold capping layer. Brazed at 630oC for 10 minutes.

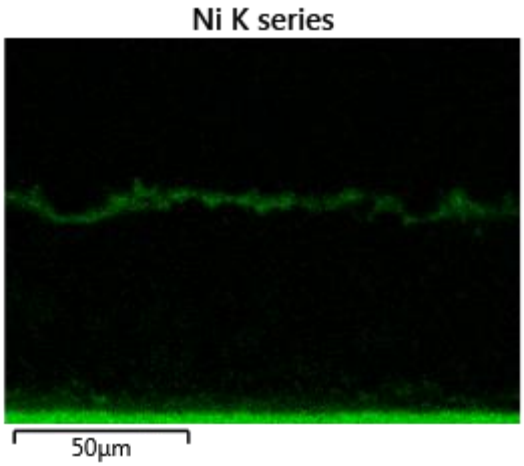

Figure 89. Cross-sectional EDS nickel map of a magnesium silicide sample with a titanium nickel barrier and a gold capping layer. Brazed at 630oC for 10 minutes.

The microscopy results show that the interface has been damaged between the barrier coating and semiconductor material. The barrier coating is still present after brazing but appears to be more diffuse than expected; implying that diffusion may be occurring. The discolouring at the interface shows a mixture of elements indicating that diffusion has occurred. Magnesium is observed in the dark voids of the braze and in some cases magnesium has migrated into the cracked region of the interface. The sheet contact resistance for this sample is measured at 1020.00 ± 6.53 $\mu\Omega.cm^2$. The contact resistance has increased with the addition of a gold capping layer when comparing the samples with and without the gold layer, the major difference is observed between the titanium adhesion layer and the magnesium silicide. The surface of the magnesium silicide is severely cracked; this is likely to be an issue in variability between samples but this effect can be attributed to the stages before the barrier layer is deposited. As water-based cutting fluid is used for grinding and cutting, there is a likelihood that damage is occurring at the surface due to a reaction between the water and magnesium alloy. To explore this observation in more detail, a water free/oil based lubricant is used to process a magnesium silicide puck and an identical barrier layer is deposited. The brazing test is repeated on this sample. Figure 90 and Figure 91 show the cross-sectional SEM images of the gold capped titanium nickel barrier layer on magnesium silicide, which has been processed with oil based cutting fluid.

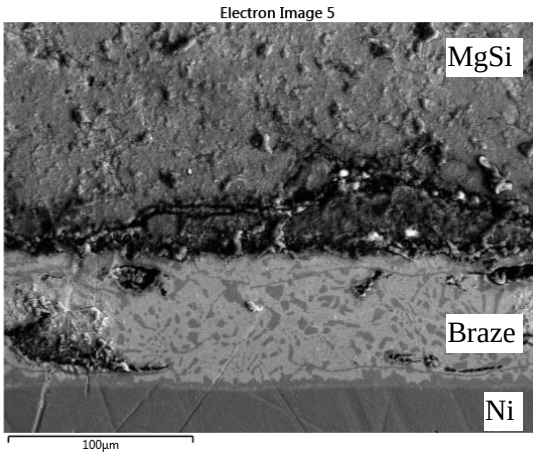

Figure 90. Cross-sectional SEM image of a magnesium silicide sample with a titanium nickel barrier and a gold capping layer. Brazed at 630oC for 10 minutes.

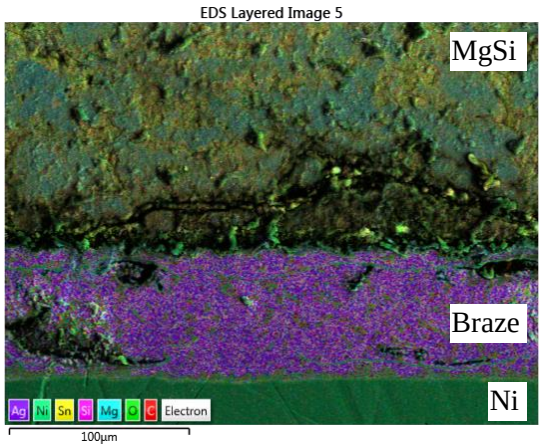

Figure 91. Cross-sectional EDS image of a magnesium silicide sample with a titanium nickel barrier and a gold capping layer. Brazed at 630oC for 10 minutes.

The junction is mostly uniform with some instances of gouges in the bond. Compositional analysis indicates that this is a processing defect during sample polishing for the SEM imaging as there is no sign of diffusion or potassium-containing traces that would represent flux. Cracking is still observed at the magnesium alloy interface, but this is much less severe and frequent along the bond line in comparison to the sample processed with aqueous cutting fluid. The compositional data also indicates that the cracking is unlikely to have arisen from the diffusion of elements and further supports the claim that the cracking is a processing defect that has occurred during the sample preparation for SEM imaging. Thin lateral traces of nickel above each interface in the braze joint can be observed. There are two possible explanations for this occurrence, either the flux is removing a portion of the nickel layer during brazing or there are still adhesion issues with the nickel layer and the titanium layer.

The nickel traces can be seen more clearly in the nickel only signature of the EDS scan in Figure 92. A nickel layer can still be observed at the barrier layer position but it appears to be less defined than the lateral layers of nickel mixed with the braze alloy. The fact that the nickel strips are observed at both interfaces of the braze joint indicates that flux etching is a factor in this occurrence but this is only observed with a gold capping layer on the barrier layer, which indicates that there may still be issues with the adhesion of the sputter coated barrier layer, even with the change in cutting fluid. The sheet resistance of the joint is measured at 1220.00 ± 40.60 $\mu\Omega.cm^2$. This is in the same region as the junction that was processed with aqueous cutting fluid, which implies that the increased resistance of the junction is dominated by other interlayer properties.

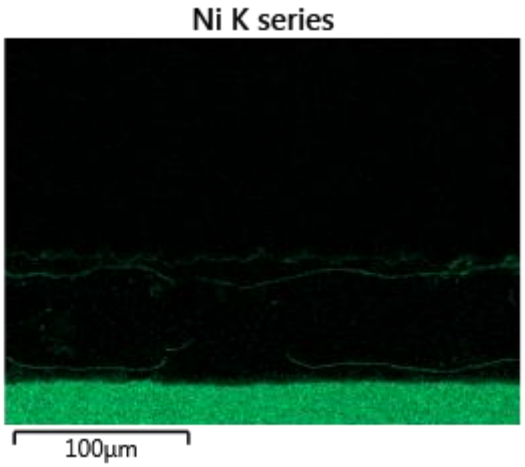

Figure 92. Cross-sectional nickel EDS image of a magnesium silicide sample with a titanium nickel barrier and a gold capping layer. Brazed at 630oC for 10 minutes.

To verify the effect of varying the cutting fluid on the barrier layer adhesion, a sample of each processing method is cross sectioned and analysed without any brazing process performed. Figure 93 shows the sample processed with aqueous cutting fluid and Figure 94 shows the sample processed with non-aqueous cutting fluid.

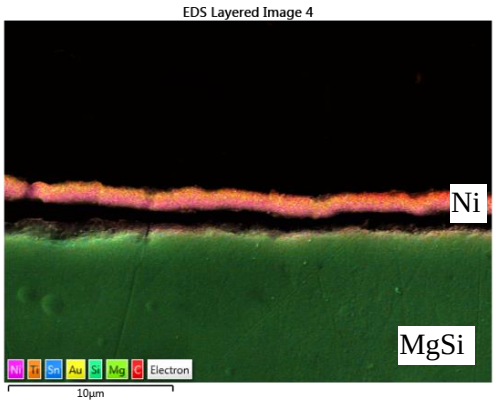

Figure 93. Cross-sectional SEM image of a magnesium silicide sample with a titanium nickel barrier and a gold capping layer, ground and cut using aqueous cutting fluid.

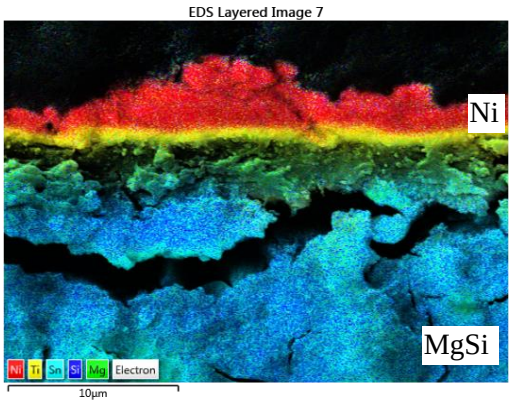

Figure 94. Cross-sectional EDS image of a magnesium silicide sample with a titanium nickel barrier and a gold capping layer, ground and cut using non-aqueous cutting fluid.

Clear differences between the two samples can be observed. The sample preparation process has clearly caused damage to the two samples but the difference in the two failures of the interfaces shows a significant result. A much stronger bond between the titanium seed layer and the magnesium silicide is achieved with the non-aqueous cutting fluid sample. When sheer stress is applied during the sample preparation process, the layer is so strongly attached that failure in the semiconductor material occurs as opposed to complete delamination of the

barrier layer in the sample which is processed with an aqueous based cutting fluid. This indicates that an improvement can be made to the joint properties by using a non-aqueous cutting fluid. As a result, processing of the samples is carried out with non-aqueous cutting fluid.

A repeat of the earlier joining test on magnesium silicide with a titanium adhesion layer and a nickel barrier coating is carried out on a sample that has been processed using non-aqueous cutting fluid.

The cross-sectional images show how the interface between the barrier layer and the magnesium silicide is more uniform and less damage is observed in comparison to samples that are processed with aqueous cutting fluid. In Figure 95, debris is observed as a result of the sample transport; the area imaged shows sufficient data to conclude that less interfacial damage has occurred due to the sample grinding process. This is supported by Figure 96 which shows a defined titanium signature, broken only by overlying debris. The sheet resistance of the bond is measured at 467.00 ± 8.35 $\mu\Omega.cm^2$; this value is the closest result so far to the Toyota material results; with a drop in resistance approaching a factor of 2 in comparison to the aqueous cutting fluid sample. This drop in resistance can be attributed to the surface layers formed when the magnesium alloy is in contact with aqueous solutions. Referring to Figure 70, water causes the formation of $MgCO_3$, $Mg(OH)_2$ and MgO, whereas using non-aqueous lubricants lead to only MgO forming from contact with the atmosphere.

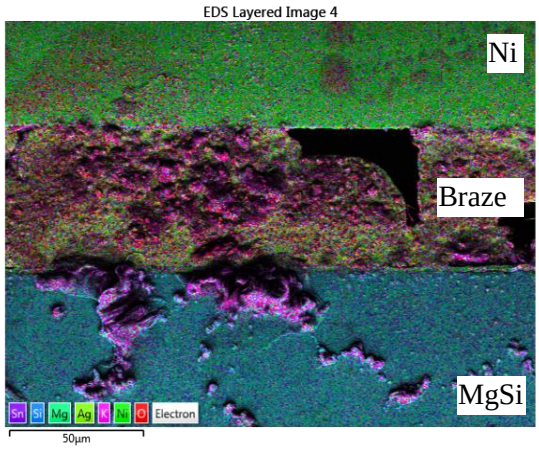

Figure 95. Cross-sectional SEM-EDS image of a magnesium silicide sample with a titanium nickel barrier, ground and cut using non-aqueous cutting fluid. Brazed under argon at 630oC for 10 minutes.

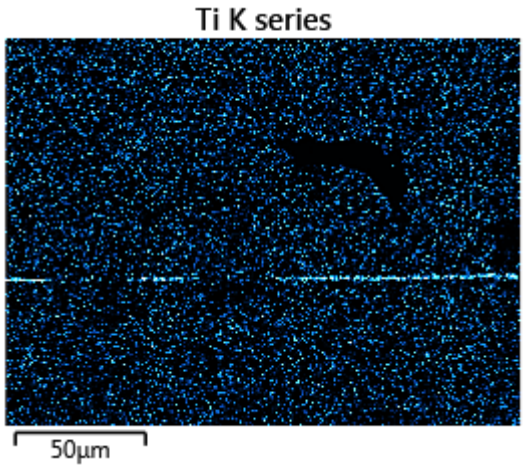

Figure 96. Titanium signature EDS image extracted from data in figure 97, showing distinct titanium layer present on the magnesium alloy surface.

Due to this result, the magnesium silicide and higher manganese silicide samples are now processed with the oil based lubricant during grinding and cutting.

It is necessary to test identical experimental parameters for the higher manganese silicide material to verify the suitability of this process for producing a thermoelectric module.

A HMS sample is ground and diced into pellets using the oil based lubricant. Sputter coating is used to apply 300 nm of titanium as an adhesion layer, 1.2 μm of nickel followed by a 30 nm protective coating of gold. The sample is brazed at 630^{o}C under argon flow using Johnson Matthey silver flo-56 braze paste with a gas pressure of 0.25 Bar.

Figure 97 shows a cross section of the sample; the braze alloy has flowed into the joint evenly, indicating that the processing conditions are suitable for this trial. Three points in the barrier coating show how the damage has occurred leading to a reaction between the brazing alloy and the higher manganese silicide material. The EDS map in Figure 98 indicates that the primary reaction involves copper, manganese and silicon. The braze alloy contains a small fraction of copper which is seen to diffuse out of the braze alloy and across the breaks in the barrier layer. Figure 99 shows the diffusion of copper in more detail. When comparing Figure 99 and Figure 100, it can be deduced that the copper is not reacting with the titanium adhesion layer directly and so the breaks in the layer are likely to be caused by displacement by the copper. This effect may also arise from the quality by which the titanium layer is deposited. If breaks are present in the layer, or thinning occurs at points where the surface roughness of the semiconductor is too high, this can cause weakness or vulnerability to barrier layer breakdown. Nonetheless, the electrical characteristics of the junction are tested to verify if the diffusion causes significant damage to the joint. The average sheet resistance is measured at 17.2 ± 0.55 μΩ.cm^{2}. This is approximately half of the resistance achieved with the corresponding higher manganese silicide produced by Toyota.

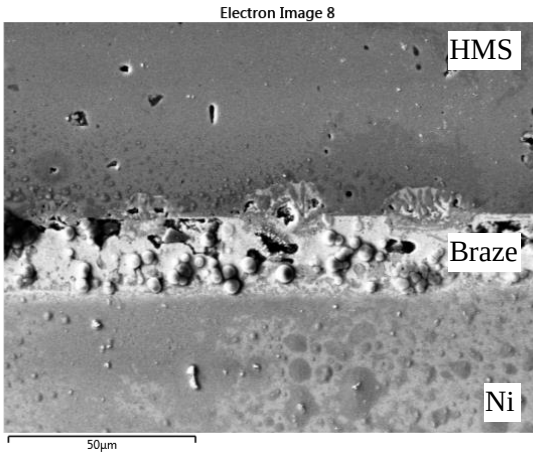

Figure 97. Cross-sectional SEM image of a manganese silicide sample with a titanium/nickel/gold barrier, ground and cut using non-aqueous cutting fluid. Brazed under argon at 630oC for 10 minutes.

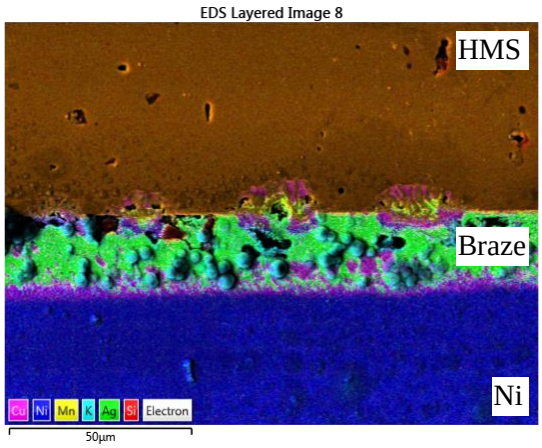

Figure 98. Cross-sectional EDS image of a manganese silicide sample with a titanium/nickel/gold barrier, ground and cut using non-aqueous cutting fluid. Brazed under argon at 630oC for 10 minutes.

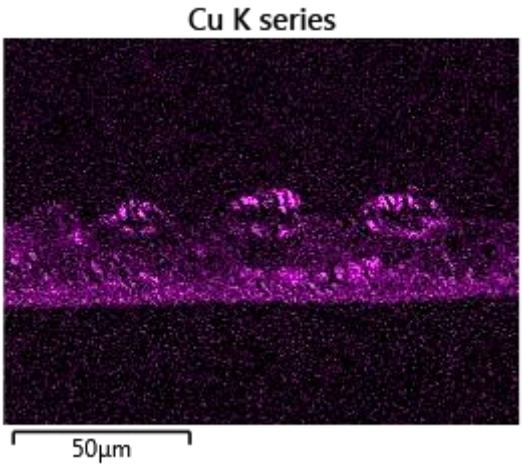

Figure 99. Copper EDS trace extracted from Figure 97.

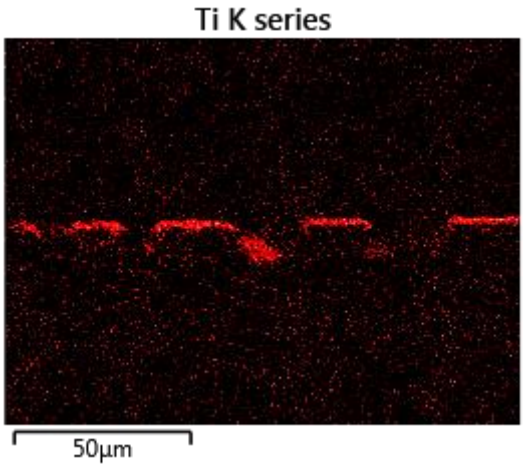

Figure 100. Titanium EDS trace extracted from Figure 97.

Titanium/nickel and titanium/nickel/gold has been tested on magnesium silicide and higher manganese silicide semiconductors for its effectiveness as a barrier coating to protect the material from diffusion and to achieve good electrical and mechanical connections. The layers offer a surface for good mechanical integrity and result in moderate electrical properties for magnesium silicide and exceptional electrical properties for higher manganese silicide. Insufficient data has been collected to deduce that the layers offer a robust diffusion layer as results show that the junctions for the magnesium silicide are expressing signs of the onset of barrier breakdown and diffusion. The higher manganese sample shows how breaks can occur in the barrier layer, allowing diffusion of copper to occur.

Future experiments will be made with this barrier composition and thicknesses will be modified to explore their effect on barrier layer stability. More specifically, the thickness of the titanium layer can be increased to account for surface roughness of the semiconductor. This would reduce the frequency of barrier degradation instances due to thinning of the adhesion layer, as shown in the HMS sample.

It has been shown in some cases; a nickel barrier layer cannot prohibit the diffusion of elements in the interface. As a result, a sample of alloys is tested for their effectiveness as barrier layers. The next section outlines the study on nickel chrome alloy that is deposited using sputter coating. This is an industry standard alloy used for protective coatings of components and is also used as a diffusion barrier in some cases. The addition of chrome increases the toughness of the barrier layer. A mechanically stronger barrier layer is expected to increase diffusion resistance.

4.3.2.3 Ni/Cr Sputter Coated Samples

Focus remains on the magnesium alloy as this represents the more reactive and process dependent of the two semiconductors. A 300 nm titanium adhesion layer is deposited onto a sample of magnesium silicide followed by 1.2 μm of nickel chrome alloy. Brazing samples are made at 630^{o}C under argon flow for 10 minutes with a gas pressure of 0.25 Bar. Figure 101 toFigure 106 show the cross sectional SEM and EDS results for this trial.

The SEM image shows that severe diffusion has occurred during the brazing process. Although a mechanically strong junction is achieved, the result is undesirable as the diffusion is a degenerative reaction that will worsen during operation. If it were to be operated as a thermoelectric device, it is likely that over time mechanical failure and oxidation will occur. This would lead to an increase in contact resistance, thus reducing the efficiency of the thermoelectric device.

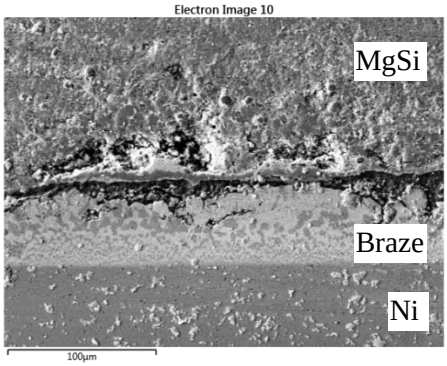

Figure 101. Cross-sectional SEM image of a Mg2Si sample with a titanium/nickel chrome barrier, ground and cut using non-aqueous cutting fluid. Brazed under argon at 630oC for 10 minutes.

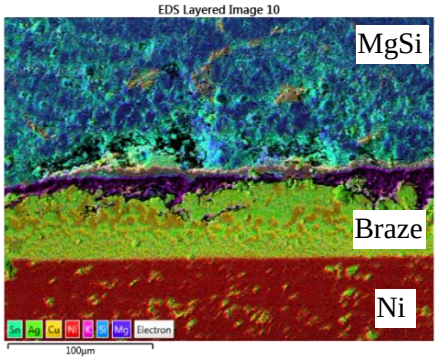

Figure 102. Cross-sectional EDS map of a Mg2Si sample with a titanium/nickel chrome barrier, ground and cut using non-aqueous cutting fluid. Brazed under argon at 630oC for 10 minutes.

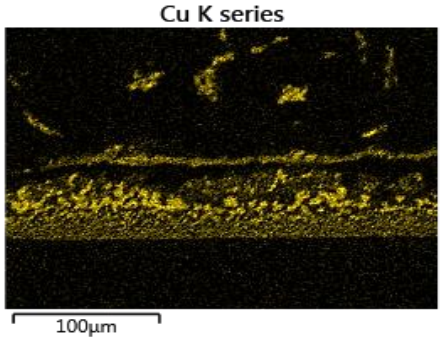

Figure 103. Cross-sectional copper EDS map of a Mg2Si sample with a titanium/nickel chrome barrier, ground and cut using non-aqueous cutting fluid. Brazed under argon at 630oC for 10 minutes.

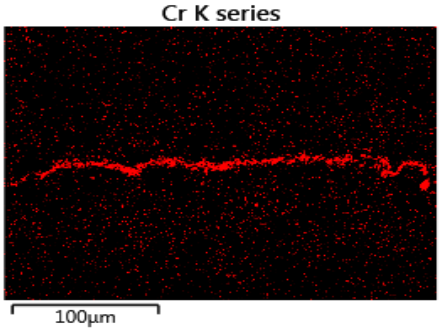

Figure 104. Cross-sectional chrome EDS map of a Mg2Si sample with a titanium/nickel chrome barrier, ground and cut using non-aqueous cutting fluid. Brazed under argon at 630oC for 10 minutes.

There are two gradients of diffusion occurring during the process. The first is the leaching of magnesium from the semiconductor alloy, into the braze layer. shows how the layer has collected beyond the diffusion barrier. Figure 105 shows the magnesium EDS signature in more detail. At the semiconductor interface, the magnesium concentration is reduced, implying that magnesium has leached from the surface layer and this effect does not represent a bulk movement of magnesium. The second diffusion gradient occurs with copper. Figure 103 shows the EDS copper signature for the cross section. The copper has collected at the diffusion barrier and has diffused deep into the semiconductor, forming localised areas of copper. The movement of copper into the semiconductor will significantly alter the thermoelectric properties of the material. Changing the specific dopant levels will cause the material to act more like a metallic conductor and less like a semiconductor. The thermal conductivity will be increased and Seebeck coefficient will be decreased.

Figure 104 shows that the nickel/chrome diffusion barrier is still intact. This indicates that this alloy is not suitable as a diffusion barrier; as diffusion has occurred without any clear breaks in the layer.

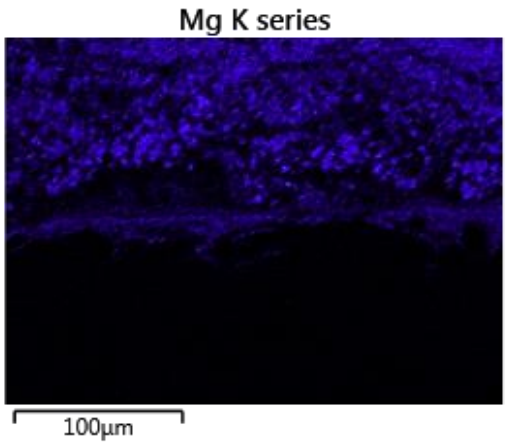

Figure 105. Cross-sectional magnesium EDS map image of a Mg2Si sample with a titanium/nickel chrome barrier, ground and cut using non-aqueous cutting fluid. Brazed under argon at 630oC for 10 minutes.

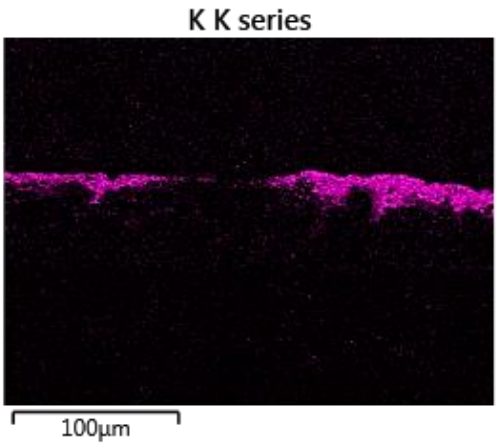

Figure 106. Cross-sectional potassium EDS map image of a Mg2Si sample with a titanium/nickel chrome barrier, ground and cut using non-aqueous cutting fluid. Brazed under argon at 630oC for 10 minutes.

Comparing Figure 105 with Figure 106, the magnesium and potassium signatures align in the braze area. Potassium fluoroborate is a component of the flux which is typically used for brazing, this reduces with an oxide to provide a clean surface for bonding between the braze alloy and the sample. Magnesium will have diffused through the barrier layer and will have reacted with the flux, forming a magnesium-potassium interlayer.

Contact resistance measurements were taken on the sample and an average sheet resistance of $2210.00 \pm 7.02\ \mu\Omega.cm^2$ is calculated for the braze junction.

The role of the flux in the braze paste is to reduce and remove oxide layers and debris, expelling this to the outside of the braze junction by capillary action. As potassium is detected in the braze joint, it may be possible that the flux process has not completed its function. Usually, if flux is still present in a braze joint, the optimal brazing temperature or time has not been achieved. To test this, a sample of the Ti/NiCr coated magnesium silicide is brazed at 650^oC for 10 minutes under argon flow with a gas pressure of 0.25 Bar. The results show that the flux process has completed as potassium is no longer present in the junction, but the magnesium diffusion has continued to the point where the barrier layer is completely broken. Figure 107 shows the element map overlaid on a cross-sectional image of the braze interface.

Comparing Figure 106 to Figure 107, potassium is no longer observed in the joint but the magnesium diffusion has continued. In the case of the samples with a Ti/Ni barrier coating, flux has not been observed in the joint when brazing has been carried out under identical conditions. The nickel chrome barrier layer allows magnesium to diffuse readily and as a result prolongs the flux reaction process. As with the process brazed at 630°C, the sample brazed at 650°C also produces a mechanically strong junction, but the sheet resistance of the interface is increased. An average sheet resistance of 2.78E-3 ± 6.53E-6 Ω.cm^2 is calculated for the braze junction. This represents a 25% increase in resistance over the lower temperature process. Figure 108 shows an EDS map of an untreated pellet of the Ti/NiCr coated magnesium silicide; it shows a well-defined, dense bonded barrier layer on the surface of the semiconductor. As the diffusion cannot be attributed to barrier layer damage or porosity, it can be concluded that this layer is not effective as a protective diffusion barrier for the components present in the magnesium silicide and braze alloy formulation.

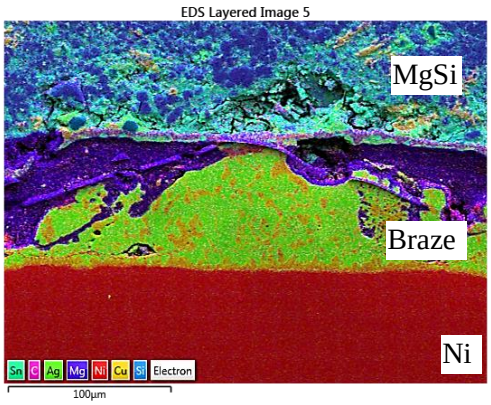

Figure 107. Cross-sectional EDS map signature of Ti/NiCr coated magnesium silicide sample. Brazing at 650oC for 10 minutes under argon flow.

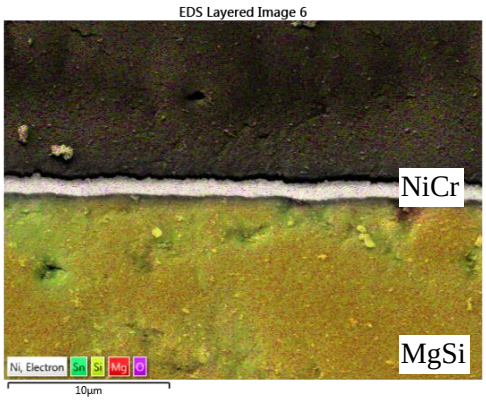

Figure 108. Cross-sectional EDS map signature of an untreated Ti/NiCr coated magnesium silicide sample.

4.3.2.4 TiN Sputter Coated Samples

The next alloy proposed for barrier layer testing is titanium nitride. Titanium nitride (TiN) is a conductive ceramic, most commonly used as a coating on machine tooling to increase hardness. Titanium nitride can be deposited using magnetron sputter coating, but carries more risk as the process needs to be carried out at elevated temperatures for a more effective coating [57]. The coating is applied to the magnesium silicide sample at 300°C in a nitrogen atmosphere and is allowed to cool to ambient temperature before being removed from the inert atmosphere. A 300 nm titanium adhesion layer is deposited followed by a 1.2 µm titanium nitride layer. As titanium nitride is a ceramic, it is expected that the layer will be difficult to braze to; because of this, a second sample is made with a 300 nm titanium

adhesion layer and a 1.2 μm nickel layer on top of the titanium nitride layer. A comparison of the two barrier layers is made by carrying out identical brazing trials.

Both samples are brazed using Johnson Matthey silverflow-56 at 630^{o}C for 10 minutes under argon flow at a gas pressure of 0.25Bar using the small prototype jig displayed in Figure 15. The samples are characterised using 4 point probe resistance measurements. Appendix figure 3 shows the sheet resistance results and bulk material resistivity of the brazed samples.

Particularly high sheet resistances are measured for the two samples. The Ti/TiN sample is measured with an average sheet resistance of 12 $\Omega.cm^2$ and the Ti/TiN/Ti/Ni sample is measured with an average sheet resistance of 46.5 $\Omega.cm^2$. In comparison to the lowest sheet resistance sample which is the Ti/Ni coated sample, the sheet resistance is five orders of magnitude higher. Analysing the pellet resistivity, the readings are the highest in comparison to any other previous sample at between two and three orders of magnitude higher. This may have arisen from the higher temperature processing for titanium nitride sputter deposition, causing nitrogenation in the thermoelectric semiconductor material. Secondly, the increased resistance could arise from oxidation of the material. If oxygen is present at an elevated temperature, the magnesium silicide will degrade rapidly.

When analysing the unicouples from the brazing trials, severe surface degradation can be observed on the semiconductor. Figure 109 shows two unicouples brazed simultaneously; both have severe colour changes on the surface of the semiconductor. This may have arisen from oxygen being present during the brazing process. Although the sample is in a continuous flow of argon gas, a low gas pressure is applied of 0.25 Bar. If the gas flow is too low, a small volume of air may be able to enter the brazing jig chamber and react with the magnesium silicide during when the system is at high temperature. If this occurs, the electrical properties of the semiconductor can be modified. Granting that the sample is polished for 4 point probe resistance measurements, only a thin layer of material is removed to maintain the sample cross-sectional area for measurement accuracy purposes.

Figure 109. Two Ti/TiN brazed unicouples showing surface degradation after processing.

The effect of oxidation can occur deep in the semiconductor material as the oxide layer is not self-passivating, thus explaining the increase in resistivity of the bulk pellets. To test this theory, the experiment is repeated on a sample coated with Ti/TiN/Ti/Ni, but the argon gas pressure is increased to 0.75 Bar. Furthermore, to compare the results of earlier tests; samples of Ti/NiCr and Ti/Ni are additionally brazed under these conditions. The samples are characterised using 4 point probe resistance measurements and the sheet resistance of the contact and bulk pellet resistivity is derived.

The nitride sample shows much-improved resistance results. The contact sheet resistance is measured at 999.00 ± 66.20 $\mu\Omega.cm^2$ and the bulk pellet resistivity is measured at 11.10 $\mu\Omega.m$. In comparison to the untreated bulk resistivity of 5.80 $\mu\Omega.m$, this is a similar increase in internal resistivity to earlier measurements. The Ti/NiCr sample had a contact sheet resistance of 3910.00 ± 16.20 $\mu\Omega.cm^2$ and a bulk pellet resistivity of 75.90 $\mu\Omega.m$. The Ti/Ni sample had a contact sheet resistance of 671.00 ± 7.13 $\mu\Omega.cm^2$ and a bulk pellet resistivity of 14.20 $\mu\Omega.m$. These measured values are in reasonable agreement with the previous results obtained with an argon gas flow pressure of 0.25 Bar. It can be concluded that degradation of the brazing jig has occurred due to usage wear. Graphite will react with oxygen in the atmosphere at high temperatures, producing carbon dioxide. This reduces the density of the jig and makes it more liable to air leakage.

A more robust argon flow jig is designed for testing. Manufactured from stainless steel and welded to a stainless steel argon feed pipe; this design has a better seal to prevent oxygen ingress and degradation after prolonged use. Figure 16 shows an image of the jig. A chamber for prototype module assembly is added to the design. Modification of the brazing profile is carried out due to the difference in thermal conductivity between graphite and stainless steel. Higher tube furnace temperatures have to be applied to reach the brazing temperatures defined with the graphite jig within the 10-minute brazing time. The brazing time could be

increased and the furnace temperature could be maintained, but it is preferable to work with the shortest brazing time possible so that the material is at elevated temperatures for the shortest duration possible.

4.4 Finalised Process

The metallization process for magnesium silicide has been studied in detail. Characterisation data suggests that the most promising process developed so far is by depositing onto the semiconductor using sputter coating. Sputter coating a seed titanium layer of 300 nm has shown to improve adhesion of the barrier layer. A final thick barrier layer of nickel is deposited with a thickness of 1.2 μm. A sheet resistance of 467.00 ± 8.35 $\mu\Omega.cm^2$ is achieved by brazing at 630^{o}C for 10 minutes in a graphite contact resistance jig with an argon flow pressure of 0.25 Bar. The finalised process is described as follows.

- Thermoelectric powders are produced by IntrinsiQ Materials London and are sent to Queen Mary University London.
- Pucks of tin/antimony-doped MgSi and undoped HMS are produced by Spark Plasma Sintering by Queen Mary University of London.
- Pucks are delivered to European Thermodynamics.
- The pucks are ground using a Struers Accuton-50 grinding/cutting machine with a 40 μm diamond size cup wheel to achieve parallel surfaces on the top and bottom faces of the disc. An oil based lubricant is used in this process to reduce material degradation. A 3 mm thickness is achieved in this process.
- The pucks are cleaned using Acetone followed by Isopropanol.
- Pucks are sent to Teer Coatings Ltd for sputter coating.
- A 300 nm Titanium layer is deposited on both faces followed by a 1.2μm nickel barrier layer.
- Samples are returned to ETL for dicing.
- The discs are diced using an Accutom-50 automated grinding/cutting machine with a metal bonded diamond blade. A pellet cross-section of 2.5 mm x 2.5 mm is achieved in this process.
- The pellets undergo an intensive clean in acetone followed by a final wash in isopropanol.
- Metallised ceramics are cleaned using acetone followed by isopropanol.
- Dots of Silverflow-56 brazing paste are deposited onto the copper metal straps of each ceramic substrate in the respective positions of the pellets. The dots have an approximate diameter of 2 mm and height of 1 mm.

- The pellets are assembled onto the hot side ceramic in a checkerboard arrangement by hand. The tack of the braze paste offers sufficient stability of the pellets to stay in position during the assembly process.
- The cold side ceramic is placed on the top of the assembly to complete the series circuit of semiconductor pellets.
- The module assembly is inserted into the chamber of the argon flow jig (figure 38) and the lid is sealed using M3 nuts and bolts. In doing so, an airtight seal is achieved, leaving only the argon gas outlet to allow the flow of the inert gas.
- The Carbolite CTF-900 tube furnace is preheated to 630^{o}C.
- Argon is released from the storage bottle at 0.25 Bar to allow flow across the sample.
- The assembly is inserted into the tube furnace and a timer is started for 10 minutes.
- After 10 minutes, the assembly is removed from the tube furnace and allowed to cool under ambient conditions on a heatproof plate.
- The flow of argon is continued for approximately 30 minutes until the jig is cool to the touch.
- The jig is disassembled and the brazed module is removed from the jig.

The process described offers a repeatable method for module prototyping which can be upscaled using an industrial scale sputter coater, multi-diamond wire dicing machine, automated pick-and-place line technology and a high-temperature inert gas brazing belt furnace.

5. Computational Modelling and Simulation

A model was developed using the joule heating module in COMSOL Multiphysics to assess the matched load power output of a high-temperature thermoelectric module comprised of silicide semiconductor materials.

The model was based on a p-n thermocouple that represents a single unit of a module. As thermoelectric modules are a series arrangement of thermocouples, the computed output of the model can simply be multiplied by the number of thermocouples in the desired module. This offers a quick and powerful method for modelling thermoelectric devices for power generation.

The joule heating module in COMSOL couples heat transfer in solids with electric currents. The model ensures that (thermal) energy and charge are conserved and follows Fourier's law and Ohms law. The Peltier effect is modelled as an additional heat flux shown in equation 6:

$$\boldsymbol{q_{addn}} = -\alpha T \boldsymbol{J} \tag{6}$$

This is added to the model as a domain heat source by calculating the del function of the heat flux shown in equation 7:

$$Q_{addn} = -\nabla . q_{addn} = \nabla . (\alpha T \boldsymbol{J}) = \alpha (\nabla T . \boldsymbol{J}) + T(\nabla \alpha . \boldsymbol{J}) \tag{7}$$

The Seebeck effect is modelled by an additional coefficient on the current density equation whereby equation 8 is formed:

$$\boldsymbol{J_{addn}} = -\alpha \sigma \nabla T \tag{8}$$

This method of modelling is adapted from a study carried out by Jaegle *et al* [29].

The geometry for the model is based on the standard pellet size used in this study. A pellet geometry of 2.5 mm x 2.5 mm x 3 mm, ceramic of 20 mm x 20 mm x 0.7 mm and Copper straps of 2.5 mm x 6 mm x 0.3 mm are modelled. Figure 110 shows the geometry from the model.

A free tetrahedral mesh is used for the model, depicted in Figure 111. Initially, the model was meshed by applying a square mesh on the bottom face and sweeping this throughout the model. This caused increased complexity in the model and as a result, the run-time for the

solver was made much longer. Accuracy of the results was not significantly improved and so the free tetrahedral mesh is chosen for simulating this model.

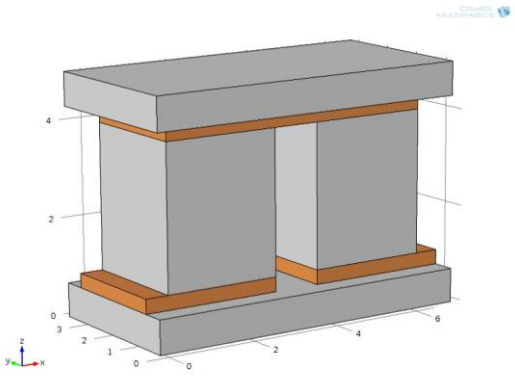

Figure 110.Geometry of COMSOL model, showing top and bottom ceramics, copper straps and TE material pellets.

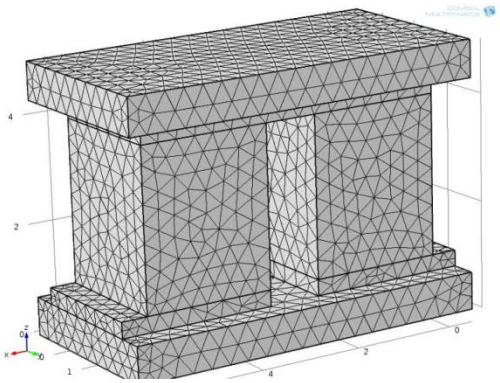

Figure 111. Free tetrahedral mesh of p-n couple used in COMSOL modelling.

Variable properties are assigned to the TE materials from characterisation data, such as Seebeck coefficient, electrical conductivity and thermal conductivity in the form of polynomials. The Peltier effect is modelled using an external current density calculated using the Seebeck coefficient, internal current density and temperature values in each axis. The Seebeck effect that arises from the resultant current is modelled as a heat source using the power density equation (Equation 8) which calculates the pumping power of the device. Electrical and thermal contact impedances are estimated and applied to the relevant interfaces. For reference, a ground terminal is applied to one of the contacts and on the opposing contact, a terminal is applied which is assigned a range of resistances for matched load power testing. A temperature differential is imposed between the top and bottom ceramics to model the device section in operation.

The simulation is executed as a parametric sweep over a range of terminal resistances; for example: 10 micro-Ohms to 300 milli-Ohms in steps of 5 milli-Ohms. The model calculates the thermal and electrical properties for each imposed resistance, and from this the power characteristics can be derived.

A surface average measurement is calculated for voltage and current density at the terminal point. Post processing is carried out using Microsoft Excel. The data is modified to represent a full-scale device. As the device is a series connection of thermocouple units, only the voltage is multiplied by the number of couples required as the current is the same at every point of the module. Using P = IV, the module power is calculated and plotted on a graph along with the I-V characteristics of the module.

5.1 Toyota Material Module Modelling

The COMSOL model is used to predict the expected output of the device. Material data supplied by Toyota is entered into the model and values of other components of the model are taken from the COMSOL material library. A contact resistance of 8.58 $\mu\Omega.cm^2$ is used for the magnesium silicide contact and 13.30 $\mu\Omega.cm^2$ is used for the higher manganese silicide contact.

Input values representative of the testing equipment available are used for the model. The temperature differential is chosen to be between 318°C and 18°C meaning a 300°C delta T is imposed.

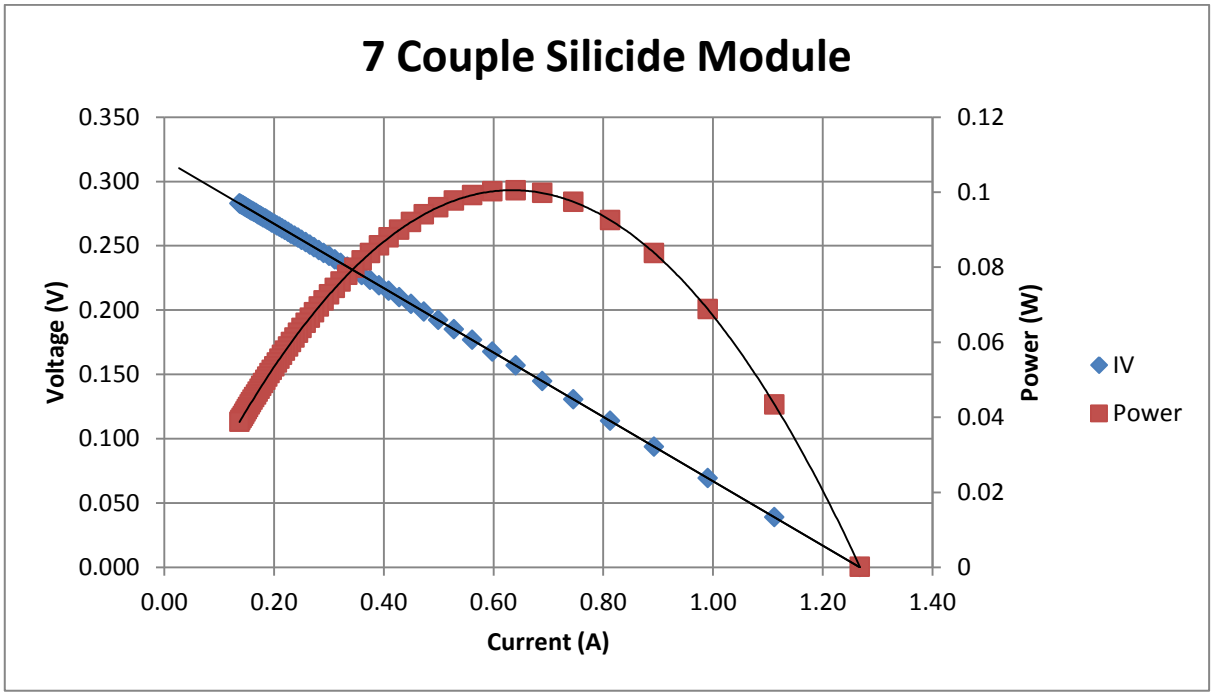

Figure 112 shows the predicted performance data for a 7-couple device.

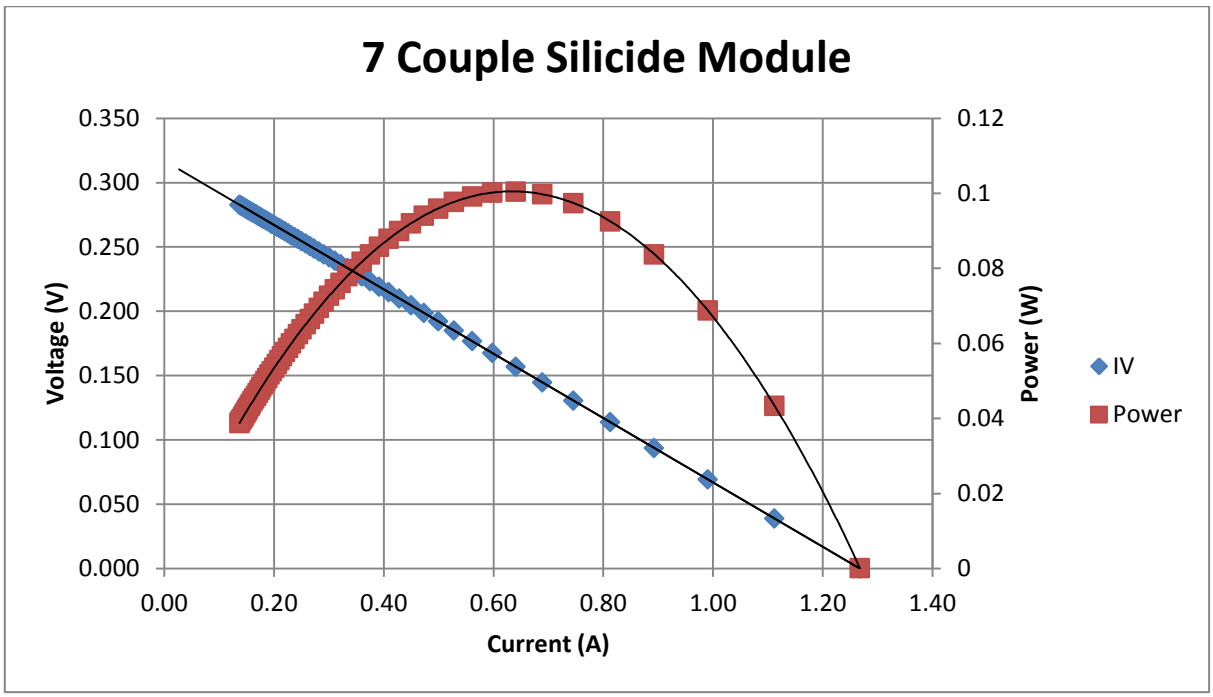

Figure 112. COMSOL model output after modification in Excel, showing I-V characteristics and derived Power output for the device.

From the simulation results, maximum power output is calculated to be approximately 100 mW at 160 mV and 0.65 A. This indicates a module resistance of approximately 250 mOhms when under operation and a module power density of 113.30 mW/cm^2 for a temperature difference of 300^{o}C.

Referring back to Section 4.2.4, the maximum power output for the 7-couple prototype module was measured at 115 mW (175 mV and 650 mA). The peak power operating data indicated that the maximum power point occurs at approximately 270 mOhms. Finally, the power density is calculated at 130.29 mW/cm^2 for a temperature difference of 300^{o}C.

Comparing the simulation results to the measured results, it shows the similarity between the COMSOL result and the experimental result. The COMSOL model slightly under predicts the power output which could possibly be attributed to the fact that the model overestimates the thermal contact resistance between the ceramic surfaces and heater/cooler plates, indicated by the lower voltage calculation which is directly proportional to temperature differential. Nonetheless, the simulated results and experimental data are in reasonable agreement with each other and so simulations with this model can be done with confidence for other materials.

5.2 QMUL/IML Material Module Modelling

Due to time constraints, a prototype module for the QMUL/IML material was not assembled. However, for comparison, COMSOL modelling is carried out using the material parameters for the MgSnSbSi and HMS provided by QMUL. A contact resistance of 467.00 ± 8.35 μΩ.cm^2 is applied to the model and the following expected output characteristics are displayed in Figure 113.

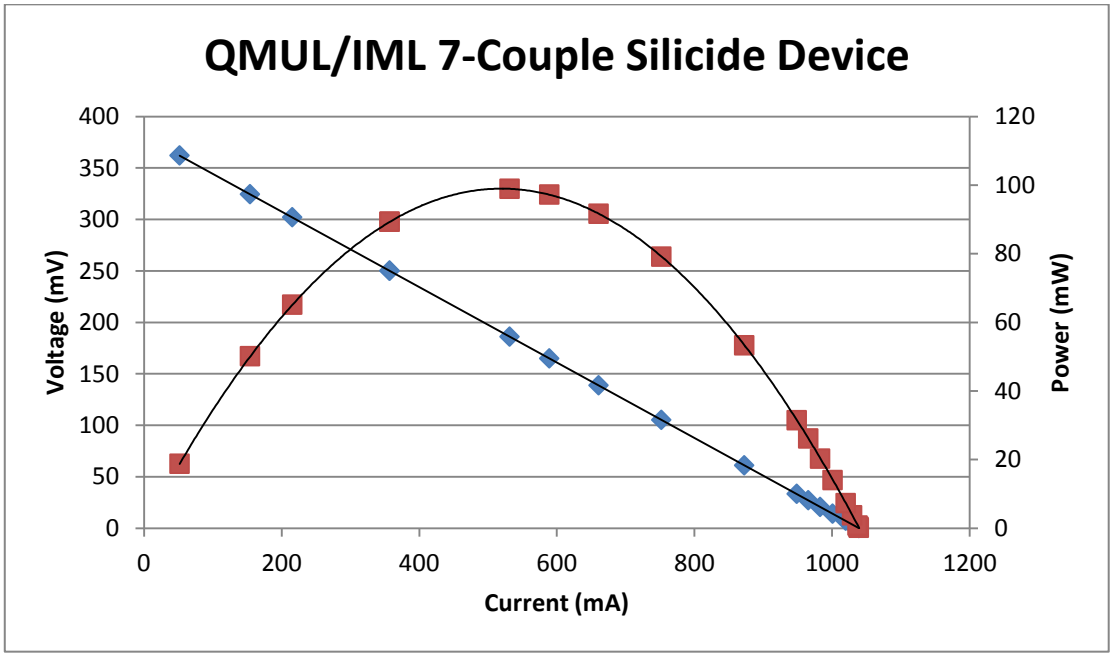

Figure 113. Graphical representation of COMSOL model output data for a 7-couple module assembled using silicide material provided by QMUL/IML using the final module assembly process defined in Section 7.2.

A 300oC temperature differential is simulated with a cold side of 18^{o}C and hot side at 318^{o}C, replicating conditions of the simulation for the Toyota material module. The peak power output is calculated at 99 mW with a voltage of 186 mV and current of 531 mA. With the module operating at peak power output, the power density is approximated at 113 mW/cm^2. The model is shown in section 7.1.3 to under-predict the output power by a factor of 1.15. With this factored in, an expected corrected power output of 114mW with a power factor of 130 mW/cm^2 would be achieved.

Finally, the aim was to replicate the results of the Toyota module system. The lowest sheet resistance achieved was 467.00 ± 8.35 μΩ.cm^{2,} which is two orders higher in comparison to the Toyota material. A sheet resistivity of 5.13 ± 0.55 μΩ.cm^2 is measured for the Toyota material. The following COMSOL model shows a simulation using a sheet resistivity of 5 μΩ.cm^2 with the state of the art material provided by QMUL/IML.

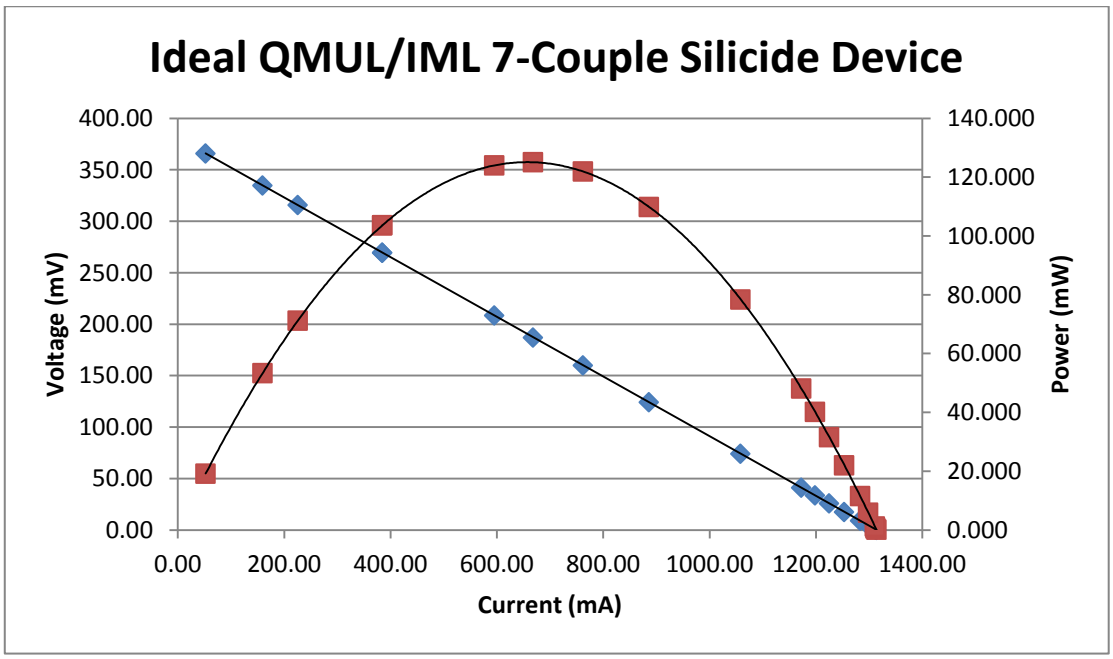

Figure 114. Graphical representation of COMSOL model output data for an ideal 7-couple module assembled using silicide material provided by QMUL/IML using the final module assembly process defined in Section 7.2.

Figure 114 displays the expected output for a module assembled with the QMUL/IML silicide material if a contact resistance comparable to the value achieved for the Toyota material was achieved. A maximum output of 125 mW is calculated at a voltage of 187 mV and a current of 668 mA. This equates to a power factor of 143 mW/cm^2. With the correction factor of 1.15 applied, the maximum power would be expected to be 144 mW and the power factor would be estimated at 163 mW/cm^2.

6. Synoptic Discussion

The aims of the study, outlined in Section 1.4, are discussed in this chapter and the success of the tasks is evaluated. The discussion is split into four sections, each covering a single aim.

6.1 Establishing a Lab Scale Thermoelectric Prototyping Facility

In the first phase of this study, a lab-scale prototyping facility is developed. The facility incorporates the necessary stages for development of modules with specific attention on thermoelectric joining technology.

The first stage involves thermoelectric material processing. A Struers Accutom-50 automated grinding and cutting machine is specified for this stage. It incorporates two important processes in the material preparation stage. Grinding is necessary to remove surface oxides and debris. Furthermore, the semiconductor discs must be of the same height/thickness across both surfaces. This ensures that when pellets are made from the material, they are all of the same height; a crucial factor in module manufacture. The second function is automated cutting of the thermoelectric material. A diamond blade is used as the materials are particularly hard but brittle. The equipment is effective for processing at lab scale as a thin blade can be used to maximise the yield of the material. As the equipment is automated, the grinding and cutting stages are low in labour intensity. The equipment can run with an oil based lubricant that protects water sensitive materials during processing.

Basic lab scale cleaning equipment is used for maintaining sample condition throughout the process. This includes; glassware, solvents and sonication equipment. As the water reactivity of the n-type semiconductor is found to be an issue when joining, de-ionised water is not used in the cleaning stages. Acetone is used for aggressive de-greasing, this solvent leaves residues so a final clean with isopropanol is always carried out.

A Carbolite CTF tube furnace is specified for the joining trial and module brazing stage. Two designs for atmosphere control during the process are explored. The first design is aimed toward small-scale lab production of thermoelectric devices. An Inconel tube, sized to fit into the tube furnace heating zone, is sourced with one end closed and the other is open for fitment of a flange system. A flange system is attached which incorporates a thermocouple and NV25 vacuum fitting is located at the open end. This system forms an effective seal for the evacuation of the chamber, while maintaining sufficient access for insertion and removal of samples. A vacuum tube attaches the tube to an Edwards RV3 vacuum pump. Before the

connection to the pump, an inert atmosphere feed and pressure monitoring equipment is located. This setup offers the maximum area possible for brazing using the tube furnace with a vacuum or inert atmosphere. Although this equipment is very effective for batch module prototyping, it is not suitable for lab-scale joining trials; this is because the process of heating and cooling of the tube is significantly long. For small scale joining trials, an inert gas flow jig is designed. Initially, the jig is formed from two graphite blocks. It is later found that degradation occurs from repetitive use and so the jig is replaced with a stainless steel version. This design offers a quicker process for small scale joining trials as the time taken for setup; heating and cooling is greatly reduced. The jig assembly process is simple and so sample insertion is easy to perform and due to its size the thermal mass means heating and cooling time is significantly reduced in comparison to the Inconel tube equipment. The jig comprises a stainless steel gas feed tube that is attached to the body in which the sample is encapsulated. The jig body has a chamber for a 7-couple module assembly and two narrow chambers for unicouple production. The significance of having two unicouple chambers is twofold. Firstly, the symmetry of the jig promotes an even flow of gas across samples anywhere in the jig. Secondly, two samples can be tested under identical conditions; this enables accurate comparison of brazing fillers or separate samples for characterization i.e. one for SEM characterization and one for contact resistance measurements. The unicouple channels have M3 screws that apply pressure during the brazing process. This is necessary as the samples are arranged horizontally and so gravitational pressure cannot be used for bond line minimization. The two assemblies are effective for their respective applications.

The design of the inert gas brazing jig is such that semiconductor pellet positioning is not necessary when prototyping due to the small sample dimensions. However, for the Inconel tube assembly, pellet arrangement jigs are necessary. The jigs designed are based on a one step brazing process. This means that jig design is more complicated in comparison to a single step joining process, such as the jigs used for industrial module manufacture (see Figure 11). The most effective jig was the wire based design (Figure 13). A smaller pitch can be achieved with this design in comparison to the comb design. The comb design is limited by the manufacturers' minimum accuracy achievable. Although the wire jig has a longer preparation time, more success has been achieved when removing the module from the jig. An example of a module manufactured using this approach can be seen in figure 50.

Bespoke characterization equipment is used in this study that offers accurate measurements for verification of samples. The Seebeck measurement equipment is built in this project and is based on a design for equipment developed at Cardiff University by Dr.G.Min and Dr.D.Rowe. The equipment is calibrated using stock reference samples of commercial bismuth telluride and is co-verified using the equipment located at Cardiff University. Although this equipment is not used in this study, it offers an effective method for quick

measurements of samples to assess material degradation during a brazing trial. Similar characteristics are measured using the four-point probe resistance measurement equipment, from which bulk resistivity can be calculated. This data can be used to assess material degradation from the brazing process and is used in this study.

The four-point probe resistance measurement equipment is built in this project but the equipment assembly is lead by Dr.R.Tuley of European Thermodynamics. This equipment is essential for the characterisation of joining trials and as part of a thermoelectric prototyping lab. Finally, the module characterization equipment, developed by the University of Glasgow is used for testing maximum power output of modules under a temperature gradient. This too is an essential piece of equipment for a thermoelectric development lab.

In summary, this phase of the study is successful as an efficient thermoelectric research facility has been developed. The facility offers the capability for fundamental joining technology and lab scale batch production using different variations of equipment.

6.2 Development of a Joining Process for Silicide Materials and Prototype Devices

The second phase of this study is to develop a joining process for achieving low resistance contacts on high performance tin-antimony doped magnesium silicide and undoped higher manganese silicide, in a process that is scalable and cost-effective for industrial scale supply. Preliminary studies are carried out to verify suitable joining mediums. Screen printing inks and braze alloys in solid and paste form are screened for effectiveness. The screen printing inks hold promise as the joining principle is less aggressive in comparison to a fluxed brazing process. The inks contained metallic-conductive particles suspended in a glass frit matrix. The glass frit melts and the solvent evaporates, leaving a solid glass matrix which is made conductive by the metallic powder. This process is the most successful for initial trials but is not pursued as should a low resistance joint be achieved, the mechanical integrity of the junction would be questionable. As the joint would have the mechanical characteristics, it would not be suitable for a system that is subject to thermal shock and high mechanical stresses. The silver braze alloy category is identified as the most promising group of filler metals for this category. With the requirement that brazing should be carried out below a temperature under 650^{o}C, a specific composition of Silver-Copper-Tin-Zinc is identified for this range. Johnson Matthey Silverflow-56 meets this requirement owing to the brazing range beginning from 630^{o}C and its availability in a paste form. The paste form is preferred as it offers a more scalable route for future upscale in comparison to the solid variety. This paste can be dispensed using screen printing or by a pick-and-place assembly machine. Ease of

assembly is also taken into account. The 'tack' of the paste reduces the need for an effective pellet positioning jig.

The joining approach is first applied to the Toyota supplied material. The material is pre-contacted with a nickel barrier layer by co-sintering. This approach is not scalable as the approach leads to large material losses when achieving parallel faces on the sintered pucks. It would also introduce a larger tolerance in the performance of modules as a consistent depth of the nickel is difficult to achieve. As a result, this leads to an effective variation in pellet height across pellets formed from a disc of co-sintered material. However, the material offers an effective baseline experiment for the validation of the brazing process. Joining trials are carried out and samples are characterised. A contact sheet resistance of 5.13 ± 0.55 $\mu\Omega.cm^2$ is measured for the n-type semiconductor and 32.70 ± 0.95 $\mu\Omega.cm^2$ is measured for the p-type semiconductor. JM Silverflow-56 is used as the filler alloy and the assembly is brazed under argon flow for 10 minutes at 630^{o}C. Although, a lower contact resistance is achieved for n-type material brazed at 650^{o}C, the lower temperature process is chosen as it is suitable for the QMUL/IML material that has a maximum recommended temperature of 650^{o}C.

The sheet resistances cited in the paper by H.S.Kim *et al.* of $4.8x10^{-6}$ $\Omega.cm^2$ for the n-type semiconductor and 3.2 $\mu\Omega.cm^2$ for the p-type semiconductor are comparable to the results achieved with the Toyota material [46]. The n-type Toyota material has a contact resistance very close to the cited literature value but the p-type material is an order of magnitude higher in comparison. The cause of the higher sheet resistance value measured in the p-type material is likely to have arisen from the reaction at the interface; this can be observed in figure 64. Diffusion of silver has occurred which is expected to cause a thin electrically resistive layer in the interface.

A 7-couple prototype module is then assembled and brazed for 10 minutes in the argon flow prototyping jig at a temperature of 630^{o}C. The device is characterised in the module test rig and a peak output power of 115mW is recorded for a 300^{o}C temperature differential. This equates to a power density of 130.29 mW/cm^2.

Various prototype devices are characterised in the study carried out by a group from Fraunhofer IPM. The pellet size (5 mm x 5 mm x 3 mm) used in the study is very large in comparison to the dimensions used for this study (2.5 mm x 2.5 mm x 3 mm). Based on volume of material (Fraunhofer IPM = 3.0 cm^3, Toyota = 2.6 cm^3), the most comparable module is the 2-couple devices tested which yielded a power density of 100 mW/cm^2[56] for a 531K temperature differential. The material compositions and performances differ between the Toyota and Fraunhofer materials; the Toyota material has a ZT approximately twice as high as the Fraunhofer material for both materials. A similar power factor is measured with a temperature differential that is 231^{o}C lower. However, the comparable power density increase

of 30% can be attributed to the higher thermoelectric performance of the material. It is expected that similar contact resistances are achieved between the two studies.

Attention is then turned to the development of a scalable process for depositing a barrier layer onto the higher performance silicide materials provided by IML and QMUL. Research is focussed on barrier layer formation on the n-type tin-antimony doped magnesium silicide. This semiconductor alloy is considerably more reactive in comparison to undoped higher manganese silicide and antimony doped magnesium silicide. This is attributed to the magnesium content and amplification of reactivity with the inclusion of tin.

Electrolytic and electroless deposition of nickel is explored first as it represents a method that is greatly suited to upscaling of manufacture for industrial supply. Characterisation results of deposition trials show that electrolytic and electroless methods are not suitable for barrier layer formation with commercially available formulations. A reaction occurs at the surface of the magnesium alloy, resulting in etching and oxidation of the semiconductor alloy. The plating solutions are aqueous based and so a natural oxidation reaction occurs between the magnesium and water molecules. Furthermore, due to the acidity of the plating solutions, reduction of the salts at the interface causes etching to occur. A method using fluoride based pre-treatment stages may be suitable for this process, but the use of which would require significant investment in material handling infrastructure. As a result, the continuation of plating trials was stopped as it became out of scope for this study with respect to safety and scalability of the proposed process.

Between co-sintering and electroplating, sputter coating represents a compromise for commercial upscale. A variety of sputter layers are explored and the effect of a titanium adhesion layer on barrier coating performance is verified. 1.2 μm sputter coated layers of nickel, nickel-chrome and titanium nitride are deposited onto tin-antimony doped magnesium silicide and brazing trials are carried out on the subsequent samples.

Characterisation data indicates that in terms of stability and contact performance, a 300 nm titanium adhesion layer, followed by a 1.2 μm nickel barrier layer offers the highest performance. Delamination of a 1 μm nickel barrier with no adhesion layer occurs after brazing trials. Although minimal diffusion occurs at the interface, the poor mechanical connection causes a high resistance layer in the joint. Poor barrier layer properties are observed with nickel-chrome and titanium nitride. Cross-sectional scanning electron microscopy results and electron diffraction spectroscopy indicates that magnesium and silver can readily diffuse through the layers. The contact resistances range between 1-4 $m\Omega.cm^2$ for the NiCr and TiN on average. In comparison to the bulk semiconductor material, the resistance of the contacts would represent a large portion of a modules resistance should these layers be used to produce a thermoelectric device.

The samples with a 300 nm titanium adhesion layer and 1.2 μm nickel barrier layer have a contact sheet resistance of approximately 0.5-0.6 $m\Omega.cm^2$ after brazing for 10 minutes under argon flow at 630^oC. This represents the lowest contact sheet resistance achieved in this study for the tin-antimony doped magnesium silicide. Cross-sectional EDS mapping indicates that severe diffusion does not occur, although when raising the brazing process to 650^oC, severe diffusion occurs. This indicates that the suboptimal sheet resistance for the lower brazing result may arise from the onset of diffusion occurring which can not be detected at that point by EDS mapping or cross-sectional imaging. No improvement in contact quality is observed with a gold capping layer. It was expected that an oxide layer was forming on the nickel barrier layer due to the samples being exposed to air. As a result, when brazing, the flux would actively remove the oxide layer, thus etching the barrier layer away, enabling diffusion to occur. In comparison to literature values for the less reactive antimony doped magnesium silicide, the contact sheet resistance is two orders of magnitude higher [46]. To improve the joining quality, the nickel layer thickness could be increased. The Toyota material barrier layer is measured at approximately 20μm thickness; this thickness is not viable for sputter coating but layers of up to 5μm can be tested for the improvement of joint quality.

A 300nm titanium adhesion layer followed by a 1.2 μm nickel barrier layer is tested on the undoped higher manganese silicide. Minor barrier layer breakdown is observed when brazing is carried out at 630^oC for 10 minutes under argon flow. It is unclear if the diffusion is due to barrier layer quality or if the layer is not suitable for the HMS material. The diffusion is uni-directional as copper is only observed past the barrier layer in the HMS. The copper in the alloy during the brazing process forms a layer at the interface for improved bond strength. If the barrier layer is broken in places, copper will diffuse into the next stable layer to improve adherence of the joint. Nonetheless, a sheet resistance of $17.00 \pm 0.13\ \mu\Omega.cm^2$ is measured for this junction. In comparison to the literature reference value, the resistance is five times higher [46]. Improvement of this value is still necessary which may be achieved using thicker nickel sputter layers.

6.3 COMSOL Modelling and Simulation

Due to time constraints, a prototype module comprising the high performance tin dope magnesium silicide is not made in this study. However, a COMSOL model is developed and verified in this study using results from the Toyota material study. The model is used to predict the expected output of a module assembled using the n and p-type QMUL/IML material with a 300 nm titanium adhesion layer and a 1.2 μm nickel barrier layer, using the characterisation data for the material and joining trials. An expected module output of 99 mW

is calculated, equating to a power density of approximately 113 mW/cm^2. Comparing to the Fraunhofer result, a similar power factor is achieved for a lower temperature differential at 300^{o}C. A COMSOL simulation is carried out with ideal contact resistance values which indicate that a maximum output of 125mW can be achieved at a voltage of 187 mV and a current of 668 mA. This equates to a power factor of 143 mW/cm^2 for deal joining parameters. The reduction in power output clearly arises from the onset of diffusion occurring in the braze interface. Improvement of the barrier layer can lead to a significantly more efficient device by incorporating higher performance materials, however with increasing dopant levels, the joining process becomes more complex.

7. Conclusions

Progress has been made in achieving ohmic contacts for high-performance tin-antimony doped magnesium silicide and higher manganese silicide. A lab scale prototyping and characterization facility has been designed and tested. Furthermore, a COMSOL model has been developed for module prototyping verification and has been validated using empirical data.

A lab scale research facility has been designed and implemented at European Thermodynamics Ltd. The facility is shown to function effectively as a thermoelectric research lab. Furthermore, the functional design of the equipment means that the lab can also work as a small-scale batch production facility; able to braze multiple modules under a vacuum or inert gas atmospheres. Automatic sample preparation equipment is used to minimise the labour intensive material processing stages and reduce tolerances in crucial thermoelectric pellet dimensions.

Using the lab scale research facility, a prototype thermoelectric generator is assembled using lower performance material. Comparable results to literature values are achieved for performance characteristics of the module. Progress is made in improving the contact properties of the higher performance tin-antimony doped magnesium silicide material using a sputter coating process. Although poor contact resistance values are achieved in comparison to literature results, a module made with the current process would outperform the modules produced by other groups. This is verified using a COMSOL model that is developed and verified in this study.

8. Future Work

For continuation of the study, it is necessary to improve the contact resistance of the high-performance tin-antimony doped magnesium silicide by two orders of magnitude. Barrier layer breakdown in the less reactive higher manganese silicide must be addressed. Thicker nickel barrier layers will be tested up to a thickness of 5μm by sputter coating and will be verified by joining trials. A 7-couple prototype device will be assembled comprising the high perfomance tin doped magnesium silicide and higher manganese silicide for comparison between each improvement of the joining trials.

Improvement of the COMSOL model will be made by incorporating more parameters to improve accuracy. Empirical data will be used to further improve the model, with the aim to achieve accurate module performance calculations with minimal errors in the results.

9. References

[1] https://upload.wikimedia.org/wikipedia/commons/thumb/8/8b/Thermoelectric_Generator_Diagram.svg/220pxThermoelectric_Generator_Diagram.svg.png. *Schematic of a basic Thermocouple.*

[2] W. Liu *et al.*, "Enhanced thermoelectric properties of n-type Mg2.16(Si0.4Sn0.6)1-ySby due to nano-sized Sn-rich precipitates and an optimized electron concentration," *Journal of Materials Chemistry*, 10.1039/C2JM31919E vol. 22, no. 27, pp. 13653-13661, 2012.

[3] V. K. Zaitsev *et al.*, "Highly effective Mg_{2}Si_{1−x}Sn_{x} thermoelectrics," *Physical Review B,* vol. 74, no. 4, p. 045207, 2006.

[4] B. Poudel *et al.*, "High-Thermoelectric Performance of Nanostructured Bismuth Antimony Telluride Bulk Alloys," *Science*, vol. 320, no. 5876, pp. 634-638, 2008.

[5] K. R. Tarantik *et al.*, "Thermoelectric Modules Based on Silicides – Development and Characterization," *Materials Today: Proceedings,* vol. 2, no. 2, pp. 588-595, // 2015.

[6] T. Hungría, J. Galy, and A. Castro, "Spark Plasma Sintering as a Useful Technique to the Nanostructuration of Piezo-Ferroelectric Materials," *Advanced Engineering Materials,* vol. 11, no. 8, pp. 615-631, 2009.

[7] D. M. G. Kanatzidis, "The Best Thermoelectric Materials," in *Dr. M G Kanatzidis Research Group*, D. M. G. Kanatzidis, Ed., ed: National Science Foundation, Northwestern University, 2009.

[8] W. Werdecker, "Aluminum Nitride-An Alternative Ceramic Substrate for High Power Applications in Microcircuits," ed. IEEE Transactions on Components, Hybrids, and Manufacturing Technology (Volume: 7, Issue: 4, Dec 1984), 1984.

[9] M. Fukuhara, "Physical Properties and Cutting Performance of Silicon Nitride Ceramic," K. Fukazawa, Ed., ed. Ware Elseiver, 1985.

[10] D.M.Rowe, *Thermoelcterics Handbook: Macro to Nano. Introduction.* 2006.

[11] http://www.europeanthermodynamics.com/products/thermoelectric-modules/peltier-generator.

[12] S. Quoilin, "The Organic Rankine Cycle: Thermodynamics, Applications and Optimization," V. Lemort, Ed., ed. Encyclopedia of Life Support Systems (EOLSS), 2011.

[13] D. M. K. *e. al*, "Why the UK Should Invest in Thermoelectrics & the Role of Nanotechnology - a Position Paper," ed. NanoKTN: NanoKTN, 2012.

[14] K. F. Hirokuni Hachiuma, "Activities and Future Vision of Komatsu Thermo modules," ed. European Conference on Thermoelectrics 2007: Conference Proceedings, 2007.
[15] R. M. R. a. R.Studd, "CRC Handbook of Thermoelectrics," ed: CRC, 1995, p. 641
[16] E. K. T.Kacsich, J.P.Fleurial, T.Caillat and M-A Nicolet, "Films of Ni–7 at% V, Pd, Pt and Ta–Si–N as diffusion barriers for copper on Bi2Te3," ed. J. Phys. D: Appl. Phys. 31, 1998, pp. 2406–2411.
[17] S. Bell, *A beginner's guide to uncertainty of measurement*. National Physical Laboratory, 1999.
[18] Mitutoyo.Corp.Available:http://www.msi-viking.com/assets/images/downloads/productspecsheets/MitutoyoSpecSheets/500%20Series%20Absolute%20Coolant%20Proof%20Calipers-IP67.pdf
[19] K.T.Inc.Available:http://www.tek.com/sites/tek.com/files/media/media/resources/Ser2400.pdf
[20] S. B. Riffat and X. Ma, "Thermoelectrics: a review of present and potential applications," *Applied Thermal Engineering*, vol. 23, no. 8, pp. 913-935, 6// 2003.
[21] S. K. M. a. S. S. a. O. Jepsen, "Electronic structure and thermoelectric properties of bismuth telluride and bismuth selenide," *Journal of Physics: Condensed Matter*, vol. 9, no. 2, p. 461, 1997.
[22] L.-D. Zhao, B.-P. Zhang, W.-S. Liu, and J.-F. Li, "Effect of mixed grain sizes on thermoelectric performance of Bi2Te3 compound," *Journal of Applied Physics*, vol. 105, no. 2, p. 023704, 2009.
[23] E. Guilmeau, Y. Bréard, and A. Maignan, "Transport and thermoelectric properties in Copper intercalated TiS2 chalcogenide," *Applied Physics Letters*, vol. 99, no. 5, p. 052107, 2011.
[24] O. Yamashita and S. Tomiyoshi, "High performance n-type bismuth telluride with highly stable thermoelectric figure of merit," *Journal of Applied Physics*, vol. 95, no. 11, pp. 6277-6283, 2004.
[25] P. C. K. Vesborg and T. F. Jaramillo, "Addressing the terawatt challenge: scalability in the supply of chemical elements for renewable energy," *RSC Advances*, 10.1039/C2RA20839C vol. 2, no. 21, pp. 7933-7947, 2012.
[26] H. Ning *et al.*, "Enhanced thermoelectric performance of porous magnesium tin silicide prepared using pressure-less spark plasma sintering," *Journal of Materials Chemistry A*, 10.1039/C5TA03473F vol. 3, no. 33, pp. 17426-17432, 2015.
[27] D. Teweldebrhan, V. Goyal, M. Rahman, and A. A. Balandin, "Atomically-thin crystalline films and ribbons of bismuth telluride," *Applied Physics Letters*, vol. 96, no. 5, p. 053107, 2010.
[28] H. R. Williams *et al.*, "Spark plasma sintered bismuth telluride-based thermoelectric materials incorporating dispersed boron

carbide," *Journal of Alloys and Compounds*, vol. 626, pp. 368-374, 3/25/ 2015.
[29] M. Saleemi, M. S. Toprak, S. Li, M. Johnsson, and M. Muhammed, "Synthesis, processing, and thermoelectric properties of bulk nanostructured bismuth telluride (Bi2Te3)," *Journal of Materials Chemistry*, vol. 22, no. 2, pp. 725-730, 2012.
[30] A. M. M.Rull-Bravo, J.F.Fernandez and M.Martin-Gonzalez, "Skutterudites as Thermoelectric Materials: Revisited," vol. 5, ed. RSC: Advances, 2015, pp. 41653-41667.
[31] B. C. Sales, D. Mandrus, B. C. Chakoumakos, V. Keppens, and J. R. Thompson, "Filled skutterudite antimonides: Electron crystals and phonon glasses," *Physical Review B*, vol. 56, no. 23, pp. 15081-15089, 1997.
[32] G. S. Nolas, M. Kaeser, R. T. Littleton Iv, and T. M. Tritt, "High figure of merit in partially filled ytterbium skutterudite materials," *Applied Physics Letters*, vol. 77, no. 12, pp. 1855-1857, 2000.
[33] A. W. Wenjie Xie, Xinfeng Tang, Qingjie Zhang, Joseph Poon and and T. M. Tritt, "Recent Advances in Nanostructured Thermoelectric Half-Heusler Compounds," vol. 2, ed. Nanomaterials: MDPI, 2012, pp. 379-412.
[34] S. J. Poon *et al.*, "Half-Heusler phases and nanocomposites as emerging high-ZT thermoelectric materials," *Journal of Materials Research*, vol. 26, no. 22, pp. 2795-2802, 2011/11/004 2011.
[35] Y. I. Y.Shinohara, Y.Isoda, I.A.Nishida, H.T.Kaibe, I.Shiota, "Proceedings of thw 16th Int. Conference on Thermoelectrics, Dresden, Germany," ed, 1997, p. 386.
[36] D. Zhao, C. Tian, Y. Liu, C. Zhan, and L. Chen, "High temperature sublimation behavior of antimony in CoSb3 thermoelectric material during thermal duration test," *Journal of Alloys and Compounds*, vol. 509, no. 6, pp. 3166-3171, 2011.
[37] A. L. Eiss, "Thermoelectric Bonding Study ", ed, 1966.
[38] F. A. Leavitt, J. C. Bass, and N. B. Elsner, "Thermoelectric module with gapless eggcrate," ed: Google Patents, 1999.
[39] N. A, "Thermoelectric Generators for Military Portable Power," ed. SAE Technical Paper, 1967.
[40] W. Luo *et al.*, "Rapid synthesis of high thermoelectric performance higher manganese silicide with in-situ formed nano-phase of MnSi," *Intermetallics*, vol. 19, no. 3, pp. 404-408, 3// 2011.
[41] C. B. Vining, "Thermoelectric properties of silicides," *CRC handbook of Thermoelectrics*, pp. 277-86, 1995.
[42] P. F. Qiu *et al.*, "Thermoelectric properties of Ni-doped CeFe[sub 4]Sb[sub 12] skutterudites," *Journal of Applied Physics*, vol. 111, no. 2, pp. 023705-7, 2012.
[43] M. Ioannou, G. Polymeris, E. Hatzikraniotis, A. U. Khan, K. M. Paraskevopoulos, and T. Kyratsi, "Solid-State Synthesis and

Thermoelectric Properties of Sb-Doped Mg2Si Materials," *Journal of Electronic Materials,* vol. 42, no. 7, pp. 1827-1834, 2013// 2013.

[44] X. Chen, L. Shi, J. Zhou, and J. B. Goodenough, "Effects of ball milling on microstructures and thermoelectric properties of higher manganese silicides," *Journal of Alloys and Compounds,* vol. 641, pp. 30-36, 8/25/ 2015.

[45] Y. Nagamoto, K. Tanaka, and T. Koyanagi, "Transport properties of heavily doped n-type CoSb₃," in *Thermoelectrics, 1998. Proceedings ICT 98. XVII International Conference on*, 1998, pp. 302-305.

[46] S. K. Bux, M. T. Yeung, E. S. Toberer, G. J. Snyder, R. B. Kaner, and J.-P. Fleurial, "Mechanochemical synthesis and thermoelectric properties of high quality magnesium silicide," *Journal of Materials Chemistry,* vol. 21, no. 33, pp. 12259-12266, 2011.

[47] D. B. Migas, V. L. Shaposhnikov, A. B. Filonov, V. E. Borisenko, and N. N. Dorozhkin, "\textit{Ab initio} study of the band structures of different phases of higher manganese silicides," *Physical Review B,* vol. 77, no. 7, p. 075205, 02/25/ 2008.

[48] Y. Miyazaki, D. Igarashi, K. Hayashi, T. Kajitani, and K. Yubuta, "Modulated crystal structure of chimney-ladder higher manganese silicides" *Physical Review B,* vol. 78, no. 21, p. 214104, 12/10/ 2008.

[49] K. Yamazaki, S. H. Risbud, H. Aoyama, and K. Shoda, "PAS (plasma activated sintering): transient sintering process control for rapid consolidation of powders," *Journal of materials processing technology,* vol. 56, no. 1, pp. 955-965, 1996.

[50] K. R. Tarantik *et al.*, "Formation of Ni Electrodes on Sintered N-type Mg_2Si Using Monobloc Sintering and Electroless Plating MethodsThermoelectric Modules Based on Silicides – Development and Characterization," *Materials Today: Proceedings,* vol. 2, no. 2, pp. 588-595, // 2015.

[51] Jaegle.M., "Simulating Thermoelectric Effects with Finite Element Analysis using COMSOL," ed. The 5th European Conference on Thermoelectrics Proceedings, 2007.

[52] M. I. Fedorov, V. K. Zaitsev, and M. V. Vedernikov, "Some peculiarities of development of efficient thermoelectrics based on silicon compounds," in *Thermoelectrics, 2006. ICT '06. 25th International Conference on*, 2006, pp. 111-114.

[53] S. Grasso, Y. Sakka, G. Maizza, and C. Hu, "Pressure Effect on the Homogeneity of Spark Plasma-Sintered Tungsten Carbide Powder," *Journal of the American Ceramic Society,* vol. 92, no. 10, pp. 2418-2421, 2009.

[54] T. C. Holgate, R. Bennett, T. Hammel, T. Caillat, S. Keyser, and B. Sievers, "Increasing the Efficiency of the Multi-mission Radioisotope Thermoelectric Generator," *Journal of Electronic Materials*, vol. 44, no. 6, pp. 1814-1821, 2015// 2015.
[55] J. M. Higgins, A. L. Schmitt, I. A. Guzei, and S. Jin, "Higher Manganese Silicide Nanowires of Nowotny Chimney Ladder Phase," *Journal of the American Chemical Society*, vol. 130, no. 47, pp. 16086-16094, 2008/11/26 2008.
[56] N. P. Institute, *Nickel Plating Handbook*. 2014, p. 80.
[57] I. Aoyama *et al.*, "Doping Effects on Thermoelectric Properties of Higher Manganese Silicides (HMSs, MnSi1.74) and Characterization of Thermoelectric Generating Module using p-Type (Al, Ge and Mo)-doped HMSs and n-Type Mg2Si0.4Sn0.6 Legs," *Jpn J Appl Phys*, vol. 44, no. 6, pp. 4275-4281, 2005/06/15 2005.
[58] Z.-H. Xie, F. Chen, S.-R. Xiang, J.-L. Zhou, Z.-W. Song, and G. Yu, "Studies of Several Pickling and Activation Processes for Electroless Ni-P Plating on AZ31 Magnesium Alloy," *Journal of The Electrochemical Society*, vol. 162, no. 3, pp. D115-D123, 2015.
[59] L. Liming, *Welding and Joining of Magnesium Alloys* (Woodhead Publishing Series in Welding and Other Joining Technologies Series). Woodhead Pub Limited, 2010.

10. APPENDIX

A.1. Table of contact resistances for varying brazing times with Toyota silicide materials.

				Contact 1							Contact 2						Sample Average Resistivity	Average Resistivity (Ohm.cm)
Material	Time (s)	Sample	Run	R1 (mOhm)	R2 (Ohms)	dR (Ohms)	D1 (mm)	D2 (mm)	dD (mm)	Resistivity (Ohm.mm)	Resistivity (Ohm.cm)	R2 (Ohms)	dR (Ohms)	D1 (mm)	D2 (mm)	dD (mm)	Resistivity (Ohm.mm)	Resistivity (Ohm.cm)		
MgSi	10	1	1	0.0042208	0.0041156	0.00010523	3.250	3.375	0.125	0.00480488	4.84E-04	0.0040074	9.6459E-05	3.925	4.075	0.150	0.00369759	3.70E-04	4.27E-04	4.47E-04
		1	2	0.0041796	0.0040642	0.00011545	3.275	3.425	0.150	0.00442562	4.43E-04	0.0039516	0.00010961	3.950	4.125	0.175	0.00360134	3.60E-04	4.01E-04	
		1	3	0.0040015	0.0039314	7.0151E-05	3.275	3.375	0.100	0.00403683	4.03E-04	0.0038057	0.00010815	3.850	3.950	0.100	0.00621856	6.22E-04	5.13E-04	
		2	1	0.0071948	0.007113	8.186E-05	3.250	3.375	0.125	0.00376556	3.77E-04	0.006081	0.00100277	3.800	3.850	0.050	0.11531901	1.15E-02	5.95E-03	5.95E-03
	12.5	3	1	0.0089394	0.0086989	0.00024049	7.880	8.200	0.320	0.00432137	4.32E-04	0.0083411	0.00029915	8.680	9.160	0.480	0.00358358	3.58E-04	3.95E-04	4.17E-04
			2	0.0060164	0.0058522	0.00016419	3.290	3.470	0.180	0.00524499	5.24E-04	0.0057408	0.00010555	3.920	4.100	0.180	0.00337173	3.37E-04	4.31E-04	
			3	0.0059521	0.0058466	0.00010556	3.350	3.530	0.180	0.00337193	3.37E-04	0.0057293	0.00012315	3.920	4.130	0.210	0.00337191	3.37E-04	3.37E-04	
			4	0.0060515	0.0059342	0.00011728	3.250	3.400	0.150	0.00449561	4.50E-04	0.0058639	0.00007623	3.900	4.000	0.100	0.00438225	4.38E-04	4.44E-04	
			5	0.0094963	0.009357	0.00019063	7.945	8.225	0.280	0.00391470	3.91E-04	0.0091121	0.00017303	8.680	8.855	0.175	0.00568537	5.69E-04	4.80E-04	
HMS	10	1	1	0.0167853	0.0162778	0.00050749	8.100	8.275	0.175	0.01667463	1.67E-03	0.0158671	0.00043122	8.800	8.875	0.075	0.03306012	3.31E-03	2.49E-03	3.30E-03
			2	0.017177	0.0165289	0.00064813	7.850	7.975	0.125	0.02981416	2.98E-03	0.0155787	0.00067453	8.850	8.975	0.125	0.03102828	3.10E-03	3.04E-03	
			3	0.0171321	0.0168153	0.00031677	8.100	8.175	0.075	0.02428585	2.43E-03	0.0160909	0.00054848	8.800	8.850	0.050	0.06307577	6.31E-03	4.37E-03	
	12.5	1	1	0.0389186	0.0386601	0.00025844	8.000	8.050	0.050	0.02972048	2.97E-03	0.0380551	0.00030249	8.650	8.750	0.100	0.01739323	1.74E-03	2.36E-03	2.13E-03
			2	0.0348589	0.0343548	0.00050418	7.950	8.075	0.125	0.02319214	2.32E-03	0.0337769	0.00039509	8.475	8.700	0.225	0.01009664	1.01E-03	1.66E-03	
			3	0.0375723	0.0369432	0.00062914	7.925	8.050	0.125	0.02894067	2.89E-03	0.0364052	0.00040277	8.600	8.725	0.125	0.01852742	1.85E-03	2.37E-03	

A.2. Table of samples and corresponding labels for specific testing.

Sample no	Material	Diameter	Notes	Proposed testing	Teer Reference	Columr
9115	HMS	30	Thick/tall puck	f	18929	FEG
9005	HMS	30	Thick/tall puck			
9098	HMS	30	Thick/tall puck			
9099	HMS	30	Thick/tall puck			
9114	HMS	30	Thick/tall puck			
8964	HMS	30	Thick/tall puck			
8889	HMS	40	Defect surface/inclusions			
8848	HMS	40	Snapped in half			
8871	HMS	40	Defect surface/inclusions			
8178	HMS	30				
9278	MgSiSnSb	30	Chipped edge	a	18929	
9320	MgSiSnSb	30		b	18922	
9425	MgSiSnSb	30		c	18924	
9401	MgSiSnSb	30		d	18929	FEG
9418	MgSiSnSb	30		e	18929	

A.3. Contact resistance data for samples with varying metallisation layers and braze

Batch/Process	Brazing Temp (oC)	Barrier layer	Contact (Ω.cm2)	Pellet (Ω.m)
Silverflow-56. 10 minutes. Argon flow 0.25 Bar.	650	Aqueous coolant TiNiAu	9.96E-04	1.43E-05
	630	Aqueous coolant TiNiAu	1.02E-03	1.40E-05
	650	TiNi	3.22E-04	2.09E-04
	630	TiNi	4.67E-04	1.05E-05
	650	Aqueous coolant TiNi	2.05E-03	1.53E-05
	630	Aqueous coolant TiNi	8.35E-04	7.69E-06
	650	TiNiAu	9.32E-04	1.36E-05
	630	TiNiAu	1.22E-03	1.31E-05
	650	NiCr	2.78E-03	1.34E-05
	630	NiCr	2.21E-03	5.46E-06
	650	Toyota MgSi other metallisation	8.58E-06	2.84E-06
	630	Toyota MgSi other metallisation	5.13E-06	2.81E-06
	650	HMS TINiAu	2.53E-05	1.47E-05
	630	HMS TINiAu	1.70E-05	1.63E-05
	650	Toyota HMS other metallisation	1.33E-05	1.71E-05
	630	Toyota HMS other metallisation	3.27E-05	1.74E-05
Silverflow-56. 10 minutes. Argon flow 0.25 Bar.	630	Ti/TiN	1.20E+01	7.12E-03
	630	Ti/TiN/Ti/Ni	4.65E+01	2.47E-02
Silverflo-56. 10 minutes. Argon flow 0.75 Bar.	630	Ti/NiCr	3.91E-03	7.59E-05
	630	Ti/TiN/Ti/Ni	9.99E-04	1.11E-05
	630	Ti/Ni	6.71E-04	1.42E-05
Aluflo HT. 10 minutes. Argon flow 0.75 Bar.	585	Ti/Ni	7.67E-05	1.00E-05

A.4. Bond line measurements and approximated compositions from SEM and XPS analysis of a HMS sample corresponding to figure 41.

Line Number	R [µm]	Average Thickness [µm]	Standard Deviation [µm]	Layer Composition
1	37.5	23.4	11.9	Silverflow-56
2	32.2			
3	8.7			
4	15.0			
5	22.4	22.6	2.56	Nickel 50% Silicon – Copper equal
6	25.5			
7	24.0			
8	18.6			
9	8.8	18.3	8.0	Copper + Nickel + trace Ag, Mn and Si
10	14.3			
11	19.5			
12	30.5			
13	32.7	37.3	3.2	HMS with interstitial Ni and Ag
14	36.4			
15	41.6			
16	38.3			
17	102.8	103.0	1.0	Whole junction
18	104.6			
19	102.8			
20	101.9			